N° d'ordre : 40939

THESE

Présentée à l'Université de Lille 1 - Sciences et Technologies
ECOLE DOCTORALE SCIENCES POUR L'INGENIEUR

Pour l'obtention du grade de

DOCTEUR DE L'UNIVERSITE LILLE 1

Spécialité : MICRO ET NANOTECHNOLOGIE, ACOUSTIQUE ET TELECOMMUNICATION

Par
Salim EL KAZZI

« Croissance épitaxiale d'hétérostructures antimoniées sur substrats fortement désadaptés en maille pour applications aux transistors à effet de champ»

Soutenance présentée le 13 Novembre 2012

Membres du Jury :

Rapporteurs :	**Saint-Girons Guillaume**	Chargé de Recherche à l'INL
	Tournié Eric	Professeur à l'Université de Montpellier 2
Examinateurs :	**Baron Thierry**	Directeur de Recherche au LTM
	Ruterana Pierre	Directeur de Recherche au CIMAP
	Bollaert Sylvain	Professeur à l'Université de Lille1
	Lefebvre Isabelle	Chargée de Recherche à l'IEMN
Co-encadrant :	**Desplanque Ludovic**	Maître de Conférences à l'Université de Lille1
Directeur de thèse :	**Wallart Xavier**	Directeur de Recherche à l'IEMN

A mon père, ma mère et à la mémoire de ma tante Henriette.

« Vous êtes bon lorsque vous marchez fermement vers votre but d'un pas intrépide. Pourtant, vous n'êtes pas mauvais lorsque vous y allez en boitant. Même ceux qui boitent ne vont pas en arrière. »
Khalil Gibran, « Le Prophète » - Le Bien et Le Mal

Remerciements

Avant tout et à chaque instant, je remercie Dieu et Sainte Marie pour leur protection et amour.

Ces travaux se sont poursuivis au sein de l'Institut d'Electronique, de Microélectronique et de Nanotechnologie (IEMN) dans le cadre du projet ANR MOS 35. Je remercie Messieurs Alain Cappy et Lionel Buchaillot, directeurs successifs de l'IEMN, de m'avoir accueilli et permis d'y mener à bien ma thèse.

Je tiens ensuite à remercier particulièrement Madame Isabelle Lefebvre et Messieurs Eric Tournié, Guillaume Saint-Girons, Pierre Ruterana, Thierry Baron et Sylvain Bollaert d'avoir accepté de participer à mon jury de thèse.

Mes remerciements les plus profonds sont, bien entendu, pour mon directeur de thèse Xavier Wallart et mon encadrant Ludovic Desplanque. Je vous remercie Xavier de m'avoir accueilli dans votre équipe et de m'avoir encadré pendant ces trois années passées. Vos questions, remarques et réponses m'ont permis d'aller plus loin dans mon travail. A chaque contact, votre professionnalisme et votre vision au-delà de l'épitaxie m'ont vraiment permis de progresser. Ludovic je te remercie d'abord parce que tu m'as évité de me fourvoyer en me faisant « revenir sur terre ». Je te remercie de m'avoir formé et accompagné tout au long de cette expérience professionnelle avec beaucoup de bonne humeur, de pédagogie, de précision et surtout avec beaucoup de patience. Ce travail n'aurait pas pu être complet sans tes nouvelles idées, ton aide et surtout ta logique. Comme parfois les mots ne peuvent pas tout dire, Xavier et Ludovic, c'était un honneur de travailler avec vous et j'espère avoir la chance de retravailler avec vous très prochainement.

Je souhaite également remercier Messieurs Pierre Ruterana et Yi Wang de l'Université de Caen qui ont effectué les analyses de microscopie électronique en transmission et qui répondaient toujours très rapidement à nos questions et demandes.

J'adresse également mes remerciements à Jean-Louis Codron et Christophe Coinon. Jean-Louis, je voyais toujours en toi l'image d'un vrai père. Merci pour ton support, ta formation sur le bâti solide et ta gentillesse qui a même touché ma famille. De même Christophe, merci pour le temps que tu m'as accordé pour me former sur le bâti gaz et l'effet Hall. Je n'oublierai jamais nos discussions agréables et surtout ton « ha ha ha ».

Je tiens à remercier Eléonore Moreau, ma collègue de bureau, qui m'a quitté au début de la troisième année. Yeyo merci de m'avoir aidé dès que je suis arrivé à Lille. Lorsque tu es partie, je me suis senti un peu perdu, seul dans le bureau.

Bien sûr, je ne peux pas oublier Dominique Deresmes qui m'a tout appris sur l'AFM. Merci Dominique parce que, même quand ce n'était pas ton problème, tu étais prêt à m'aider pour le résoudre.

Sébastien, Javier et Sylvie, même si vous êtes partis tôt, merci à tous pour vos encouragements.

Je ne peux être que reconnaissant à Philippe Caroff pour nos discussions enrichissantes. Depuis le début, j'étais étonné de ta grande passion pour faire avancer les choses. Merci Philippe, tu me motivais énormément lorsqu'on papotait ensemble. Bonne chance à toi et à ta famille et à très bientôt j'espère.

Merci à Dominique Vignaud pour ces réponses et parce qu'à chaque question, il me proposait gentiment de m'asseoir.

Un grand merci à tout le groupe « Photonique THz », particulièrement Emilien pour son humour mais aussi Jean François, Guillaume, Tahsin et Mathias.

Merci pour les anciens thésards, surtout Estelle Mairiaux et Aurélien Olivier pour leurs conseils. Estelle, tu avais raison, on rigole moins à la fin. Aurélien, attends moi, j'arrive.

J'adresse également mes remerciements à ma « nouvelle amie » Arame Thiam qui m'a toujours poussé à continuer. Merci pour ta générosité Arame, ta gentillesse, ton grand cœur et surtout ton sourire éclatant.

Alex, le Maestro, l'ami que je n'oublierai jamais pour son humour, je veux seulement te dire « Mec tu es très fort ». Ensuite, je remercie l'ensemble des thésards et postdocs de l'IEMN qui étaient là pendant ces 3 ans : Fabio Pavanello « my friend » et Philipp Latzel le grand basketeur, Yoan my man, Abbas et Abdallah mes compatriotes, Cyrille le grand et les belles Sonia et Marina.

Pour finir, je tiens à remercier ma famille et mes proches amis pour leur soutien tout au long de ce travail. Je vous aime tous.

A tous, un grand MERCI.

Epitaxial growth of Sb-based heterostructures on highly mismatched substrates for field effect transistor applications

Low power consumption transistors operating at low supply voltage are highly required for both high frequency autonomous communicating systems and CMOS technology. Since the performances of silicon-based devices are strongly degraded upon low voltage operation, low bandgap III-V semiconductors are now considered as alternative active materials. Among them, one of the best candidates is InAs. Therefore, the present work aims on paving the way to the use of InAs in transistor channels for both high-speed analog and digital applications. We particularly investigate the molecular beam epitaxy growth of InAs/AlSb heterostructures on both (001) GaAs and GaP via an antimonide metamorphic buffer layer. Using atomic force microscopy, transmission electron microscopy and reflection high energy electron diffraction, we first show the critical influence of the growth conditions on the III-Sb nucleation. From this study, we then achieve optimized high mobility InAs layers on these two highly mismatched substrates. The results obtained in the GaP case are extended to commercially available high quality GaP/Si platforms for the integration of InAs-based materials on an exactly oriented (001) Si substrate. State of the art mobility of 28 000 $cm^{-2}.V^{-1}.s^{-1}$ at 300K and higher than 100 000 $cm^{-2}.V^{-1}.s^{-1}$ at 77K are demonstrated.

Croissance épitaxiale d'hétérostructures antimoniées sur substrats fortement désadaptés en maille pour applications aux transistors à effet de champ

La nécessité de diminuer la consommation à la fois des systèmes autonomes communicants à haute fréquence et des circuits CMOS implique l'utilisation de transistors fonctionnant sous faible tension d'alimentation. Les performances des composants à base de silicium se dégradant rapidement dans ce régime de fonctionnement, les semiconducteurs III-V à faible bande interdite sont aujourd'hui envisagés comme une alternative. Parmi ceux-ci, l'InAs paraît le plus prometteur. Dans ce contexte, ce travail a pour but d'ouvrir la voie à l'utilisation d'un canal à base d'InAs pour les systèmes analogiques et numériques. Plus précisément, nous étudions la croissance par épitaxie par jets moléculaires des hétérostructures InAs/AlSb sur des substrats (001) GaAs et GaP par l'intermédiaire d'une couche tampon Ga(Al)Sb. La microscopie à force atomique, la microscopie électronique en transmission et la diffraction d'électrons de haute énergie sont utilisées afin de mettre en évidence l'influence critique des conditions de croissance sur la nucléation des antimoniures. Cette étude sert de base à l'optimisation de canaux InAs à haute mobilité sur ces deux substrats fortement désadaptés en maille. Les résultats obtenus dans le cas de GaP sont ensuite étendus au cas de pseudo-substrats commerciaux GaP/Si de haute qualité cristalline pour l'intégration de matériaux à base d'InAs sur des substrats Si (001) exactement orientés. Des mobilités électroniques atteignant 28 000 $cm^{-2}.V^{-1}.s^{-1}$ à 300K et supérieures à 100 000 $cm^{-2}.V^{-1}.s^{-1}$ à 77K sont démontrées.

TABLE OF CONTENTS

Introduction *11*

I. Background *15*

I.1: III-Sb semiconductors *15*
I.1.A: Crystal and optoelectronic properties *15*
I.1.B: Electronic and optoelectronic devices *18*
I.1.B.1: Some optoelectronic devices *18*
I.1.B.2: electronic applications and AlSb/InAs HEMTs *19*

I.2: Heteroepitaxy of 6.1 Å family on standard substrates *22*
I.2.A. Generalities on the growth of highly mismatched III-V materials *22*
I.2.A.1: Nucleation mechanism and growth modes *22*
I.2.A.2: Misfit dislocations in CFC *26*
I.2.A.3: Threading dislocations and stacking faults *27*
I.2.B. Growth of (Al)GaSb on GaAs *29*
I.2.B.1: Gradual metamorphic growth *29*
I.2.B.2: Misfit disclocation array growth mode *30*
I.2.B.2.1: InAs on GaAs(P) *31*
I.2.B.2.2 GaSb on GaAs *33*
I.2.C: Growth of (Al)GaSb on Si *35*
I.2.C.1: Antiphase Domains *35*
I.2.C.2: III-V direct growth on (001) Si *37*

I.3. Conclusion and thesis objectives *41*

II. Experimental setup *49*

II.1: Material Growth *49*
II.1.A: IEMN MBE chambers *49*
II.1.B: Elemental sources *50*
II.1.B.1: Group III element sources *50*
II.1.B.2: Group V element sources *52*
II.1.C: Temperature measurement and calibration of the substrate *53*
II.1.D: Reflection high-energy electron diffraction (RHEED) *54*
II.1.D.1: Surface characterization and lattice constant *54*
II.1.D.2: Flux calibration *57*

II.2: Material characterization *58*
II.2.A: Atomic Force Microscopy (AFM) *58*
II.2.B: Transmission Electron Microscopy (TEM) *59*
II.2.C: Hall effect measurements *61*

III. Nucleation and strain relaxation of GaSb on highly mismatched substrates *67*
III.1: Surface reconstructions *67*
III.1.A: GaAs surface *67*
III.1.A.1: (001) GaAs considered reconstructions *67*
III.1.A.2: Influence of GaAs reconstruction on GaSb growth *71*
III.1.B: GaP surface *78*
III.1.B.1: Observed reconstructions *78*
III.1.B.2: Influence of the surface reconstruction *80*

III.1.C. Conclusion *82*

III.2: Influence of the experimental parameters on the early stages of GaSb growth*83*
III.2.A: Influence of the growth temperature *83*
III.2.B: Influence of the growth rate *89*
III.2.C: Influence of the Sb flux *92*
III.2.D: Discussion *94*
III.2.E: Conclusion *96*

III.3: Towards island coalescence *97*

III.4: Conclusion *100*

IV. Growth of high electron mobility AlSb/InAs hétérostructures *105*

IV.1: Generalities *105*
IV.1.A: AlSb/InAs HEMTs *105*
IV.1.B: Electron mobility in heterostructure systems *106*
IV.1.C: Anisotropic transport properties in AlSb/InAs *108*

IV.2: Growth of AlSb/InAs heterostructures on highly mismatched III-V substrates *110*
IV.2.A: AlSb/InAs heterostructure design *110*
IV.2.B: Samples *112*
IV.2.C: Influence of the Sb flux on the electron mobility of AlSb/InAs heterostructures grown on mismatched substrates *114*
IV.2.C.1: Study on GaAs substrates *114*
IV.2.C.2: Study on GaP substrates *117*
IV.2.D: Influence of the growth temperature on the electron mobility of AlSb/InAs heterostructures grown on mismatched substrates *119*
IV.2.E: Summary *123*

IV.3: Integration of AlSb/InAs heterostructure on direct (001) Si substrate via GaSb/GaP accomodation layer *123*

IV.4: Conclusion *127*

Conclusions and perspectives *131*
List of communications *135*

INTRODUCTION

The future needs of society in electronic equipment cover the field of ambient intelligence, in particular objects or communicating sensors. Most of these objects should be integrated in their environments but also energy independent. This means that these systems must be self-reinforcing extracting available energy around them or from electromagnetic waves, mechanical and even thermoelectric energies. Aarts et al. [1] introduced the consequences of the ambient intelligence vision for electronic devices by mapping the involved technologies on a power-information graph (figure 1). He showed that the autonomy is only possible for consumption with a very low power.

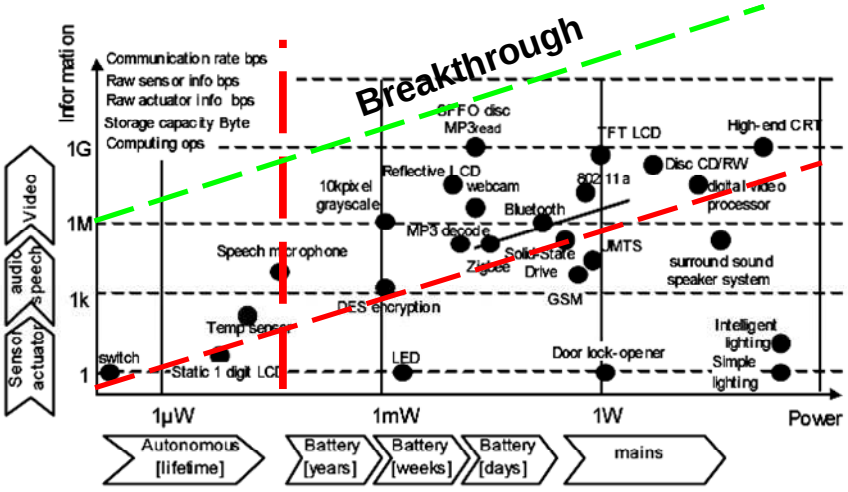

Figure from ref. [1] *showing technologies mapped on a power-information graph*

By looking at the bit rate performance at less than 100 µW, we can notice that we are still limited at 1 Kbit/s by using a Si CMOS (complementary metal-oxide-semiconductor) technology. Hence the fabrication of low power consumption transistors which constitute circuits is still highly required. The key point to achieve a low power consumption transistor (besides its topology change) is the reduction of its supply voltage V_{dd} for 50 to 200mV, which is to say a few kT/q at room temperature. However, this reduction is not possible for Si CMOS transistors [2] (V_{dd} ~ 0.5-1 V) since the mobility in silicon is too low to compensate the degradation of the cut-off frequency at low V_{dd}. Therefore, researchers are interested to use other semiconductor materials which have low bandgap energy and high electron mobility [3,4]. In this vein, the ANR MOS 35 project [5] proposes to produce high frequency transistors working at very low V_{dd} and based on III-V materials.

On the other hand, the well-established CMOS technology which has allowed the development of most electronic devices since more than 30 years is now facing a power consumption crisis. Indeed, the power consumption of modern electronic chips has reached 100W/cm^2 which can be considered as an upper limit. Since year 2004, this has stopped for instance the increase in clock frequency in processors. Once again, there is a need for supply voltage reduction, using low bandgap energy and high electron mobility materials [6].

Among the III-V semiconductors, as far as electron transport is concerned, one of the best candidates for low voltage operations is InAs, which exhibits a low electron effective mass of 0.026 m_0, a 300K mobility above 30 000 cm^2/V.s. and a saturation velocity above 4x10^7 m/s. Most of the recent studies in the field have focused on the InGaAs alloy which has a bit less interesting transport properties but can be easily grown epitaxially on InP substrates. The present work aims going further and paving the way to the use of InAs as active channel material. Since the III-V modulation-doped heterostructures provide excellent models to study the transport property of the channel, one can learn more about the problems of future III–V transistors with these kinds of structures [7]. Hence, we decide to focus in this work on the InAs/AlSb system which is the most commonly used heterostructure to achieve high electron mobility at room temperature.

However, due to the large lattice mismatch between InAs and commonly available substrates (about 12% with GaP and Si, about 8% with GaAs), the fabrication of InAs-based devices requires the development of an integration pathway on highly mismatched substrates. Motivated by this challenge, the researchers have been using two techniques. The first one makes use of “Wafer-bonding” which consists on bringing into contact two perfectly flat and clean materials to connect them mechanically thanks to the Van Der Walls forces. However, this technique is still limited by its high cost, its complexity and the fact that it does not allow a 300 mm full wafer processing [8]. The second method, called “monolithic integration”, is the one used in this work and consists on the epitaxial growth of III-V semiconductors directly on the foreign substrate. Regarding integration on Si substrates, the most often popular scheme is to use GaAs/Ge/Si intermediate layer for which the antiphase domain (APD) problem is treated at the nearly lattice matched Ge/GaAs interface. In the case of InAs-based epitaxy, this approach would imply 2 steps in the mismatch accommodation, the first one between Si and Ge and the second one between GaAs and InAs, leading to rather thick buffer layers.

In this work, we will investigate the molecular beam epitaxy (MBE) growth of InAs-based heterostructures on both (001) GaAs and GaP substrates. The former case can be useful either for low power high frequency applications on semi-insulating GaAs substrates or to the integration of InAs MOSFETs on Si via the above mentioned Si/Ge template. In the latter case, the idea is to demonstrate a two-step solution addressing first the problem of APDs during the epitaxial growth of a GaP interfacial layer on a (001) exactly oriented silicon substrate. The mismatch is then accommodated through a GaSb buffer layer grown on the GaP/Si template. Since high quality GaP/Si templates grown by MOVPE have been achieved in Marburg University [9], we will focus first on the optimization of the MBE growth of AlSb/InAs heterostructure on (001) GaP. Then, we will transfer the growth conditions for the integration on Si, using the Marburg University GaP/Si template.

This manuscript is divided in four chapters. The first provides an introduction to antimonide materials and devices, it outlines the basic knowledge on the InAs/AlSb system and the problems related to the growth of highly mismatch materials. The main targets of this PhD thesis are exposed. The second chapter describes the experimental techniques which are used in this work and their main characteristics. The third chapter details the investigations concerning the nucleation of GaSb on mismatched substrates. The fourth chapter then presents the optimization of the antimonide buffer layer for the growth of high electron mobility AlSb/InAs heterostructure on GaAs and GaP. It mainly reveals the importance of the nucleation process of the buffer layer on the active layer transport property. At the end of this chapter, the growth of AlSb/InAs heterostructures on Si is reported, using GaP/Si platforms.
Finally, we discuss in the conclusion the relevance and possible future research in the technical areas studied in this work.

References

[1] Emile Aarts and Raf Roovers, Proceedings of the Design,Automation and Test in Europe Conference and Exhibition (2003) 1530

[2] ITRS 2006 Update *http://www.itrs.net/Links/2006Update/2006UpdateFinal.htm*

[3]ftp://ftp.cordis.europa.eu/pub/fp7/ict/docs/events3-20070226-07-mfgineurope-duallogic-dimoulas-230207_en.pdf

[4] R. Chau, S. Datta, M. Doczy, B. Doyle, B. Jin, J. Kavalieros, A. Majumdar, M. Metz, and M. Radosavljevic, Nanotech, IEEE transactions **4** (2005) 153

[5] MOS35 ANR Project, Contract No. ANR-08-NANO-022

[6] Jesús A. del Alamo, Nature **479** (2011) 317

[7] J. del Alamo, J. A., Kim, D.-H., Kim, T.-W., Jin, D. & Antoniadis, D. A. Int. Conf. Indium Phosphide Relat. Mater. (IEEE, 2011)

[8] H. Ko, T. Takei, R. Kapadia, S. Chuang, H. Fang, P. W. Leu, K. Ganapathi, E. Plis, H. S. Kim, S.-Y. Chen, M. Madsen, A. C. Ford, Y.-L Chueh, S. Krishna, S. Salahuddin and A. Javey, Nature **468** (2010) 286

[9] A. Beyer, J. Ohlmann, S. Liebich, H. Heim, G. Witte, W. Stolz, and K. Volz, J. Appl. Phys. **111** (2012) 083534

CHAPTER I: Background

This chapter aims at introducing the objectives of this work within the context of antimony based materials for electronics and optoelectronics. The first part is devoted to III-Sb crystal and electronic properties. Then, we review the major applications that have been developed using antimonides. In the second part, we present the problems encountered during the growth of highly mismatched materials on standard commercially available III-V substrates and their influence on device performances. We also show some of the attempts that have been made to facilitate the integration of III-Sb directly onto Si substrates. Finally, the third part explains the main objectives of this thesis by presenting the way of investigation considered within this work.

I.1. III-Sb semiconductors

I.1.A. Crystal and optoelectronic properties

III-V semiconductors are compounds formed by a group-III element (Ga, Al, In…) and another group-V element (P, As, Sb, N) from the Mendeleev's periodic table. Beside the nitrides, these compounds have a crystallographic zinc blende structure composed of two face-centered cubic (fcc) sub-lattices (Fig. I.1). One of these sub-lattices is occupied by group-III elements, whereas the other is occupied by group-V elements [1].

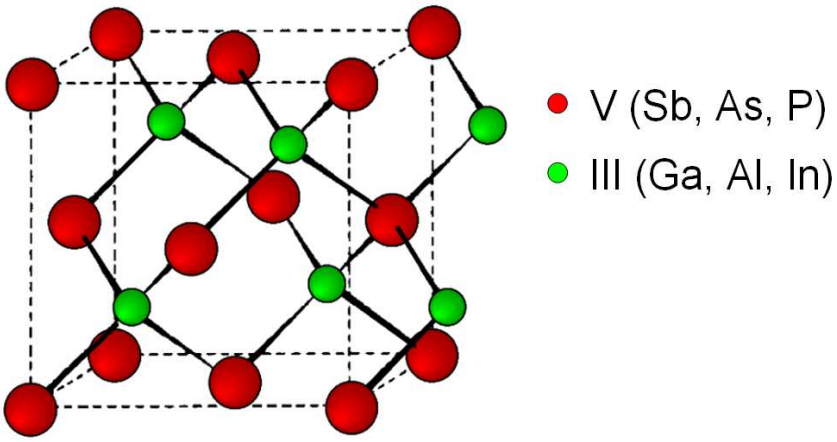

***Figure I.1**: Unit cell structure of a zinc blende lattice. III atoms are shown in green (small), V atoms shown in red (large), and the dashed lines show the cubic cell [2].*

The number of possible combinations between the III and V elements leads to the realisation of a wide variety of semiconductors which have the same crystal structure. The lattice constant depends on the alloy composition and is determined by the Vegard law [3]. For example, if we consider the semiconductor compound $Al_xGa_{1-x}Sb_yAs_{1-y}$, its lattice constant $a_{AlGaAsSb}$ is equal to:

$$a_{AlGaAsSb} = xya_{AlSb} + x(1-y)a_{AlAs} + (1-x)ya_{GaSb} + (1-x)(1-y)a_{GaAs} \qquad \textbf{(Eq. I.1)}$$

where a_{AlSb}, a_{AlAs}, a_{GaSb} and a_{GaAs} are the lattice constants of binary compounds found in figure I.2. One can also extend the Vegard law to determine semiconductor band gap energies and the corresponding wavelength λ. Considering $Al_xGa_{1-x}Sb_yAs_{1-y}$, we can find an expression that relates the band gap energies, Eg, to the ratio of the constituents and a bowing parameter b:

$$Eg_{AlGaSbAs} = xyEg_{AlSb} + x(1-y)Eg_{AlAs} + (1-x)yEg_{GaSb} + (1-x)(1-y)Eg_{GaAs} - b(1-x)(1-y)xy \qquad \textbf{(Eq. I.2)}$$

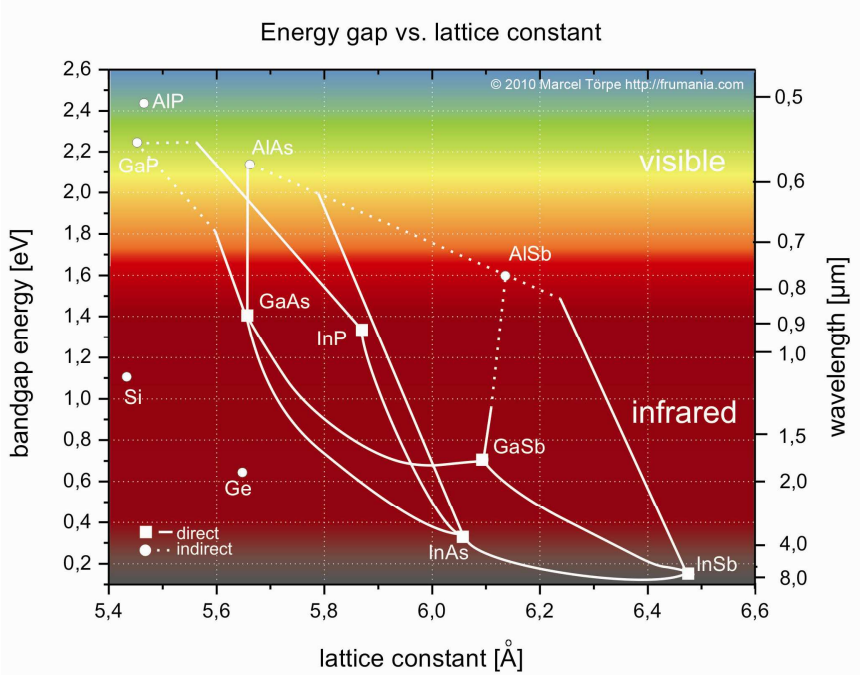

***Figure I.2**: Lattice constant, bandgap energies and wavelengths of various III-V semiconductors [4].*

In figure I.2, we can notice that binary III-Sb compounds, along with InAs are semiconductors emitting in the infrared (IR) domain, i.e. λ > 800 nm. Furthermore, this figure shows that besides AlSb which has an indirect band gap, these materials have very small direct bandgap energies in comparison with other III-V materials. Therefore, direct bandgap III-Sb (along with

InAs) semiconductors are very important for optoelectronic applications in the IR range and many lasers, photodiodes, etc... are fabricated in this domain [5].

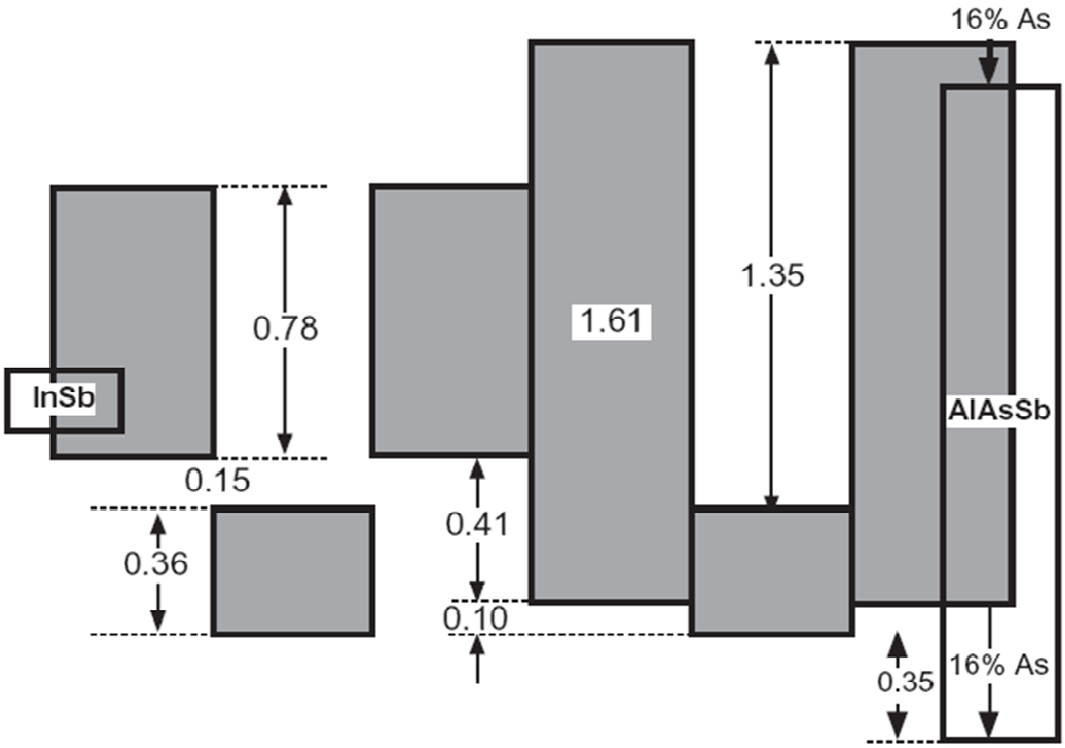

	InSb	GaSb	InAs	GaSb	AlSb	InAs	AlSb
m^*_e/m_0	0.013	0.039	0.024	0.039	0.14	0.024	0.14
m^*_{hh}/m_0	0.24	0.22	0.26	0.22	0.47	0.26	0.47
μ_e (cm²/V.S)	77000	5000	40000	5000	200	40000	200
μ_h (cm²/V.S)	1100	1000	450	1000	420	450	420

Figure I.3*: Band line-ups of III-Sb and InAs semiconductors. The shaded areas represent the energy gaps. All energies are in eV [6].*

On the other hand, these materials present unique electronic properties not encountered in other systems [6]. Compared to GaAs (8 000 cm^2/Vs), we can notice from figure I.3 that besides InSb which has a lattice constant (6.47 Å) greater than all other materials, InAs has the highest electron mobility with a lattice constant close to 6.1 Å (or 6.1 Å family). Moreover, GaSb and InSb exhibit the highest hole mobility among III-Vs. Secondly, this system presents a great variety of band line-ups from type I to type III. For example in figure I.3, the InAs/GaSb type III system is characterized by a broken gap line-up at the interface and the lowest states of InAs conduction band lie below the highest states of GaSb valence band. The difference is about 150

meV. Replacing Ga with Al, the valence band drops, closing the broken gap and leading to a type II line-up. The conduction band rises by about 0.4 eV, leading to a large InAs/AlSb conduction band offset of 1.35 eV. Type I line-up can also be observed for the AlSb/GaSb system. The peculiar configurations that can be achieved associating 6.1 Å materials are of great interest both for fundamental research and innovative device applications.

I.1.B. Electronic and optoelectronic devices

In this part, we discuss the main applications involving the use of antimonide materials. Since one of our goals at IEMN is to achieve a high performing InAs-based HEMT, we present in the second section the major work done on the InAs/AlSb system that is mostly used for these types of HEMTs. With the help of this system we also demonstrate why antimonides are suggested to address millimeter wave applications, such as low noise and ultra low power consumption. Finally, the state of the art on InAs/AlSb heterostructure is presented to reveal the remaining work to do on this system.

I.1.B.1. Some optoelectronic devices

An example of device using III-Sb in optoelectronics is the mid-infrared (MIR) laser. It is known that for the first quantum well laser diodes operating in the 3-5 microns range, type I line-up was used in the active zone [7]. After showing that non-radiative Auger recombinations limit the device performances, researchers decided to use type II and III line-ups in the active region of bipolar MIR lasers. The target was to limit by several orders of magnitude losses by Auger effect [8-10]. Since antimonides easily offer this variety of band line-ups, W type lasers were then fabricated using these materials and high performances were reached. For instance, Jouillé et al. [11] have obtained InAs(PSb)-based "W" quantum well laser diodes emitting near 3.3 μm up to 135 K, and Bewley et al. reached an operating temperature of 195 K with a continuous-wave operation at 3.25 μm [12].

Other types of MIR lasers were precisely fabricated with InAs/AlSb and GaInAs/AlAsSb systems which have been used as a solution to increase the conduction band offset in quantum cascade lasers (QCLs). Lasers emitting at 6.7 and 4.5 μm at 300K [13-14] were reported with InAs/AlSb and more recently, lasing was observed on GaInAs/AlAsSb material system in pulsed mode for a temperature of 400 K with a wavelength emission of 4.5 μm [15]. The good performance of III-Sb QCLs and the variety of the band line-ups in these materials motivated many groups to propose AlSb/InAs/GaInSb/GaSb interband cascade lasers (ICLs). With these

lasers, threshold current of 1.3x 10^5 A/cm^2 and a conversion efficiency of 17% were measured [16]. Many IR photodetectors were also fabricated with these materials due to their ability to cover the largest area of wavelength in the MIR between all the III-V materials. Since the efficiency of photodetectors requires low temperature operation, a new generation of high performance III-Sb IR photodetectors using a Peltier module was developed [17]. More recently, Rodriguez et al. [18] reported on a GaInAsSb/AlGaAsSb QW laser structure grown by MBE on a (001) oriented GaAs substrate. RT, continuous-wave (cw) operation around 2.2 μm is achieved which is the longest wavelength emission for an interband laser grown on GaAs cw operating at RT. In the same year, they demonstrated a RT operation GaSb-based type-I laser at 2.25 μm on a (001) Si substrate but this time in pulsed regime [19]. By further optimizing the growth conditions, it didn't take them so long to successfully achieve a cw operation of GaSb-based LDs emitting near 2 μm and directly grown onto silicon, opening the route to the direct monolithic integration of III-V devices on a Si platform [21].

I.1.B.2. Electronic applications and AlSb/InAs HEMTs

Antimonide electronic applications include both high-speed analog and digital systems used for data processing, communications, imaging and sensing. In figure I.4 given by Bennett et al. [21], we can see the trend toward higher frequencies and lower consumption with increasing lattice constant. The development of Sb-based transistors for use in low-noise high-frequency amplifiers, digital circuits, and mixed-signal circuits could provide the enabling technology needed to address these rapidly expanding needs.

From this figure, the first HEMTs were fabricated with GaAs channels and AlGaAs barriers on GaAs substrates [22]. In order to achieve higher electron mobility and velocity, the consistent progression of this trend was to use pure InAs as the channel (30 000 cm^2/ V.s and velocity of 4.10^7 cm/s) along with nearly lattice-matched AlSb, AlGaSb or InAlSb barriers. InSb-channel HEMTs were also fabricated with InAlSb barriers reaching mobility as high as 40 000 cm^2/V.s at room temperature (RT) [23]. However, the most commonly used heterostructure for antimony based compound semiconductors (ABCS) is AlSb/InAs since these two materials have nearly similar lattice constants along with a large conduction band offset (1.35 eV) [24]. While AlSb/InAs heterostructures growth were first reported in the early 1980s [25], first AlSb/InAs HEMTs was fabricated in 1987 [26].

These devices are particularly appealing for low noise performance [27]. Recently, low noise amplifier (LNA) were developed using AlSb/InAs HEMTs from Chalmers University of Technology (Sweden) showing high frequency and low noise performances combined with low DC power consumption [28]. Even if further improvements in the device and epitaxial structure layouts are required for these type of HEMTs, they claimed that their results have attained microwave noise performance comparable to GaAs(InP)-based HEMTs.

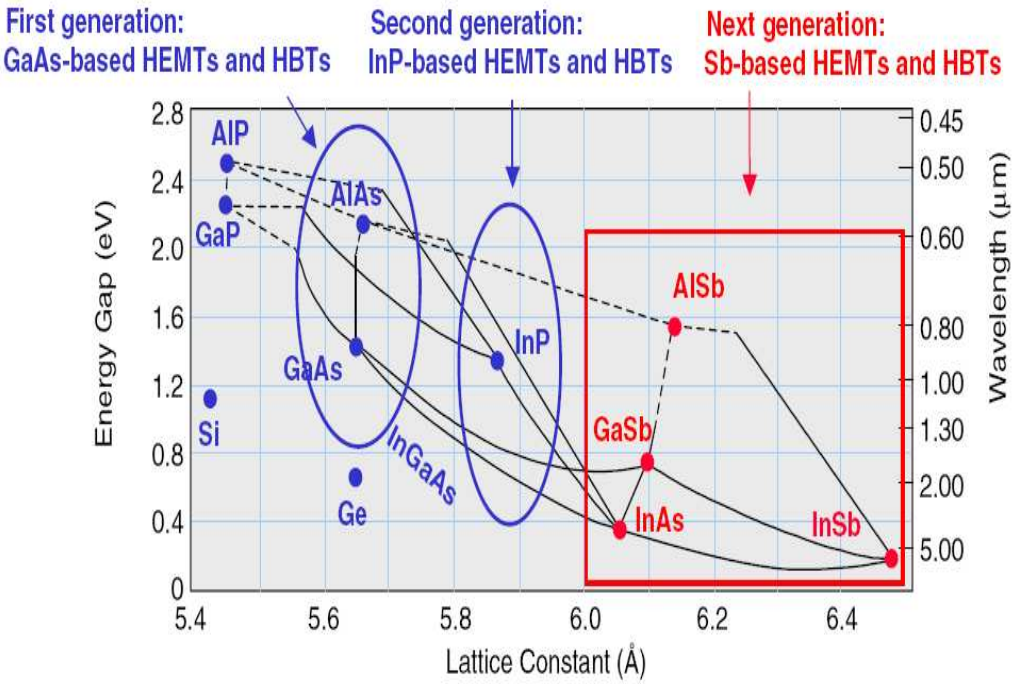

Figure I.4: *Energy gap versus lattice constant, showing the evolution of transistors to larger lattice constants and smaller bandgaps for high-frequency and low-power consumption [21].*

Since high mobilities and low sheet resistance are desired for HEMT applications, many studies were interested to achieve the best AlSb/InAs heterostructure properties. We note that many variations could play a crucial role on the InAs transport properties such as interface control [29,30], channel thickness [31] and doping plane [32]. One challenge to increase the transistor performances is to combine large mobility and large sheet carrier density, which has a straightforward impact on the resistance. Best published results on InAs/AlSb HEMTs are from Rockwell-UCSB [33] with a sheet resistance of 89 Ω/□, n_s = 3.7 10^{12}/cm² and µ = 19 000 cm²/Vs. At 77 K, n_s is 3.4 10^{12}/cm² and µ = 65 000 cm²/Vs (best result ever reported for a III-V heterostructure used in HEMTs). Figure I.5 displays the relationship between mobility and carrier density reported by IEMN and different groups on the InAs/AlSb system. One can see

that mobility is often higher than 20 000cm²/Vs with a sheet carrier density of 1.5-2 x 10^{12}/cm². Best reported mobility at IEMN is μ = 34 000 cm²/Vs with n_s = 1.4 x 10^{12}/cm² on an InP substrate [34]. At 77 K, the mobility can exceed 200 000 cm²/Vs. The two main dopants that are frequently used for this system are Silicon and Tellurium.

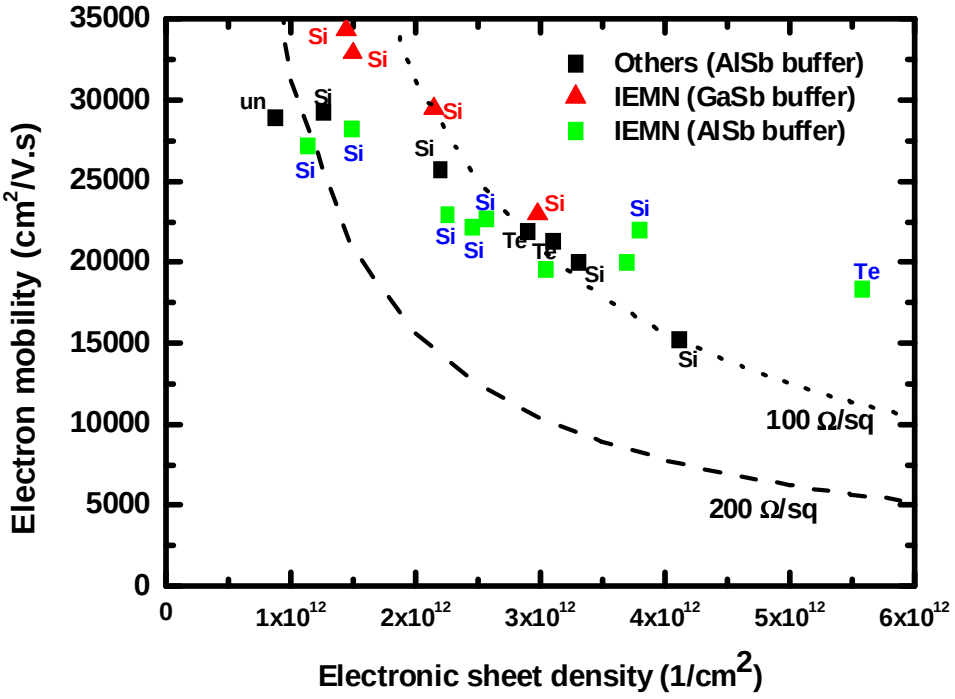

Figure I.5: *Electron mobility versus sheet density for InAs single quantum wells from [21, 33, 34]. The doping technique is indicated close to each point.*

Eventhough AlSb is considered as the ideal buffer for a transistor since GaSb presents low resistivity, inducing leakage current in the buffer, better transport properties result from using GaSb buffers. Kroemer et al. for instance declared that the Ga adatoms tend to be more mobile than A1 adatoms and therefore smooth out the roughness generated in the nucleation layer [35,36]. They found that a GaSb buffer provides mobilities in the InAs QW nearly an order of magnitude greater than with an A1Sb buffer. A record mobility of 944 000 cm^2/Vs at 12 K was hence achieved. It's important to mention that even if we have discussed the work that have been already done on InAs/AlSb HEMTs, much progress has been also achieved on other III-Sb electronic devices like RTDs and HBTs [37,38]. In all cases, the main advantage of Sb-structure is the same in terms of high-frequency operation, low noise and power consumption.

Obviously, all the studies on both electronic and optical devices lead to a considerable progress that has been made in the fabrication of the antimonide-arsenide system in the active

layers. However, the growth of these active layers on ideal substrates for the technology industry remains a big challenge. For optoelectronic devices, many groups have used a lattice matched n-doped (or p-doped) GaSb substrates for high optical performances. Beside their high cost, GaSb substrates also present p-type residual doping preventing them to be used for high frequency electronic devices. The use of other commercially available susbtrates (GaAs, Si) is hence a must and the study of the growth of ABCS on highly mismatched substrates is still very relevant.

I.2. Heteroepitaxy of 6.1 Å family on standard substrates

The studies on the metamorphic growth of III-Sb and InAs on mismatched substrates, involving mainly (Al)GaSb buffer layers, reveal three main growth problems. First, the large lattice mismatch between the active layers and the substrate leads to a high density of threading defects (TDs) that propagate in the active layers and deteriorate device performances. Secondly, the polar/non polar interface involves, like for other III-V materials, the formation of antiphase domains (APDs). Finally, the difference in the thermal coefficients with Si can create cracks in the structure for thick layers during their cooling down from the growth temperature to room temperature.

In this paragraph, we try to tackle the problem of III-Sb buffer layer growth on highly mismatched substrates. We first present the main difficulties encountered during the growth of highly mismatched materials and their influence on device performance. In order to achieve the growth of III-Sb on the ideal substrate for the technology industry (Si), we finish by mentioning some of the solutions that has been previously proposed for the integration of III-Sb directly on silicon.

I.2.A. Generalities on the growth of highly mismatched III-V materials

I.2.A.1. Nucleation mechanism and growth modes

"**Heteroepitaxy**" is the kind of epitaxy where a crystalline film is grown on a crystalline substrate or film of different chemical nature. The lattice mismatch between the epilayer and the substrate is given by:

$$f = \frac{a_{layer} - a_{substrate}}{a_{substrate}} \qquad (\textbf{\textit{Eq. I.3}})$$

where a_{layer} and $a_{substrate}$ are the lattice constants of the epi-layer and the substrate, respectively. Being much thicker, the substrate imposes its lattice constant at the beginning of the growth. Hence, the lattice constant of the growing layer in the growth plane is accommodated to that of the substrate, inducing an **elastic deformation.** The elastic strain energy stored in the layer volume depends on *f* and increases proportionally with the layer thickness *h*, and is given by:

$$\varepsilon_e = \frac{hf^2 E}{(1-\nu)} \qquad \textbf{(Eq. I.4)}$$

E is the Young Modulus and *v* the Poisson's ratio of the epilayer. This corresponds to what is called ***pseudomorphic*** growth. Whether the lattice constant of the epi-layer is smaller ($f < 0$) or larger ($f > 0$) compared to that of the substrate, the strain is named "tensile" or "compressive", respectively. As the epilayer growth continues and *h* increases, the stored energy continues to increase until a certain "critical thickness" where two different strain relaxation modes, plastic or elastic, can occur. This gives rise to three growth modes, depending mainly on the mismatch and the growth conditions for the III-V heteroepitaxy case (figure I.6 a, b and c).

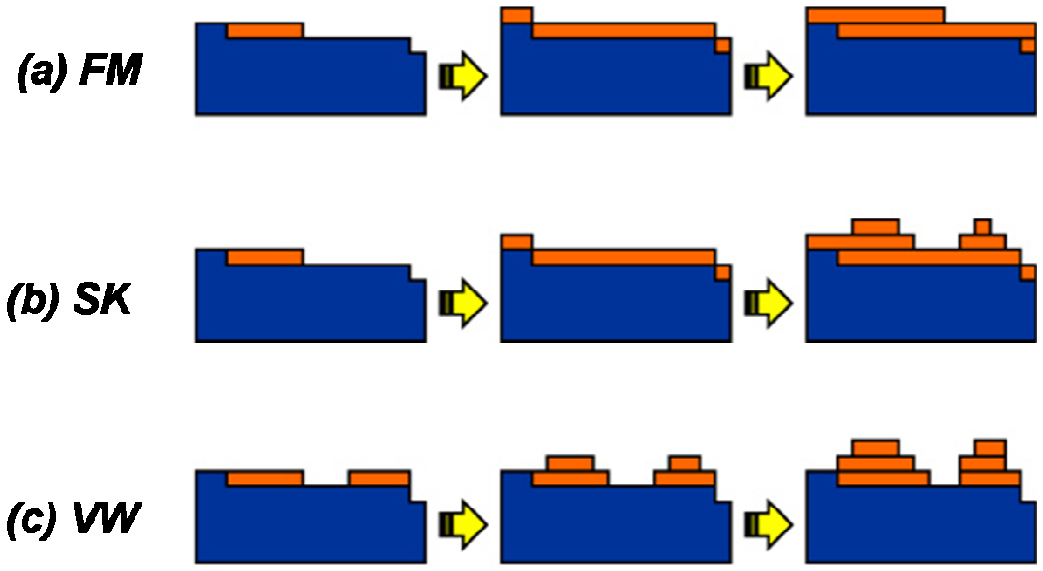

Figure I.6*: Thermodynamic thin film growth modes. (a)'Frank-van der Merwe' (layer or two-dimensional) growth, (b)'Stranski–Krastanov' (combined layer + island) growth and (c) 'Volmer-Weber' (island or 3-dimensional) growth [39].*

2D growth mode for low mismatched systems (< 2%)

For this growth mode, the formation of misfit dislocations (MDs) is energetically favoured at the critical thickness. The formation of MDs releases part of the strain energy via a

plastic deformation of the layer. (fig. I.6a). The mismatch is then accommodated by the residual elastic deformation and the plastic deformation defined by:

$$\varepsilon_s = \rho b_R \qquad \textbf{(Eq.I.5)}$$

(where ρ is the dislocation density and b_R is the Burgers vector component relaxing the strain). As we continue increasing the material thickness, more misfit dislocations are generated until a certain density ρ_c where the strain is fully relaxed and the epi-layer regain its normal lattice constant.

Many studies were developed to determine the "critical thickness" in the 2D growth mode. We mention here the well-known model of Matthews et al. [40] where the critical thickness h_c for the introduction of 60° dislocations is given by:

$$h_c = \frac{b(1-\nu/4)[\ln(h_c/b)+1]}{2\pi f(1+\nu)} \qquad \textbf{(Eq. I.6)}$$

where b is the Burgers vector, ν is the Poisson's ratio and f is the mismatch. This model considers that the growth is always 2D, based on the balance of two forces: the tension in the dislocation line and the Peach and Koelher force. The critical thickness is determined when the second force wins over the first one: the dislocation then propagates into the layer, leaving at the interface a misfit dislocation. The critical thickness h_c is then defined by the thickness of the epi-layer for which the first MD appears. Figure I.7 gives the values of h_c calculated for the $In_xGa_{1-x}As/GaAs$ system [41].

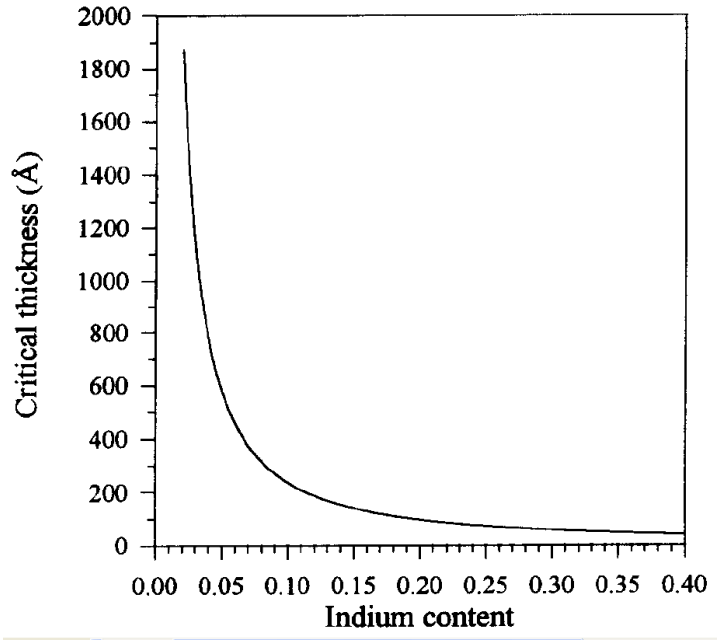

Figure I.7: *Critical thickness of InGaAs on GaAs vs. In concentration calculated with the Matthews model [41].*

One can clearly note the non-linear behaviour of the critical thickness with the In content. For $x < 0.15$, h_c increases rapidly whereas for $x = 1$, the pseudomorphic growth is limited within a few monolayers (ML for a (001) plane: 1 ML = 1 plane of III element atoms + 1 plane of V element atoms = half of the lattice constant value ~ 3 Å). This is due to the variation of the lattice mismatch going from 0 to 7.2 % depending on In content. For the ideal case, the dislocations are in the interface plane of the epi-substrate. Practically it is not always the case; some threading dislocations (TDs) propagate to the surface and deteriorate the device quality. For many researchers, the difficulty still remains in the understanding of the growth conditions to avoid deteriorating TDs and promote an ideal atomically smooth layer-by-layer growth for high quality thin films.

Stranski-Krastanov growth mode for moderate mismatches (2-6%)

When the mismatch between the epilayer and the substrate is > 2%, the growth occurs with a Stranski-Krastanov (S-K) growth mode [42]. Here, a layer-by-layer growth is unfavourable at the "critical thickness" leading to the formation of strained islands on top of the first layers (fig. I.6b). The driving force of the 2D-3D transition is the decrease of the elastic energy provided by the surfaces of the islands [43]. The transition takes place when this reduction compensates the increase in surface energy associated with the formation of islands. Hence, the thickness of the epilayer at the 2D-3D transition is much lower than the thickness h_c (where the first MD appears). For example in the InAs/GaAs system, the thickness of the 2D-3D transition was observed after 2 MLs of growth whereas Matthews' theory predicted 5 MLs [44]. Coherent strained InGaAs islands without any MD were also observed [45] with TEM (Transmission electron microscopy) images. At the same time, a theoretical study concluded that a strained film is at its minimum energy when it's a 3D morphology [46]. All these studies confirmed that the elastic strain relaxation with the formation of 3D islands is the reason of the 2D-3D transition in the S-K growth mode. Although MDs will appear after island coalescence [47] (or even before, like the case of highly mismatched materials where h_c is reached before coalescence [48]), one can see that elastic relaxation (caused by the formation of 3D islands) precedes the plastic relaxation (caused by MDs) within the S-K growth mode.

Volmer-Weber growth mode for highly mismatched systems (> 6%)

In this growth mode (fig. I.6c), strain is relaxed at the beginning of the growth; small clusters are nucleated directly on the substrate surface and then grow into nearly-fully relaxed islands

of the condensed phase. In this case, the plastic relaxation precedes any other relaxation and h_c is reached at the moment the growth begins. This growth mode is observed for very highly mismatched growth (> 6 %) where both h_c and the critical thickness are expected to be within the first monolayers.

It is clear that the growth mode depends on both elastic and plastic relaxation. Sometimes, the same system can be grown with different growth modes. Changing the growth conditions can tune the "critical thickness" of the pseudomorphic growth but also h_c. Furthermore, the nature of the misfit dislocations plays an important role on the plastic relaxation. The ability of a crystalline material to deform plastically largely depends on the nature of the dislocations that will move within this material. In the next section, we investigate the main types of MDs that are found in III-Sb semiconductors. We try to study their influence on the strain relaxation and the main mechanisms that have been used to control their formation.

I.2.A.2. Misfit Dislocations in CFC

In diamond- and zinc-blende-type lattices, perfect dislocations have Burgers vector b = 1/2<110> [49]. Three main dislocation types are generally found in III-V epi-layers: screw, edge and mixed dislocations. The edge type has the highest core energy [50] and is the one responsible of the accommodation of the lattice mismatch. These dislocations are formed by inserting an extra half plane of atoms into a perfect crystal and are marked by an edge of an incomplete plan of atoms (see figure I.8). The dislocation line corresponds to the position where the half-plane terminates. These dislocations are often represented by the symbol ⊥ where the Burgers vector is perpendicular to the dislocation line [51]. For the screw dislocations also shown in figure I.8, the Burgers vector is parallel to the interface and the angle is 0° between the dislocation line and the interface. The screw dislocation can be constructed by shearing one part of the crystal with respect to the other one within a half-plane. This dislocation type cannot relax tetragonal mismatch and is only responsible of a localized twist between the epitaxial layer and substrate [52-54]. The mixed type dislocations are decomposed into both edge and screw components where the angle between the dislocation line and the Burgers vector can be in the range of 0 – 90 degrees.

In highly mismatched (001) III-V growth the two most commonly observed dislocations are 60° and 90° MDs (or Lomer dislocations). They have a <110> type Burgers vector for a perfect

dislocation lying on (001) interface in diamond and zinc blende-type lattices, at 60° or 90° to its dislocation line. The 60° dislocation is a mixed type dislocation, with edge and screw components. In addition, the interaction of two 60° MDs (b inclined 45° at the interface) can lead to a 90° (or edge) MD formation where the dislocation line is perpendicular to the interface.

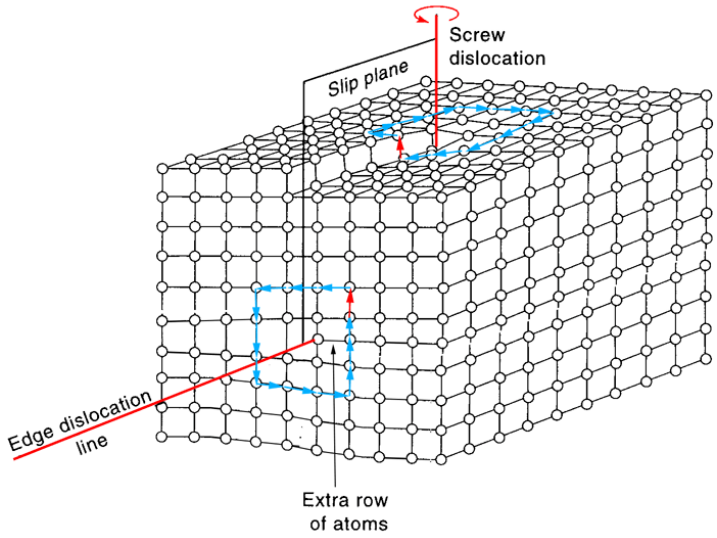

Figure I.8: *Edge and screw dislocations (Red arrows present burger vectors) [55]*

25% of the elastic energy coming from the strained layer can be transferred to a 60° MD whereas a 100% efficiency in accommodating the lattice mismatch is found in 90° MDs due to their edge Burgers vectors at the interface. At last, the 60° MDs are able to thread to the surface and thus can be responsible of many threading defects whereas 90° ones do not introduce any mis-orientation or extra stress in the system [56].

I.2.A.3. Threading dislocations (TDs) and Stacking Faults (SFs)

As mentioned above some of the MDs can usually serve as a source for threading dislocations which propagate through the epitaxial layer. An example of TDs in a 1µm thick GaSb layer grown on GaAs substrate is shown in figure I.9. We can notice in figure I.9a that some of the TDs cross the whole epitaxial layer, whereas others have their lines cut during the sample preparation. As the dislocations have a/2 <110> Burgers vectors some of them will be out of contrast in observations carried out in cross sections along <110> type zone axis. Therefore, such observation cannot be used to state the dislocation density. On the other hand, plan view image in figure I.9b shows clearly the TDs as dark dots/lines on the shiny GaAs background. This observation is the most frequently used method to determine the TD density.

Such threading dislocations are known to deteriorate device performance by forming nonradiative recombination centers and accelerate the diffusion of impurities along their line [56].

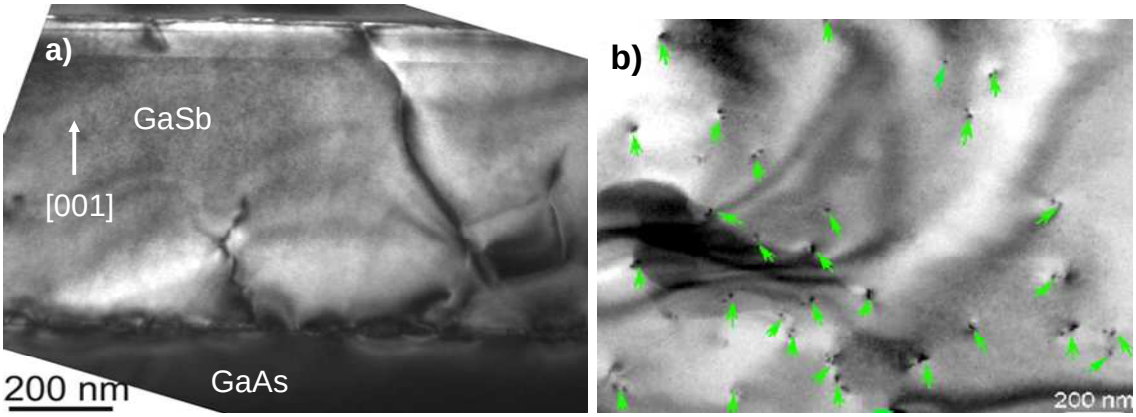

Figure I.9: *a) Cross-section images in the [110] direction and b) plan-view images recorded close to the [001] growth axis showing TDs in 1μm of GaSb on GaAs [58].*

Stacking faults (SFs) are other damaging planar defects that can appear during growth. We consider that figure I.10a [59] shows the formation of a face centered cubic (fcc) lattice. The atoms of the second layer (black, or B) sit in the holes formed by the atoms of the first layer (labeled A) and the atoms of the third layer (C) sit in the holes formed by the atoms B, the structure is hence repeated (ABCABC…). The term stacking fault (SF) implies that there is a local interruption in the regular stacking sequence and that this continues in the same manner after the SF (ABCBCABC…). In III-V semiconductors, the stacking of the zinc blende structure is usually in the [111] directions. Due to the glide of the dislocations, SFs are created by the dissociation of perfect dislocations into partial dislocations.

Another type of plane defect resulting from a change in the stacking sequence is the microtwin. In zincblende, it occurs almost exclusively on (111) planes. Here the normal crystal and its twin share a single plane of atoms and there is reflection symmetry about the twinning plane (fig. I.10b). Figure I.10c exhibits an example of a plan-view TEM image of plane defects coming from the change in the stacking sequence during Si growth. By a simple change of the diffraction vector of the image (figure I.10d), one can see that some defects completely vanish whereas the medium sized defects stay in contrast.

These last defects were determined as microtwins whereas the vanished ones are SFs [60]. A contrast image change is usually the only method to distinguish these two types of defects.

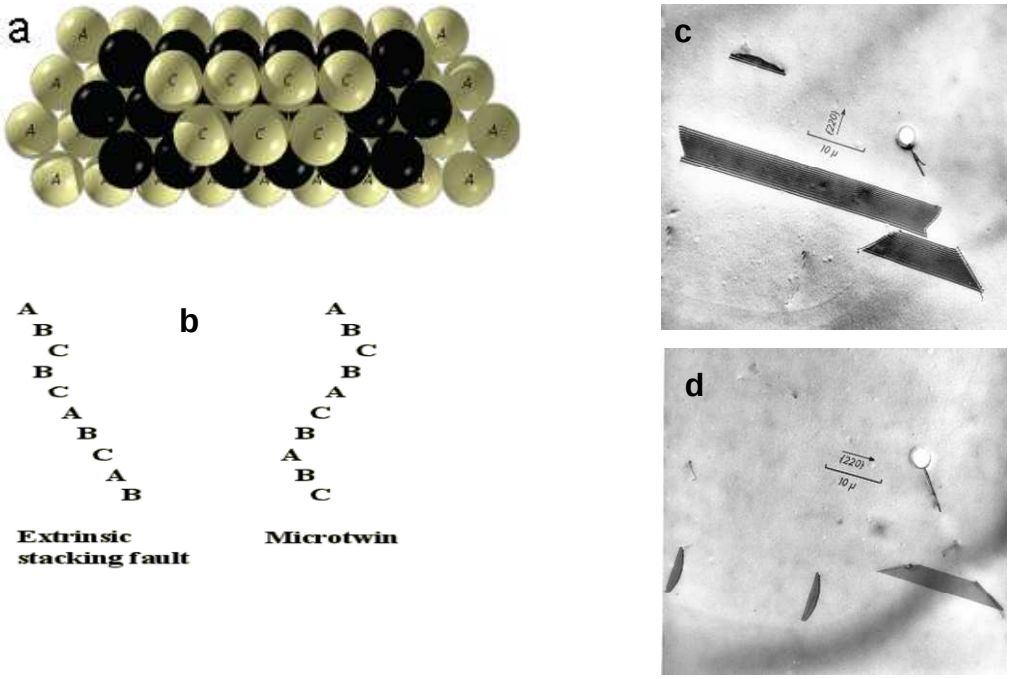

Figure I.10: ***a)*** *stacking sequence of fcc [58],* ***b)*** *is the sequence difference between a Microtwin and a stacking fault ,* ***c)*** *and* ***d)*** *Plan-view TEM image of planar defects in Si with a different contrast image [60].*

Furthermore, whereas some observations showed that devices containing stacking faults still worked, the ones with a microtwin inside were electrically faulty. For instance, Mishima et al. demonstrated that the distribution of the microtwins in InSb/$Al_xIn_{1-x}Sb$ quantum wells grown on (001) GaAs substrates correlates with the measured anisotropic electron mobility in the quantum well [61].

While it may appears that the metamorphic approach could provide any lattice constant by eliminating the mismatch problem with the substrate, we have demonstrated that other problems occur. Since some dislocations can thread in the layer volume and be the cause of the deterioration of the device performance, scientists tried to use different methods to accommodate the mismatch strain without any influence on the quality of the epi-layer. In the next part, we present two main methods that were previously developed to solve the metamorphic growth of III-Sb problems on highly mismatched III-V substrates.

I.2.B. Growth of Al(Ga)Sb on GaAs

I.2.B.1. Gradual metamorphic growth

In the goal of accommodating the mismatch strain, researchers have attempted to mitigate the detrimental defects by bending the vertically propagating defects along strained

interfaces using compositionally graded-layers [62-63]. Figure I.11 shows an example of the growth of an AlGaAsSb metamorphic buffer layer on a GaAs substrate. By optimizing the Sb compositional grading and the thickness of each buffer layer, they increased the lattice mismatch from 5.65 Å for GaAs to an almost strain-free 5.77Å matrix for $Al_{0.5}Ga_{0.5}As_{0.76}Sb_{0.24}$ (lattice matched to $In_{0.26}Ga_{0.74}As$). With this kind of buffer, InAs QDs lasers on an AlGaAsSb metamorphic buffer layer were successfully achieved [64].

While this approach has enabled a number of device demonstrations [65,66] by perfectly relaxing mismatch strain, it reveals several inefficiencies. At every strain relief of two buffer-layers (with a mismatch less than 2%) only 60° MDs are generated [67] and a high density of TDs (~10^9/cm^2) at low layer thickness is still observed. Thicker buffer layers (> 1 µm) are hence used to decrease this density [68]. However, the increase of the buffer thickness will also lead to a poor thermal and electrical conductivity making this method not very satisfying.

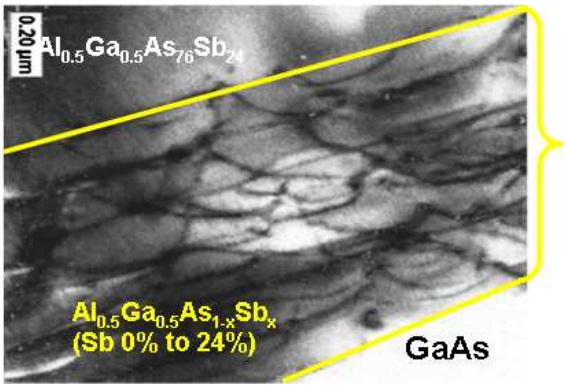

Figure I.11: *AlGaAsSb on GaAs using compositionally graded-layers [64].*

I.2.B.2. Misfit disclocation array growth mode

In 1992, Bourret and Fuoss claimed that in order to produce an epitaxial layer without defects in the case of highly lattice mismatched materials, a growth process that enables the formation of a 2D network of 90° MDs at the substrate-layer interface is needed [69]. Due to their sessile nature and their efficiency for strain accommodation, the 90° (or edge) MDs will relax all the strain coming from the mismatch at the interface in both [110] and [1-10] directions leading to strain free layer-by-layer growth. Since reports showed that low strain (< 2%) resulted in 60° dislocations, moderate strain (3%–6%) in mixed 90° and 60° dislocations, and high strain (>6%) in pure 90° [70], this growth process is promoted in heteroepitaxy for highly mismatched systems. However, the difficulty remains in understanding the growth mechanisms that can lead to the best atomic configuration at the interface to perfectly relax

strain by 90°MDs without any TDs. For example, Rocher et al. [71-73] have shown in the GaSb/GaAs system that the growth temperature is a strong factor in determining which kind of MDs is found at the interface. GaSb growth at 420-470°C favours 90° MDs whereas higher temperatures (> 510°C) promote 60° MDs. Furthermore, a high density of TDs was still observed in both cases even if 90°MDs do not propagate to the surface of the film [74]. These studies lead to the conclusion that the creation of regular arrays of 90° MDs appears to be directly related to the generation of island growth [75]. On the other hand, threading dislocations are believed to come from 60° MDs which are created at the edge of {111} planes during coalescence of large faceted irregular shape islands [76]. Therefore, the reduction of threading dislocations in large lattice mismatched growth will depend on having perfect 90° MDs at the interface with nearly no island formation. More precisely, one would hope to grow highly mismatched materials within the 2D growth mode. In the following, we try to present some of the attempts that have been previously used in the growth process on highly mismatched systems.

I.2.B.2.1. InAs on GaAs(P)

Tournié et al. [77,78] compared the growth of InAs on GaAs using the S-K and the 2D growth modes. They reported that with an As_4/In ratio of 10 a S-K growth mode appears leading to the formation of 60° MDs at the edge of the islands which then glide to the interface to relieve the strain (figure I.12a). Both 60° MDs and few 90° dislocations are detected at the interface with a dislocation spacing of 4 nm. On the other hand, when the As_4/In flux ratio is set to 0.7 inducing In-stable surface conditions, a 2D growth mode is forced. Only pure edge 90° MDs are located at the substrate epi-layer interface with a dislocation spacing of 8 nm (figure I.12b).

Chang et al. [79] studied the case of the largest lattice mismatch among all the arsenides and phosphides: InAs on GaP (mismatch = 11%). Like the InAs/GaAs system, they claimed by means of RHEED observations that for In-rich conditions a 2D growth mode appears (fig. I.13a) whereas a 3D island growth occurs under As-rich conditions (fig. I.13b). In both cases, a regular network of pure 90° MDs with a spacing of 4 nm was formed directly at the interface, which corresponds to 85% of strain relaxation. However, in the 3D growth mode, island coalescence can induce stacking faults at the boundary between two islands as observed in TEM images. In 2D growth mode, the 25-nm-thick InAs epilayer appears clean with very few

defects detected. No threading dislocation is observed but a couple of stacking faults are present in the interfacial region.

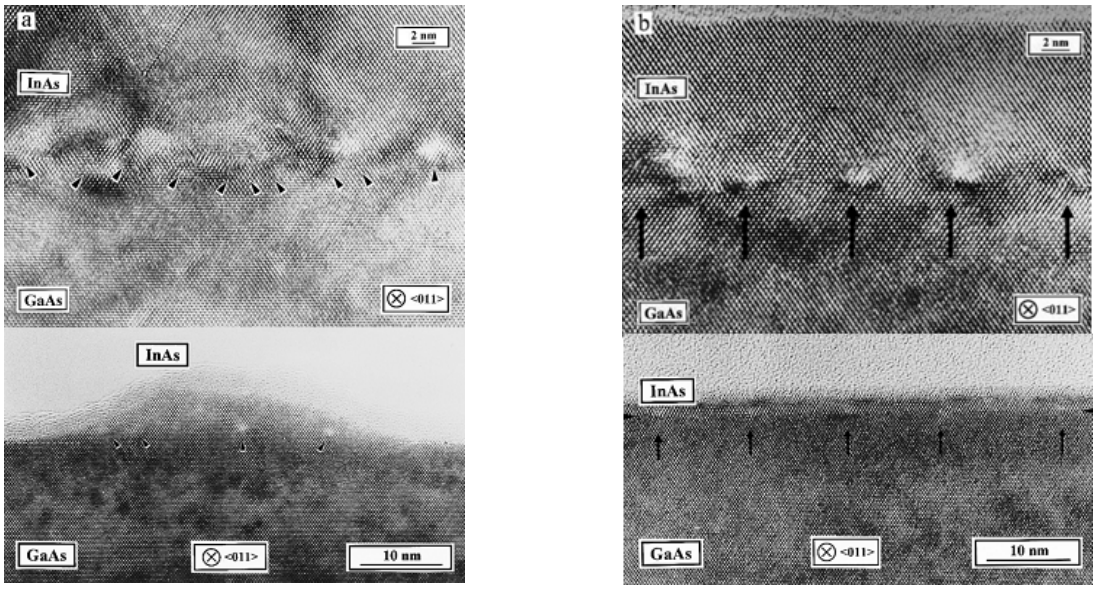

Figure I.12: *TEM images of InAs growth on GaAs by* ***a)*** *S-K growth mode and* ***b)*** *2D growth mode [77].*

The studies reported on the InAs/Ga(As, P) systems have shown that the ideal conditions to have a network of 90 ° MDs at the interface is to use In-rich conditions. Working with these conditions is however critical since the V/III ratio can be less than unity and lead to the formation of In droplets at the surface.

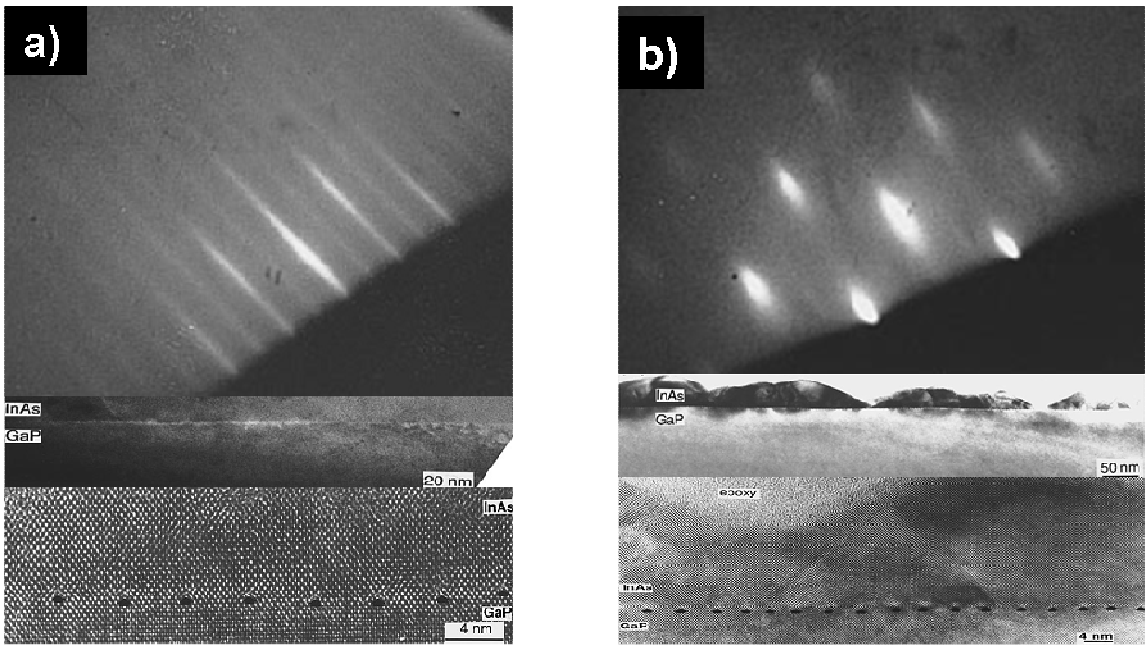

Figure I.13: *TEM images of InAs growth on GaP by* ***a)*** *2D growth mode and* ***b)*** *S-K growth mode [79].*

I.2.B.2.2. GaSb on GaAs

Later on, Huang et al. [80] reported in 2006 on the growth relaxation of GaSb on GaAs via interfacial 90° misfit dislocations (IMF) along both [110] and [1-10] directions. A planar growth mode is established after 3 MLs and a low dislocation density is obtained for bulk GaSb with a relaxation > 98% (figure I.14a). Actually, for a 100% relaxation of the GaSb overlayer, the theoretical distance between two 90° dislocations is given by:

$$S = \frac{b}{f} = \frac{a_f \times a_s}{\sqrt{2}(a_f - a_s)} \qquad \textbf{(Eq. I.7)}$$

where b is the Burgers vector, f is the lattice mismatch between the layer and the substrate and a_f and a_s are the layer and substrate lattice parameters respectively.

They measured a misfit separation of 56 Å corresponding exactly to 13 GaSb lattice sites and 14 GaAs lattice sites. In the [1-10] direction, every 14th Ga atom has a pair of dangling bonds (one going into and out of the image plane) to accommodate the larger Sb atom in the next (001) plane [81] (figure I.14b).

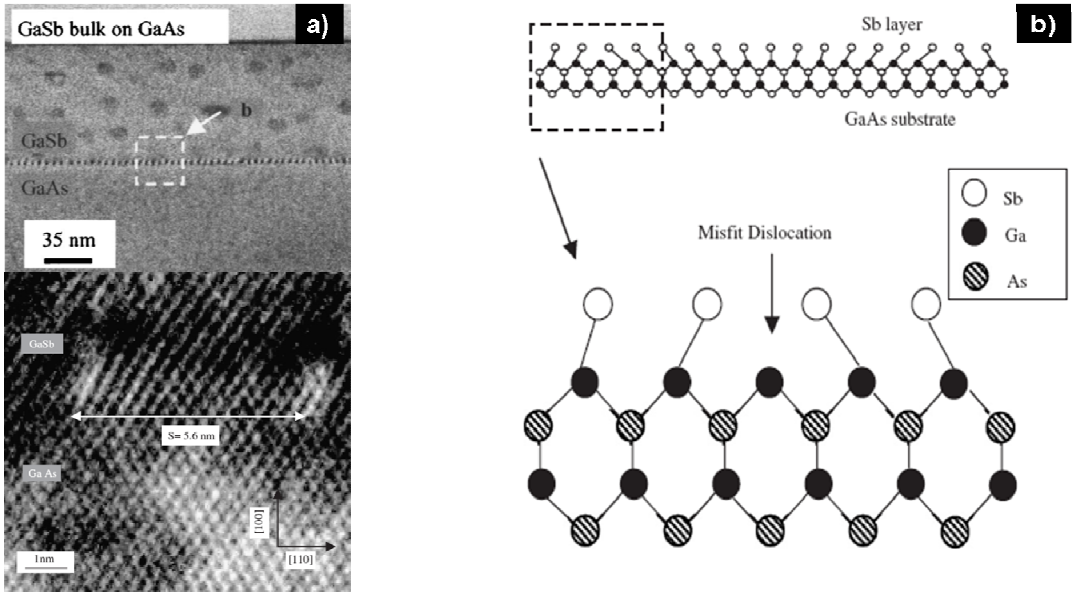

Figure I.14: a) *TEM image GaSb/GaAs interface via 90°MDs array* ***b)*** *Atomic configuration of a 90°MDs array at the GaSb/GaAs interface [80,81].*

It was then shown that a high V/III ratio (10) produces strain-relieved QDs by IMF and the low V/III ratio of 1 establishes highly strained QDs by SK (fig. I.15a) [82, 83].

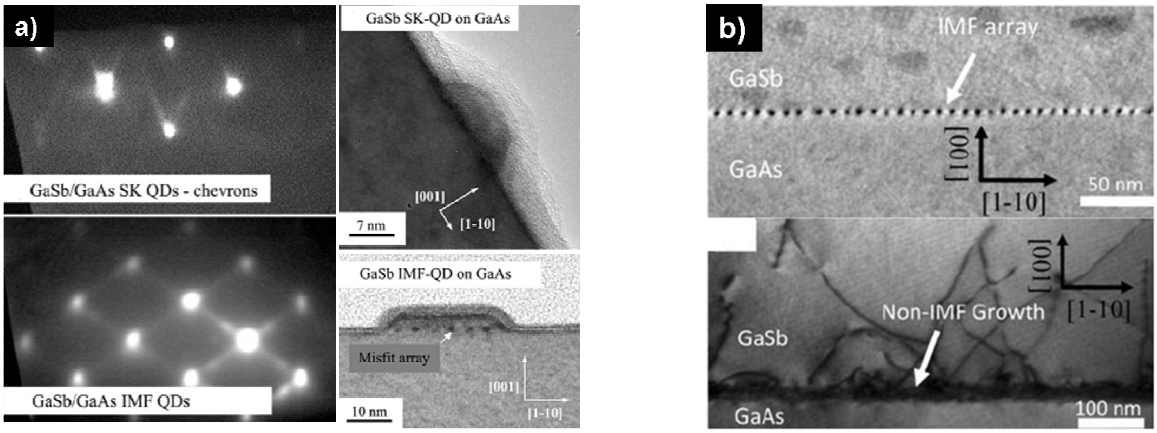

Figure I.15: *TEM images of* ***a)*** *GaSb islands growth on GaAs via IMF and Sk growth modes [82,83];* ***b)*** *Growth of GaSb islands after Sb deposition on a Ga-rich (1) and an As-rich (2) GaAs surface [84].*

Further experiments demonstrated that the initial surface preparation of GaAs also influences directly the growth mode of GaSb islands on GaAs. In the IMF growth, a sheet of Sb atoms are deposited on a Ga-rich GaAs surface before starting the GaSb growth. If Sb is deposited on an As-rich GaAs surface instead of on a Ga-rich one, the resulting epitaxial layer will have high defect density as shown in the TEM image of figure I.15 b [84].

After all these studies, a considerable progress was made in growing GaSb layers directly on (001) GaAs substrates. Results indicate that the IMF-grown GaSb is nearly-fully relaxed (98.5 %) with low density of threading dislocations (~ 10^6 cm^{-2}) and laser emission in the infrared has been recently demonstrated [85]. Even though these studies showed promising results, the optimized growth process leading to the formation of a high quality IMF array are still unclear. For instance, both 2D and 3D growth modes are reported for the same experimental conditions (see refs [80] [82]). The (4x2) Ga-rich GaAs surface reconstruction is observed at 510°C [80] in opposition with usual reported results. Furthermore, the TD density is based on scanning different areas of the wafer and only 1x1 μm^2 plan-view TEM images are shown.

The best way to grow III-Sb on mismatched III-V substrates can be achieved by forming a 90°MD array at the interface. This will better relax the epi-layer with lower threading defects and higher device performance, while avoiding the mismatch problem at the same time. However, the growth mechanisms that can lead to this goal are still unclear. Depending on the choice of the constituent elements of the substrate and epi-layers material, these mechanisms change. A detailed understanding of this growth mode is required.

I.2.C. Growth of Al(Ga)Sb on Si

I.2.C.1. Antiphase domains (APDs)

Beside the lattice mismatch, another challenge related to the growth of III-V semiconductors on Si is the formation of Antiphase Domains (APDs). If the growth is started with simultaneous exposure of III and V atoms on a Si surface, both III-Si and V-Si bonds can be formed from the initial layer on two different areas of the substrate. For example when GaAs is grown on a GaAs substrate, the Ga and As atoms experience no difficulty in choosing lattice sites: the epilayer just mimics the crystalline structure of the substrate. However, when epilayers of GaAs are grown on Si (100), Ga and As atoms can exhibit ambiguity in choosing lattice sites. The lattice sites on the (100) planes of Si are indistinguishable and there are no preferential nucleation sites for Ga and As since silicon bonds well to both of them [86].

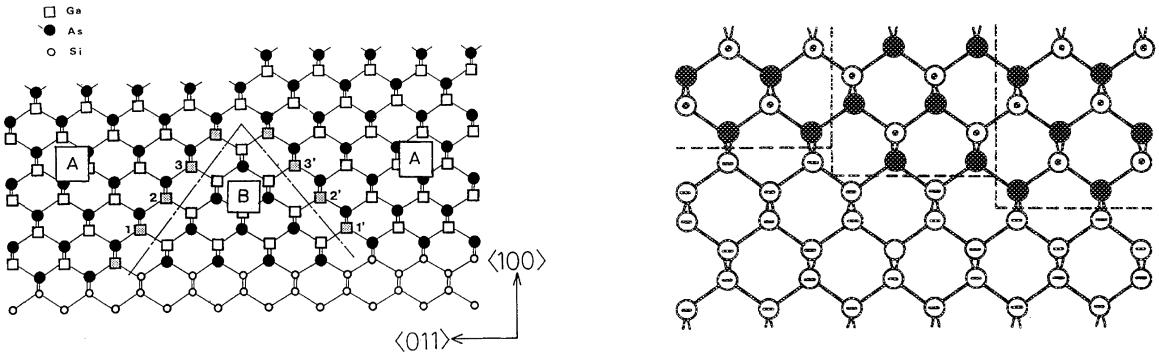

Figure I.16: a) *Anti-phase Boundaries in GaAs on (001) Si and* ***b)*** *Anti-phase domain formation on (001) Si with surface steps [86,87].*

As illustrated in figure I.16, when two areas with different nucleation atoms meet, this results in an As-As and a Ga-Ga faulty bonds. These types of bonds are called anti-phase boundaries (APBs) and the domains themselves are called anti-phase domains (APDs). Since silicon is usually grown with at least a single step height of one atomic layer, extensive APDs are observed in the growth of all polar III-V semiconductors on Si. In figure I.16b, the III-V takes its zinc blende structure in every domain but from one area to another, adjacent to it, the crystal structure rotates by 90°. This III-V symmetry breaking has shown to lead to the degradation of optical and electrical quality of the deposited material. In order to grow APD free layers, it is very important to get a Si surface with biatomic steps. At least two main methods are commonly used to eliminate these APDs. The first one is a high temperature Si annealing. Sakamoto et al. for example indicated that surface steps have been changed from monoatomic

layer to biatomic layer height by annealing Si (001) at a temperature of 1000°C for 20 min [88]. The second method uses the growth of the III-V on different crystallographic orientation substrates in a way that APDs will disappear. Uppal et al. [89] showed that after a thin deposition (0.1 μm) of GaAs/(Al,Ga)As supperlattices on a (211) Si substrate, the growth becomes perfectly homoepitaxial while maintaining both structural and electrical proprieties of the epi-layers.

An example of using these 2 methods is given on figure I.17. Through a combination of slight mis-orientation and a high-temperature surface annealing, Kroemer et al. proposed a nucleation process which leads to the pairing of all Si surface steps into a particular kind of double-height steps [90].

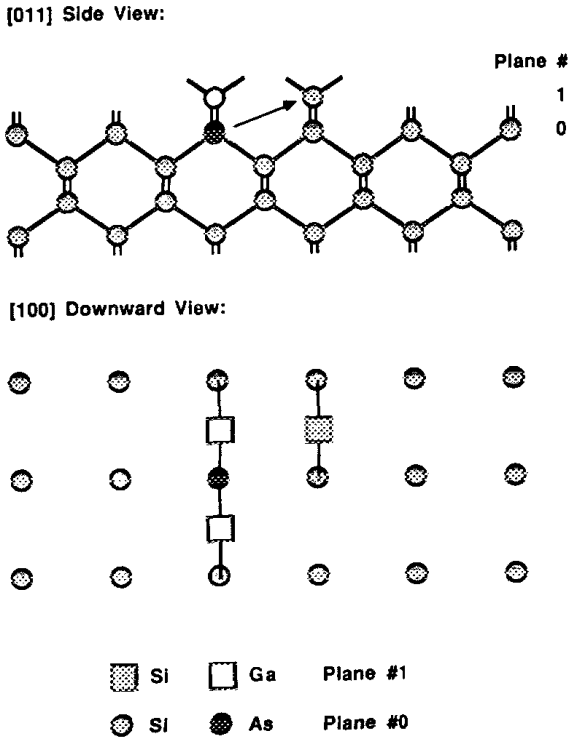

Figure I.17: *Proposed first stage of the nucleation of GaAs on Si under Ga·rich conditions: An incoming As atom interchanges sites with a Si atom in plane #0 (the original top Si plane), simultaneously bonding two "waiting" Ga atoms. The ejected Si atom is placed on an adjacent site in plane # l. Top: [011] view. Bottom: [100] (i.e., downward) view [90].*

They claimed that under Ga-rich conditions, first incoming As atoms will not simply bond to Si in the plane above the original Si surface, but will undergo an exchange reaction with a Si atom from the last Si plane. Two Ga atoms are simultaneously bonding to both the embedded As atom and to two adjacent Si atoms of the original surface. This energetic growth

mechanism proved that by lowering one of the double step energy, single domain growth of GaAs on Si can be achieved.

I.2.C.2. III-V direct growth on (001) Si

Many attempts have been reported to integrate directly III-V semiconductors on exactly oriented (001) Si. The GaAs/Si system has been a very popular research topic in III-V crystal growth. The dislocation densities of GaAs films grown by several methods (two-step growth technique [91] thermal annealing [92] and use of pseudormorphic supperlattices [93]) have been limited to a dislocation density in the order of 10^6 cm^{-2}. To our knowledge, the lowest density (~ 10^4 cm^{-2}) was obtained for the films grown at a low-temperature of 330 °C with atomic hydrogen irradiation [94].

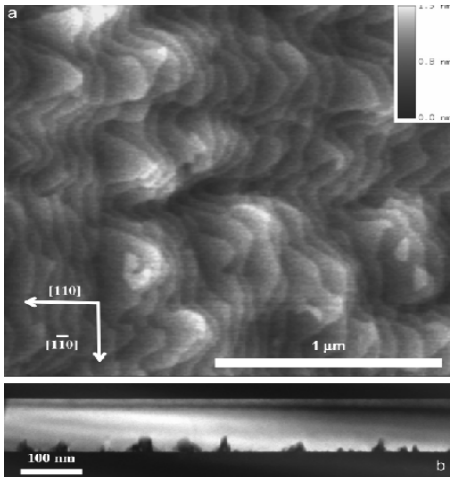

Figure I.18: *AFM and cross-section TEM images showing low density of APDs in the GaP layer on Si [96].*

In the same vein, Kunert et al. recently grew low lattice mismatched GaP on Si by metal organic vapor-phase epitaxy (MOVPE) [95,96]. Their goal was to avoid TDs related to the lattice mismatch by the pseudomorphic nucleation of GaP on Silicon. The objective is the monolithic co-integration of III/V-based optoelectronics and Si-based microelectronics on Si substrates. They demonstrated that under appropriate growth conditions a kinking of APBs appears from the {110} towards the {111} planes and hence the self-annihilation of these defects can be initiated. Furthermore, the Si surface area covered by monolayer high islands should be as small as possible to initiate self-annihilation of the APBs. APD-free GaP layers on exactly oriented (001) Si substrates have been achieved after only 40 nm of overgrowth (figure I.18).

For the III-Sb case, a few attempts have been reported on (Ga,Al)Sb [97-100] and InSb [101-102] on (001) Si substrates. Akahane et al. [97] found that GaSb grown directly on the Si substrate forms large islands, indicating excessive surface diffusion of Ga atoms on Si surface. AlSb growth leads to small islands because of the smaller diffusion length of Al atoms. Hence, they grew GaSb on Si with an AlSb initiation layer. Further TEM studies then revealed that a low-temperature AlSb buffer introduces a perfect 90° MDs array at the interface (fig. I.19a) and helps in converting the GaSb growth mode from a 3D island growth mode to a layer-by-layer one [98]. More recently, Vajargah et al. [99] investigated the IMF dislocation array at the GaSb/Si interface with an AlSb layer in between using the geometric phase analysis (GPA) method (see explanation chapter II) on HAADF-STEM images (fig. I.19 b,c and d).

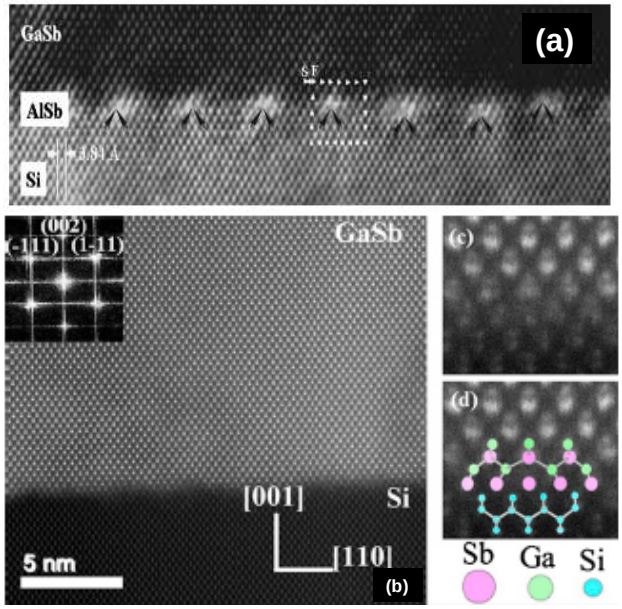

Figure I.19: a) *90° MDs array at the GaSb/AlSb/Si interface showing a high quality GaSb epi-layer [98],* ***b)*** *Cross-sectional HAADF-STEM image of a GaSb epitaxial film on Si with FFT in inset,* ***c)*** *A magnified image of misfit dislocation core and* ***(d)*** *the atomic model representation of the dislocation core structure [99].*

The atomic model reconstruction of the core structure reveals that it is a glide set type of dislocation core consisting of a ring of eight atoms and an inner atom with dangling bonds. By inspecting the first monolayer at the interface, it was inferred that the core is an Sb column.
The GPA measurements (fig. I.20) indicates that the lattice parameter of the epitaxial film recovers its bulk value within three unit cells from the interface due to the relaxation through

IMF dislocations. The standard deviation of strain in both film and substrate sides is less than 0.4%.

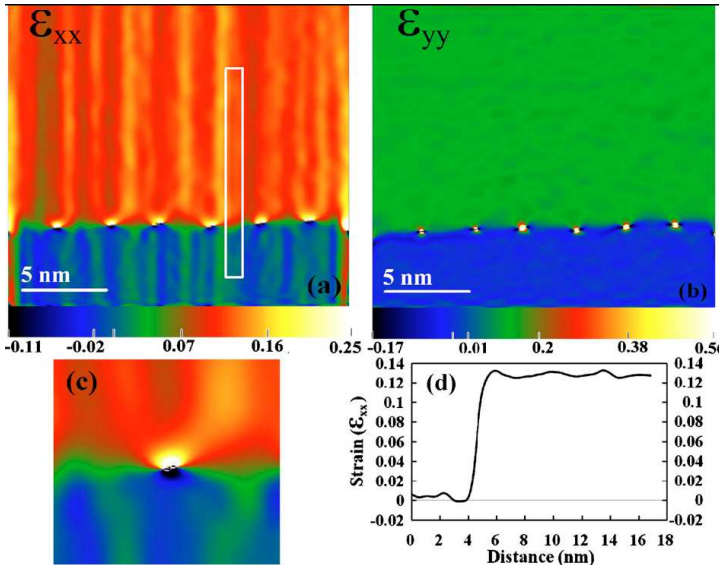

***Figure I.20**: The strain map (a) parallel, ε_{xx} with and (b) perpendicular ε_{yy} to the interface. (c) Strain in a dislocation core. (d) Line profile of the ε_{xx} strain vs distance from highlighted area in (a). The vertical modulations are the residual electron beam instabilities of the scan coils in the unprocessed images [99].*

Afterwards, a study on the TD density and APDs using IMF growth was established on AlSb on a 5° miscut (001) Si substrate [100]. In figure I.21, the high quality IMF interfaces exhibited a distance between two dislocations of 3.46 nm corresponding exactly to 8 AlSb lattice sites grown on 9 Si lattice sites.

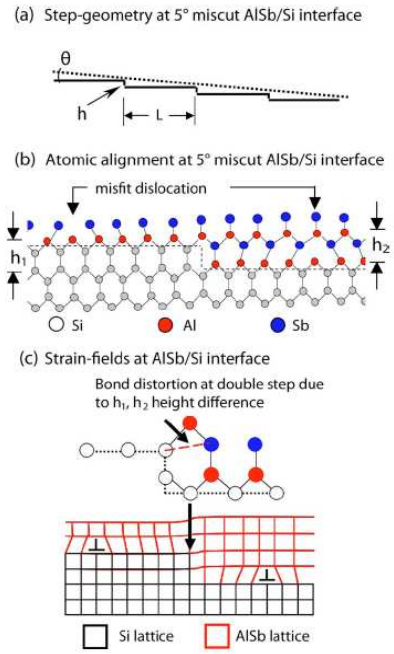

***Figure I.21:** Schematics showing the step geometry and atomic arrangement of AlSb on 5° miscut Si [100].*

This distance was well matched to the terrace length (L =31.09Å) of the 5° miscut Si substrate and results in a single interface MD per terrace. Furthermore, the miscut substrate geometry suppresses APD formation due to the double step height. Based on all these studies, the surface morphology became flatter and high-quality GaSb growth was achieved for a low defect density of ~7.10^5/cm^2 and an average APD density of ~10^3/cm^2.

From the above observations, we have pointed out the main problems related to the growth of antimonides directly on Si. Even though some attempts on growing antimonides have been already reported with very low TD densities and APDs when a 5° miscut (001) Si substrate is used, exactly oriented Si substrates are the standard ones in the current Si technology. Therefore, the need of growing III-Sb on exactly oriented (001) Si is very relevant to achieve a reproducible technology for the integration of high speed and low power Sb-based electronic devices.

I.3. Conclusions and thesis objectives

We have shown the importance of growing III-Sb on GaAs and Si substrates for both optoelectronic and electronic devices. After exploring the main problems related to the growth of III-Sb materials on highly lattice mismatched substrates, one can conclude that two major difficulties remain: TDs coming from the mismatch and APDs coming from the growth of a polar (III-V) on a non-polar material in the case of the use of Si substrates.

Since interesting results have been demonstrated for the growth of GaP templates on (001) Si, we focus on the former bottleneck by treating the cases of Sb-based heterostructures on GaAs and GaP substrates.

In order to achieve a pure antimonide buffer layer, we will first try to perfectly control its growth on highly mismatched III-V materials. Since GaAs is a commonly used substrate in the industry, we particularly try to investigate the growth conditions (surface preparation, growth rate, growth temperature and V/III ratio) that can lead us for a high quality GaSb layer on a GaAs substrate. At the same time, we will present the growth of GaSb on GaP, increasing then the mismatch with the substrate to 11.7 %. With the help of these 2 studies we hope to be able to explain the main mechanisms to reach a perfectly 90°MDs array at the GaSb/Ga(As,P) interface. We can also wish to reveal new aspects which may lead to a better understanding of the III-Sb heteroepitaxial growth.

After optimizing the growth conditions of the buffer layers, we study their impact on the active layers. Therefore, we present the results of an AlSb/InAs heterostructure growth on both GaAs and GaP surfaces. In this phase of work, it is important to mention that even if we decided to work on a specified active layer used mainly for electronic applications (AlSb/InAs), our results can be extended to other III-Sb active layers.

At the end of this work, we show our attempt to grow an AlSb/InAs heterostructure on an exactly oriented silicon substrate by using GaP/Si templates from the $NASP_{III/V}$ GmbH company in Marburg. We demonstrate that the result is very promising for the integration of high speed and low power Sb-based electronic devices in the silicon technology.

References

[1] C. Kittel, « Physique de l'état solide », Dunod (2007)

[2] http://cnx.org/content/m16927/latest/

[3] S. Adachi, "Properties of semiconductor alloys: group IV, III-V and II-VI semiconductors", Wiley (2009)

[4] http://lab.frumania.com/tag/semiconductor-bandgap-energy-vs-lattice-constant/

[5] I. Vurgaftman, J. R. Meyer and L. R. Ram-Mohan, J. Appl. Phys. **89** (2001) 5815

[6] H. Kroemer, Physica E **20** (2004) 196

[7] C. Renard, PhD in materials science "Hétérostructures antimoniures/arséniures pour les applications optoélectroniques dans le moyen infrarouge", University of Paris VII, September (2005)

[8] M. E. Flatté, C. H. Grein, H. Ehrenreich, R. H. Miles and H. Cruz, Theoretical, J. Appl. Phys. **78** (1995) 4552

[9] C. H. Grein, P. M. Young and H. Ehrenreich, J. Appl. Phys. **76** (1994) 1940

[10] E. R. Youngdale, J. R. Meyer, C. A. Hoffman, F. J. Bartoli, C. H. Grein, P. M. Young, H. Ehrenreich, R. H. Miles and D. H. Chow, Appl. Phys. Lett. **64** (1994) 3160

[11] A. Joullié, E. M. Skouri, M. Garcia, P. Grech, A. Wilk, P. Christol, A. N. Baranov, A. Behres, J. Kluth, A. Stein, K. Heime, M. Heuken, S. Rushworth, E. Hulicius and T. Simecek, Appl. Phys. Lett. **76** (2000) 2499

[12] W. W. Bewley, H. Lee, I. Vurgaftman, R. J. Menna, C. L. Felix, R. U. Martinelli, D. W. Stockes, D. Z. Garbuzov, J. R. Meyer, M. Maiorov, J. C. Connolly, A. R. Sugg and G. H. Olsen, Appl. Phys. Lett. **76** (2000) 256

[13] R. Teissier, D. Barate, A. Vicet, D. A. Yarekha, C. Alibert, A. N. Baranov, X. Marcadet, M. Garcia and C. Sirtori, Electron. Lett. **39** (2003) 1252

[14] R. Teissier, D. Barate, A. Vicet, C. Alibert, A. N. Baranov, X. Marcadet, M. Garcia, C. Sirtori, C. Renard, D. Revin and J. Cockburn, Appl. Phys. Lett. **85** (2004) 167

[15] Q. Yang, C. Manz, W. Brooner, C. Mann, L. Kirste, K. Köhler and J. Wagner, Appl. Phys. Lett. **86** (2005) 131107

[16] R. Q. Yang, J. L. Bradshaw, J. D. Bruno, J. T. Pham, D. E. Wortman and R. L. Tober, Appl. Phys. Lett. **81** (2002) 397

[17] J.-B. Rodriguez, PhD in Electronic, Optronic and materials science “Superréseaux InAs/GaSb réalisés par épitaxie par jets moléculaires pour photodétection à 300 K dans le moyen-infrarouge”, University of Montpellier II, July (2005)

[18] J.-B. Rodriguez, L. Cerutti and E. tournié, Appl. Phys. Lett. **94** (2009) 023506

[19] J.-B. Rodriguez, L. Cerutti, P. Grech and E. tournié, Appl. Phys. Lett. **94** (2009) 061124

[20] J. R. Reboul, L. Cerutti, J.-B. Rodriguez, P. Grech, and E. Tournié, Appl. Phys. Lett. **99 (**2011) 121113

[21] B.R. Bennett, R. Magno, J. B. Boos, W. Kruppa and M. G. Ancona, Sol. Stat. Elect. **49** (2005) 1875

[22] L. D. Nguyen, L. E. Larson, UK Mishra, Proc IEEE **80** (1992) 494

[23] T. Ashley, A.B. Dean, C.T. Elliott, G.J. Pryce, A.D Johnson and H. Willis, Appl. Phys. Lett. **66** (1995) 481

[24] Y. Roelens, A. Noudeviwa, S. Bollaert, F. Danneville and G. Dambrine, Convention CNES 82067/00 (2008)

[25] C. A. Chang, L. L. Chang, E. E. Mendez, M. S. Christie and L. Esaki, J. Vac. Sci. Technol. B **2** (1984) 214

[26] G. Tuttle and H. Kroemer, IEEE Trans. Elect. Dev. **34** (1987) 2358

[27] A. Noudéviwa, Y. Roelens, F. Danneville, A. Olivier, N. Wichmann, N. Waldhoff, S. Lepilliet, G. Dambrine, L. Desplanque, X. Wallart, G. Moschetti, J. Grahn, IEEE Trans. Elect. Dev. **57** (2010) 1903

[28] G. Moschetti, N. Wadefalk, P.-Å. Nilsson, Y. Roelens, A. Noudeviwa, L. Desplanque, X. Wallart, F. Danneville, G. Dambrine, S. Bollaert, J. Grahn, Solid-State Electronics **64** (2011) 47

[29] G. Tuttle, H. Kroemer, J.H. English, J. Appl. Phys. **65** (1989) 5239

[30] G. Tuttle, H. Kroemer, J.H. English, J. Appl. Phys. **67** (1990) 3032

[31] C.R. Bolognesi, H. Kroemer, J.H. English, J. Vac. Sci. Technol. B **10** (1992) 877

[32] M. Johnson, B.R. Bennett, M.J. Yang, M.M. Miller, B.V. Shanabrook, Appl. Phys. Lett. **71** (1997) 974

[33] J.B. Hacker, J. Bergman, G.r Nagy, G. Sullivan, C. Kadow, H.K. Lin, A. C. Gossard, M. Rodwell, and B. Brar, IEEE Micro. IEEE Microwave and Wireless Letters **14** (2004) 156

[34] L. Desplanque, D. Vignaud and X. Wallart, J. Cryst. Growth **301–302** (2007) 194

[35] M. Thomas, H.-R. Blank, K.C. Wong and H. Kroemer, J. Cryst. Growth **175** (1997) 894

[36] M. Thomas, H.-R. Blank, K.C. Wong and H. Kroemer, Appl. Phys. Lett. **69** (1996) 2080

[37] H. Kitabayashi, T. Waho, and M. Yamamoto, Electr. Lett. 33 (1997) 102

[38] A.S. Vengurlerkar, F. Capasso and T.H. Chiu , Appl. Phys. Lett. **57** (1990) 1772

[39] M. Opel, J. Phys. D: Appl. Phys. **45** (2012) 033001

[40] J. W. Matthews and A. E. Blakeslee, J. Cryst. Growth **27** (1974) 118

[41] G. Sek, J. Misiewicza, D. Radziewiczb, M. Tłaczałab, M. Panekb and R. Korbutowiczb, Vacuum **50** (1998) 219

[42] N. Grandjean, PhD in physics "Phénomènes de surface en croissance épitaxiale fortement contrainte de (In,Ga)As sur GaAs : relaxation élastique, transition 2D-3D, effet surfactant", University of Nice-Sophia Antipolis, February (1994)

[43] D. Jacob, PhD in material science "Relaxation hétérogènes des contraintes dans les hétérostructures semiconductrices III-V : Caracérisation par microscopie électronique en transmission et simulation", University of Science and Technology Lille, February (1998)

[44] F. Houzay, C. Guille, J.M. Moison, P. Henoc, F. Barthe, J. Cryst. Growth **81** (1987) 67

[45] S. Guha, A. Madhukar, and K. C. Rajkumar, Appl. Phys. Lett. **57** (1990) 2110

[46] B. J. Spencer, P. W. Voorhees, and S. H. Davis, Phys. Rev. Lett. **67** (1991) 3696

[47] Y. Androussi, A. Lefebvre, T. Benabbas, P. François, C. Delmarre, J. Y. Laval and A. Dubon, J. Cryst. Growth **169** (1996) 209

[48] Y. Chen, X. Win, Z. Liliebtal, J. Wasburn, J. F. Klem and J. Y. Yao, Appl. Phys. Lett. **68** (1996) 111

[49] P. M. J. Maree, J. C. Barbour, K. L. Kavanagh, C. W. T. Bulle-Lieuwma, M. P. A. Viegers and J. F. van der Veen, J. Appl. Phys. **67** (1987) 4413

[50] J. P. Hirth and J. Lothe, Theory of Dislocations, 2nd ed. (Wiley, New York, 1982)

[51] A. Jallipalli, Doctor of Philosophy, optical science and engineering, "structural, electrical characterization and simulation of periodic Misfit dislocation arrays localized at the GaSb/GaAs interface", University of New Mexico, August (2008)

[52] P. M. J. Maree, J. C. Barbour, J. F. van der Veen, K.L. Kavanagh, C. W. T. Bulle-Lieuwma and M. P. A. Viegers, J. Appl. Phys. **62** (1987) 4413

[53] Vila A., Cornet A., Morante J. R., Ruterana P., Loubradou M., Bonnet R., Gonzalez Y., and Gonzalez Y., Philos. Mag. A. **71** (1995) 85.

[54] Vila A., Cornet A., Morante J. R., Ruterana P., Loubradou M., and Bonnet R., J. Appl. Phys. **79** (1996) 676.

[55] http://courses.eas.ualberta.ca/eas421/lecturepages/microstructures.html

[56] A. Rocher, E. Snoeck, Mat. Sci. Eng. **B67** (1999) 62–69

[57] J. H. Kim, T. Y. Seong, N. J. Mason and P. J. Walker, J. Elec. Mat. **27** (1998) 466

[58] Y. Wang, P. Ruterana, L. Desplanque, S. El Kazzi, and X. Wallart, J. Appl. Phys. **109** (2011) 023509

[59] H. S. Leipner course: Defects in crystals (2007)

[60] http://www.tf.uni-kiel.de/matwis/amat/def_en/kap_6/advanced/t6_3_2.html

[61] T.D. Mishima, J.C. Keay, N. Goel, M.A. Ball, S.J. Chung, M.B. Johnson and M.B. Santos, J. Cryst. Growth **251** (2003) 551

[62] G. Balakrishnan, S. Huang, T. J. Rotter, A. Stintz, L. R. Dawson, K. J. Malloy, H. Xu, and D. L. Huffaker, Appl. Phys. Lett. **84** (2004) 2058

[63] S. S. Yi, C. K. Inoki, D. L. Harris, T. S. Kuan, T. F. Kuecha and D. M. Hansen, Appl. Phys. Lett. **77** (2000) 842

[64] Y. C. Xin, L. G. Vaughn, L. R. Dawson, A. Stintz, Y. Lin, L. F. Lester, and D. L. Huffaker, J. Appl. Phys. **94** (2003) 2133

[65] P. F. Marsh, C. S. Whelan, W. E. Hoke, R. E. Leoni, T. E. Kazior, Microelectronics Reliability **42** (2002) 997

[66] H. Happy, S. Bollaert, H. Fouré and Alain Cappy, IEEE Trans. Elec. Dev. **45** (1998) 2089

[67] Y. Wang, P. Ruterana, L. Desplanque, S. El Kazzi, and X. Wallart, J. Appl. Phys. **109** (2011) 023509

[68] W. Qian, R. Kaspi and M. Skowronski, J. Electrochem. Soc. **44** 1430 (1997)

[69] A. Bourret and P. H. Fuoss, Appl. Phys. Lett. **61** (1992) 1034

[70] Y. Wang, P. Ruterana, L. Desplanque, S. El Kazzi, and X. Wallart, J. Appl. Phys. **109** (2011) 023509

[71] J. M. Kang, M. Nouaoura, L. Lassabatère and A. Rocher, J. Cryst. Growth **143** (1994) 115

[72] J. M. Kang, Suk-Ki Min and A. Rocher, Appl. Phys. Lett. **65** (1994) 2954

[73] A. Rocher, E. Snoeck, Mat. Sci. Eng. **B67** (1999) 62–69

[74] S. F. Fang, K. Adomi, S. Iyer, H. Morkoç, H. Zabel, C. Choi and N. Otsuka, J. Appl. Phys. **68** (1990) R31

[75] Vila A., Cornet A., Morante J. R., Ruterana P., Loubradou M., and Bonnet R., J. Appl. Phys. **79** (1996) 676.

[76] W. Qian, M. Skowronski, R. Kaspi, M. De Graef, and V. P. Dravid, J. Appl. Phys. **81** (1997) 7268

[77] A. Trampert, E. Tournié and K. H. Ploog, Appl. Phys. Lett. **66** (1995) 2265

[78] E. Tournié, O. Brandt, C. Giannini, K. H. Ploog and M. Hohenstein, J. Cryst. Growth **127** (1993) 765

[79] J. C. P. Chang, T. P. Chin and J. M. Woodall, Appl. Phys. Lett. **69** (1996) 981

[80] S. H. Huang, G. Balakrishnan, A. Khoshakhlagh, A. Jallipalli, L. R. Dawson, and D. L. Huffaker, Appl. Phys. Lett. **88** (2006) 131911

[81] A. Jallipalli, G. Balakrishnan, S.H. Huang, A. Khoshakhlagh, L.R. Dawson, D.L. Huffaker, J. Cryst. Growth **303** (2007) 449–455

[82] G. Balakrishnan, J. Tatebayashi, A. Khoshakhlagh, S. H. Huang, A. Jallipalli, L. R. Dawson, and D. L. Huffaker, Appl. Phys. Lett. **89** (2006) 161104

[83] J. Tatebayashi, A. Khoshakhlagh, S. H. Huang, L. R. Dawson, G. Balakrishnan and D. L. Huffaker, Appl. Phys. Lett. **91** (2007) 141102

[84] A. Jallipalli, G. Balakrishnan, S. H. Huang, T. J. Rotter, K. Nunna, B. L. Liang, L. R. Dawson and D. L. Huffaker, Nanoscale Res Lett. **4** (2009) 1458

[85] J. M. Yarborough, Y. Y. Lai, Y. Kaneda, J. Hader, J. V. Moloney, T. J. Rotter, G. Balakrishnan, C. Hains, D. Huffaker, S. W. Koch and R. Bedford, Appl. Phys. Lett. **95** (2009) 081112

[86] S. F. Fang, K. Adomi, S. lyer, H. Morko, C. Choia, N. Otsuka and H. Zabel, J. Appl. Phys. **68** (1990) R31

[87] M. Kawabe and T. Ueda, Jpn. J. Appl. Phys. **26** (1987) L944

[88] T. Sakamoto and G. Hashiguchi, Jpn. J. Appl. Phys. **25** (1986) L78

[89] P. N. Uppal and H. Kroemer, J. Appl. Phys. **58** (1985) 2195

[90] H. Kroemer, J. Vac. Sci. Technol. B **5** (1987) 1150

[91] M. Akiyama, Y. Kawarada and K. Kaminishi, Jpn. J. Appl. Phys. **23** (1984) L843

[92] M. Yamaguchi, M. Tachikawa, Y. Itoh, M. Sugo and S. Kondo, J. Appl. Phys. **68** (1988) 4518

[93] R. Fisher, H. Morkog, D. A. Neumann, H. Zabel, C. Choi, N. Otsuka, M. Longerbone and L. P. Erickson, J. Appl. Phys. **60** (1986)1640

[94] Y. Okada, H. Shimomura and M. Kawabe, J. Appl. Phys. **73** (1993) 7376

[95] I. Nemeth, B. Kunert, W. Stolz and K. Volz, J. Cryst. Growth **310** (2008) 4763

[96] I. Nemeth, B. Kunert, W. Stolz and K. Volz, J. Cryst. Growth **310** (2008) 1595

[97] K. Akahane, N. Yamamoto, S. Gozu, and N. Ohtani, J. Cryst. Growth **264** (2004) 21

[98] Y. H. Kim, J. Y. Lee, Y. G. Noh, M. D. Kim, S. M. Cho, Y. J. Kwon, and J. E. Oh, Appl. Phys. Lett. **88** (2006) 241907

[99] S. Hosseini Vajargah, M. Couillard, K. Cui, S. Ghanad Tavakoli, B. Robinson, R. N. Kleiman J. S. Preston and G. A. Botton, Appl. Phys. Lett. **98** (2011) 082113

[100] S. H. Huang, G. Balakrishnan, A. Khoshakhlagh, L. R. Dawson, and D. L. Huffaker, Appl. Phys. Lett. **93** (2008) 071102

[101] Y. H. Kim and J. Y. Lee, Y. G. Noh and M. D. Kim,Y. J. Kwon and J. E. Oh, R. Gronsky, Appl. Phys. Lett. **89** (2006) 031919

[102] M. Mori, K. Murata, N. Fujimoto, C. Tatsuyama and T. Tambo, Thin Solid Films **515** (2007) 7861

CHAPTER II: Experimental setup

II.1. Material growth: Molecular Beam Epitaxy

Molecular Beam epitaxy (MBE) is a method for single crystal deposition. It's one of the best techniques used for the production of high-quality semiconductor devices. III-V MBE was first based on the principle of the three temperatures proposed by Gunther in 1958 [1]. The method consists in making group V molecular flux reacts with another group III one evaporated at temperatures T_V and $T_{III,}$ respectively, on a substrate surface heated at a temperature T_s satisfying $\mathbf{T_{III} > T_s > T_V}$. The progress of MBE was later attributed to the work of J. Arthur and A. Cho [2-3] who demonstrated the homoepitaxial growth of GaAs buffers. They declared that once the condition of the 3 temperatures is satisfied, the group III atoms are condensed on the substrate and their re-evaporation is almost negligible. The V element is hence incorporated just to ensure the stoichiometry of the grown layer. This process implies that an excessive group V element flux is sent to the surface which requires a temperature T_S sufficiently large to prevent excessive group V condensation. The first advantage of MBE is the slow deposition rate (reaching less than 0.01 ML/s) allowing an excellent control of the layer surface and thickness. Such control has allowed the development of structures where the electrons can be confined in space, giving quantum wells or even quantum dots. The second most important aspect in MBE is the ultrahigh vacuum environment leading to different *in situ* characterisation techniques (XPS, UPS, APS, MS, RHEED...). At these very low pressures, the mean free path of the gas atoms or molecules coming from the cells is in the order of few meters. On the other hand, the distance between the cells and the substrate is very short (~30 cm). By comparing this distance and the mean free path, one can deduce that molecules arrive to the substrate surface with nearly no collisions ("molecular beam flux").

II.1.A. IEMN MBE reactors

Three MBE reactors are running at IEMN. One reactor is concerned with graphene growth experiments and two are dedicated to III-V material growth: a Solid-source MBE (SSMBE) RIBER 21 TM reactor and a Gas-source (GSMBE) MBE 32 P reactor, coupled together with an ESCA analysis chamber and both running with a base pressure better than 1×10^{-10} Torr. To obtain high-purity layers, it is critical that the material sources must be

extremely pure and the entire process be done in an ultra-high vacuum environment. The III-V MBE system consists in four main vacuum chambers: growth chamber, intermediate chamber, outgassing chamber and an introduction chamber. These chambers are separated each other by gate valves to maintain the vacuum integrity between them (fig. II.1).

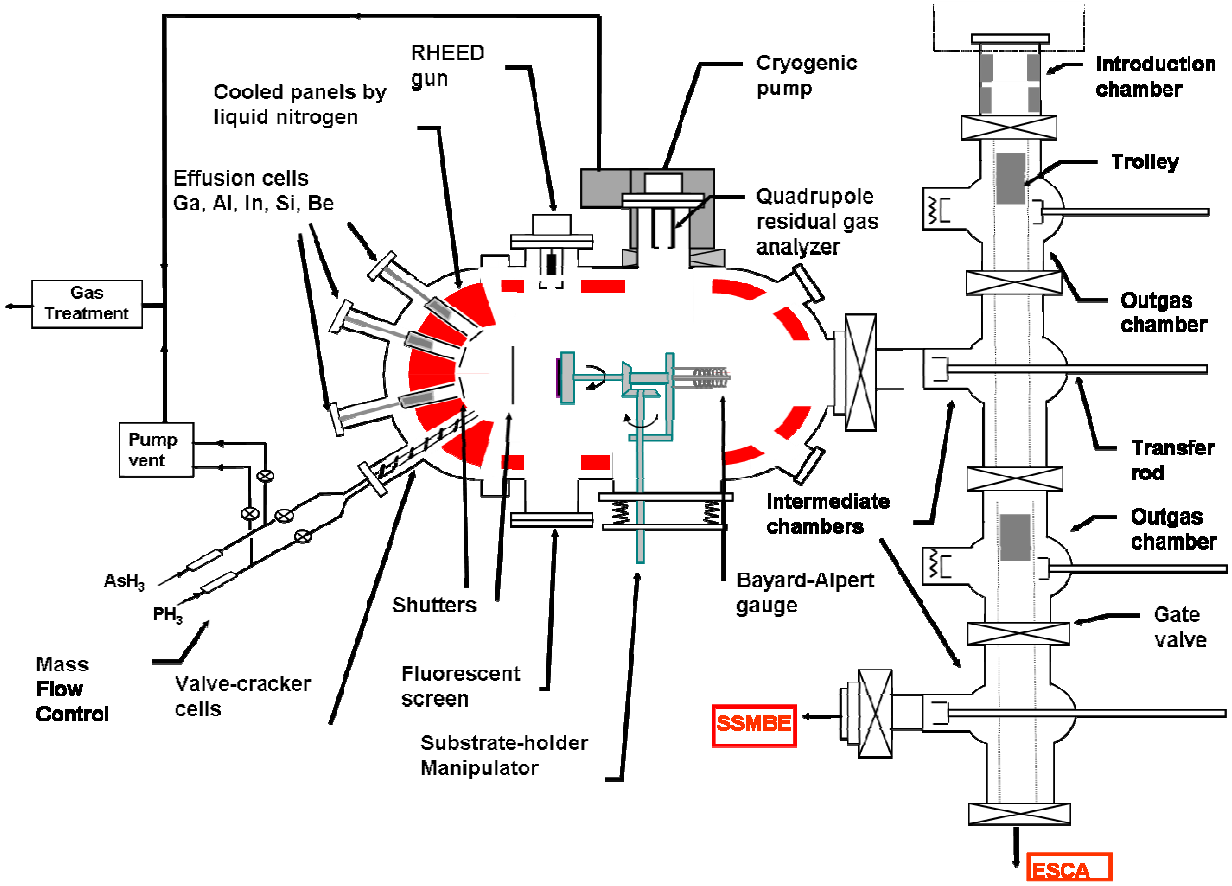

Figure II.1: *IEMN III-V MBE system. Only details on GSMBE are given since both reactors operate nearly in the same way. The difference in SSMBE is first that no P element is used and secondly, an As solid effusion cell is used as source for As_4 elements rather than arsine (which gives As_2) in GSMBE.*

II.1.B. Elemental sources

II.1.B.1. Group III element sources

The group III **element** sources are effusion cells (Knudsen type) where Gallium, Indium and Aluminum are melted and then evaporated in an atomic flux. We assume the Knudsen formula giving the atomic flux arriving on the substrate to be valid. The arriving atomic flux is then a function of the cell temperature, geometric parameters (aperture area, position in the reactor) and of the evaporated element properties (vapor pressure, molecules velocity).

$$F_i = \frac{a p_i(T)\cos\theta}{d^2\sqrt{2m_i KT}} \qquad \text{with} \qquad \log p_i(T) = \frac{X}{T} + Y\log T - Z \qquad \textbf{(Eq. II.1)}$$

where: a is the aperture area of the cell

$p_i(T)$ is the vapour pressure at T

d is the cell-substrate distance

m_i is the material mass

θ is the angle between the cell axis and the normal to the substrate

X, Y and Z are characteristic constants of the material

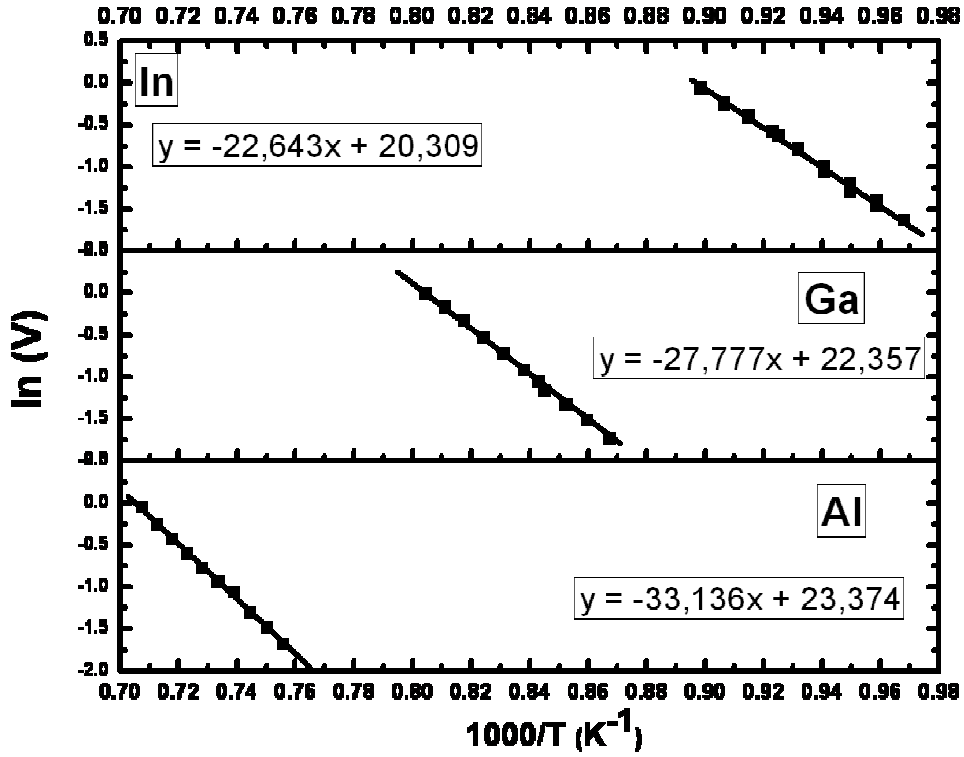

Figure II.2: *Growth rate of In on InAs, and Ga and Al on GaAs in function of the cell temperature.*

For a given reactor geometry, the atomic flux of each element is a unique function of the material temperature and hence is controlled by regulating the temperature T of the cell crucible. Figure II.2 gives an example of experimental atomic flux of the In, Ga and Al cells in function of the crucible temperature. The atomic flux (or growth rate V) is given in ML/s where 1 monolayer corresponds to a complete layer of group III and V atoms in the [001] direction (see section II.1.D). In figure II.2, the evolution of the growth rate is deduced for each cell and follows an Arrhenius law given by:

$$y = \ln(V) = A + B\left(\frac{1000}{T}\right) = A + Bx \qquad \textit{(Eq. II.2)}$$

where A and B are characteristic constants of each material, the latter having the dimensions of an activation energy divided by the Boltzmann constant. Since the cell contents evolve with time, Eq. II.2 allows us to readjust the temperature from a single growth rate measurement. For day to day control, the atomic flux is also checked with the help of a Bayart-Alpert gauge placed in front of the substrate holder.

II.1.B.2. Group V element sources

Both MBE reactors are equipped with an antimony valved cracker cell (Veeco RB 200) used as a **Sb_2** source. The cracker temperature is set at 900°C to produce **Sb_2**. Actually, decreasing the cracker temperature produces Sb_4 species but rapidly leads to a plug of the valve due to excessive antimony condensation. It has been demonstrated that the use of Sb_2 from Sb_4 is beneficial to the electronic properties of binary antimonides. Particularly, a lower concentration of native residual acceptors responsible for the p-type residual conductivity of undoped GaSb is obtained [4-5].

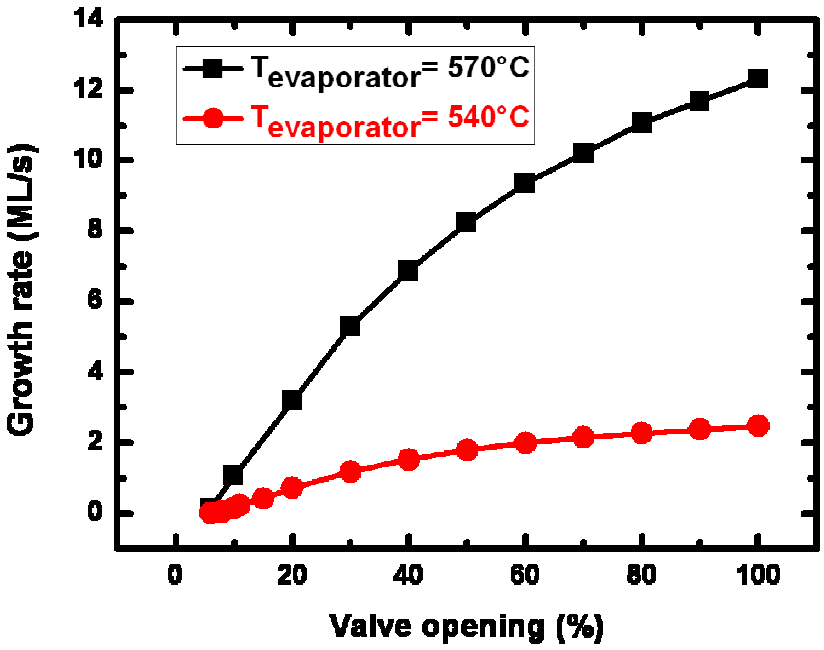

Figure II.3: *Sb growth rate in function of the valve opening at a cracker temperature of 900°C and an evaporator temperature of 540°C (red line) and 570°C (black line).*

Depending on the desired atomic flux, the evaporator temperature is changed and the valve opening is varied. The pressure is hence measured by the gauge flux and corresponds to a certain Sb growth rate (section II.1.D) on the substrate. Figure II.3 exhibits an example of the variation of the Sb growth rate on a GaSb substrate in function of the valve opening at an evaporator temperature of 540°C and 570°C. As group III element cells, the equation of each line also allows us to readjust the valve opening from a single growth rate measurement.

In SSMBE, a valved cracker cell (Riber VAC 500) is used to sublime the solid As element into tetramer $\mathbf{As_4}$ species at a cracker and evaporator temperatures of 400 and 600°C, respectively. Like in the case of an Sb cell, the calibration of the As growth rate is determined in function of the valve opening. On the other hand, the arsenic $\mathbf{As_2}$ flux in GSMBE is obtained by cracking arsine AsH_3 through a high-temperature injector (HTI). Before going through the HTI, the atomic flux is regulated with the help of a mass flow controller. Here, the evolution of the growth rate is linear in function of the AsH_3 flow. Similar to $\mathbf{As_2}$, the phosphorus $\mathbf{P_2}$ flux is obtained by cracking phosphine PH_3 through the HTI.

II.1.C. Temperature measurement and calibration of the substrate

An exact temperature measurement of the substrate is probably the most difficult operation in MBE. The substrate is actually heated by radiation with a filament heater where the temperature is controlled via a thermocouple. However, the thermocouple does not give the exact temperature of the substrate since it's not in direct contact with the material. Hence, in our experiments, we use **optical pyrometry**. Optical IR pyrometry is till now one of the most frequently used techniques for temperature measurements. It's notably important to mention that for an exact pyrometer measurement many critical considerations need to be taken into account: coating of the optical viewport, the band pass of the pyrometer, Mo block temperature, light coming from the effusion cells and the substrate heater, etc… [6,7]. Therefore, our pyrometer is installed in front of the sample in a way that it measures precisely the thermal radiation coming only from the middle of the sample surface (red area in figure II.4).

In figure II.4, we can notice that the grown sample is heated by radiation with the filament heater but being radiantly transparent, high band gap *Eg* semiconductors (like GaP) do not absorb all the heat radiation. The pyrometer measurement is then the one coming directly from the filament itself. To overcome this problem, our samples were soldered to Si templates using Indium. This way the pyrometer will measure the Indium temperature. Actually, the heat

coming from the radiation is absorbed in Silicon templates, in such a way that the sample and Si will have the same temperature.

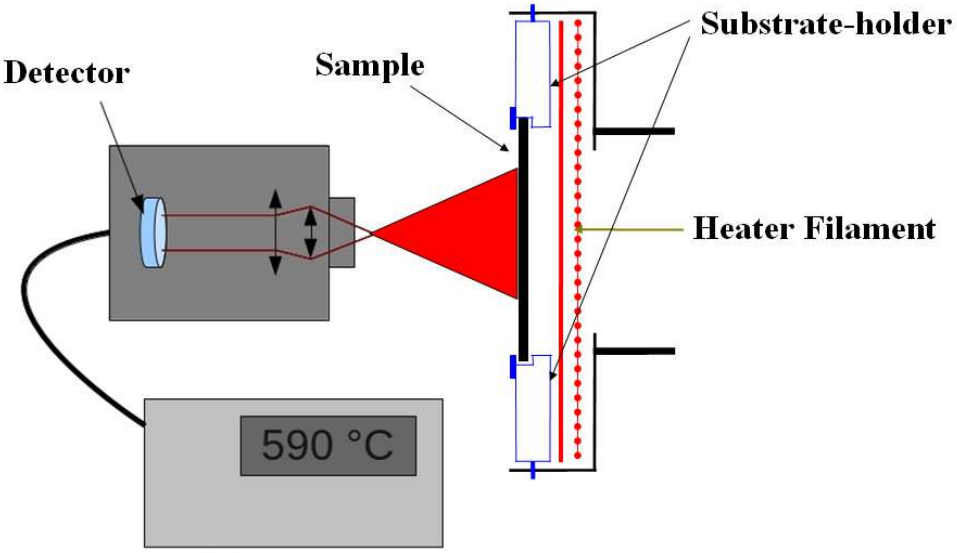

Figure II.4: *Layout of the optical pyrometer equipment.*

The temperature calibration was established using InSb melting point as a reference. A small InSb substrate is soldered on Si and placed on the substrate-holder. The temperature is then increased until a certain point where InSb starts to melt (520 ± 5°C). This observation was done with the help of the RHEED system introduced in the next section.

II.1.D. Reflection high-energy electron diffraction (RHEED)

One of the very useful tools for *in-situ* monitoring of the growth is reflection high-energy electron diffraction (RHEED). It can be used to give feedbacks on surface morphology, determine lattice constant, calibrate the substrate temperature and element growth rate, and observe removal of oxides from the surface.

II.1.D.1. Surface characterization and lattice constant

The RHEED gun emits electrons (15 keV for SSMBE and 35 keV for GSMBE) which strike the surface at a shallow angle (~1°) (see figure II.5). The incoming electrons with a momentum $\mathbf{k}_0$ have a very small incident angle with respect to the sample surface. Therefore, they will only be scattered from the top layer of atoms of the sample. Assuming *elastic scattering*, no energy transfer is allowed from the electrons to the sample. So the scattered

wave vector $\mathbf{k}_{ij}$ lies on the surface of the sphere of constant energy, the so-called *Ewald sphere* (where $|\mathbf{k}_0| = |\mathbf{k}_{ij}|$). In reciprocal space, 3D array turns into spots and the two-dimensional array of the surface atoms turns into vertical lines, the *reciprocal rods*. Wherever these rods cross the Ewald sphere, the condition for constructive interference of the elastically scattered electron beams from the surface is fulfilled. Therefore, these crossing points in **k**-space determine the directions of constructive interference for the electrons in real space. After being reflected, these scattered electron beams hit a fluorescent RHEED screen in certain spots, lying on so-called *Laue circles* which are numbered starting from zero. The figure II.5 shows the Laue circles no. 0 in red and no. 1 in blue.

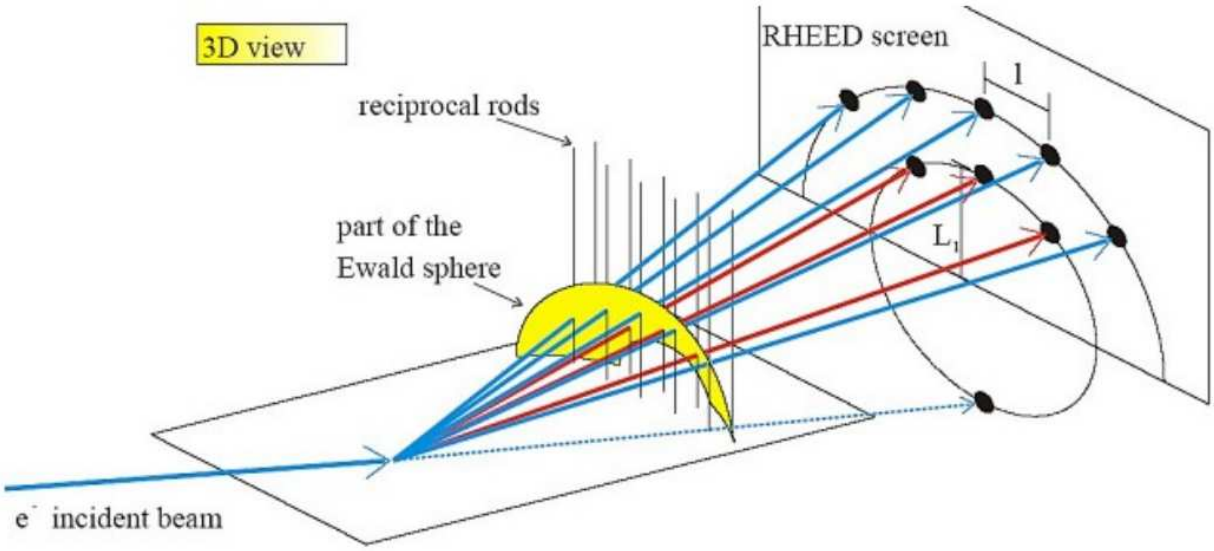

Figure II.5: *Schematic illustration of the in-situ RHEED technique [8].*

A camera monitors the screen and can record instantaneous pictures or measure the intensity of a given pixel as a function of time. Figure II.6 presents examples of RHEED patterns for different types of surfaces.

We use these images to explain the use of this technique to analyze the surface evolution. For example, the RHEED screen exhibits the surface evolution during deoxidization. While increasing the temperature with an arsenic overpressure for GaAs substrates (or phosphorus for GaP substrates), the appearance of a haze is an indication of the amorphous nature of the protective oxide (fig. II.6a). When the deoxidization temperature is reached (610°C for GaAs and 650° for GaP), the RHEED changes to a monocrystalline pattern indicating that the oxide is desorbed from the surface (fig. II.6b). Figures II.6c and II.6d present the RHEED pattern of a 3D mismatched GaSb growth on GaP. Both figures reveal islands formation on mismatched

substrate. However, the appearance of developed streaks in fig. II.6d indicates the formation of {111} facets at the edge of the islands, whereas the well rounded circles in fig. II.6c evidence the absence of any island facets.

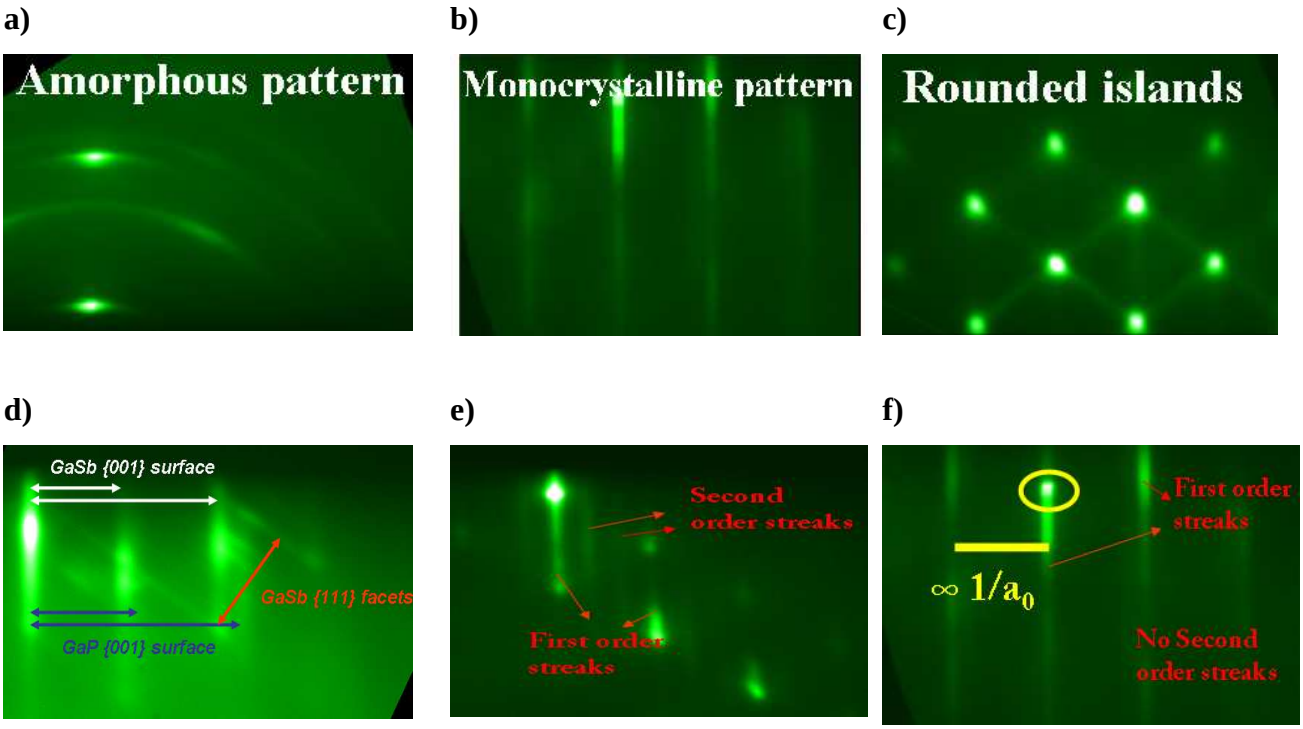

Figure II.6: *RHEED images for different types of surface:* ***a)*** *Amorphous surface,* ***b)*** *Monocrystraline GaAs surface,* ***c)*** *rounded shape GaSb islands on GaP,* ***d)*** *faceted shape GaSb islands on GaP.* ***e)*** *and* ***f)*** *correspond to 2D GaSb surface in both [110] and [1-10] directions, respectively.*

RHEED images of a GaSb surface in both [110] and [1-10] directions are shown in figures II.6e and 6f, respectively. In figure II.6e, in addition to first order streaks which correspond to the lattice constant of the surface, two secondary streaks with a 1/3 spacing of the primary line are seen corresponding to a 'x 3' RHEED pattern in the [110] direction. On the other hand, no secondary streaks are marked in figure II.6f and a 'x 1' RHEED pattern appears in the [1-10] direction. During growth, the RHEED pattern has been recorded. The Specular Beam Intensity (SBI) was hence extracted (yellow circle in fig II.6f) and surface roughness deduced [9]. The strain relaxation can be also determined using the in-plane lattice constant, calculated from the inter-reticular spacing between two first order diffraction streaks (yellow line).

II.1.D.2. Flux calibration

As mentioned before, RHEED SBI oscillations can be used as a measurement of the growth rates in MBE. When a 2D growth is initiated on a smooth surface, the roughness of the surface is function of the coverage θ of the surface, hence the intensity of the specular reflection starts to oscillate between a maximum for (θ=1) and a minimum one (θ=0.5). These RHEED oscillations were first used by Neave et al. [9] where the oscillation frequency corresponds to the monolayer growth rate of the epilayer [10].

Figure II.7 is a schematic illustration of RHEED oscillations. One monolayer corresponds to a complete layer of Ga and As atoms. When a layer starts, the surface is smooth and the specular spot is bright (A); but as the layer nucleates, 2D islands form on the surface and the specular spot intensity decreases (B, C). As the layer is completed (D), the islands coalesce into a flat layer and the specular spot intensity re-increases (E)

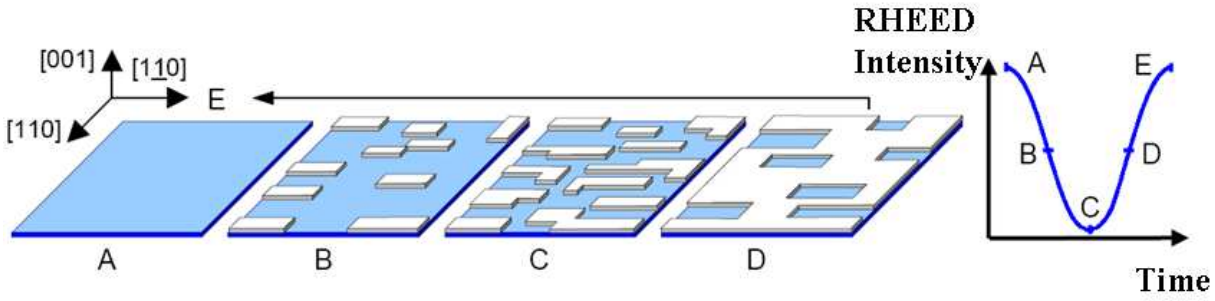

Figure II.7: *Principle of RHEED oscillations [11].*

We are then able to calibrate the Ga and As growth rates on the GaAs substrate. For the Ga calibration, we fix the As flux high enough to maintain RHEED oscillations but also low enough to reduce oscillation damping. The temperature of the Ga effusion cells is changed varying the beam flux and thereby the corresponding frequency of RHEED oscillations. A typical example of the SBI in the RHEED pattern during GaAs growth is shown in figure II.8 (blue line) when Ga crucible is at 950°C. The period of oscillation corresponds exactly to the growth of a single monolayer, i.e. a complete layer of Ga and As atoms in the [001] direction.
Once the Ga growth rate is calibrated, we fix it at 1 ML/s and the As flux is decreased until a certain point where the growth rate starts to decrease below 1ML/s (red line fig. II.8). We can also observe a RHEED pattern transition from a (2x4) As-rich surface to a (4x2) Ga-rich one. These conditions can't be extended since oscillations rapidly disappear as Ga droplets start to form on the surface. Indeed at this point, we are in excess Ga conditions and the GaAs growth

rate depends on the As flux. This method allows us calibrating all group-III and V element growth rates on different substrates (GaAs, InAs and GaSb).

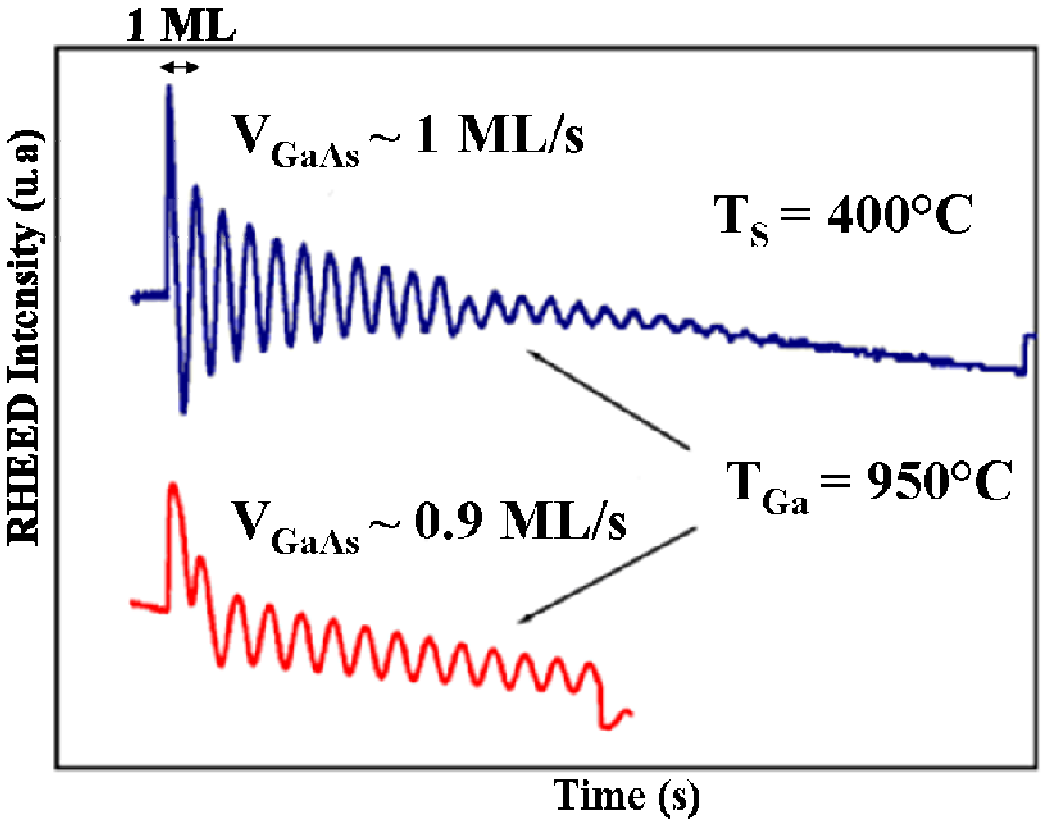

Figure II.8: *RHEED oscillations used for calibration of the growth rate of Ga and As on GaAs [12]. The oscillations are limited by the Ga element when the element V is in excess (blue line), as in the usual growth conditions, or by the arsenic flux when Ga is in excess (red line).In the latter case, we observe that the growth rate is slower (0.9 ML / s) than in the first case (1 ML/s). The growth temperature is 580 ° C. Gallium cell being at the same temperature (950°C) in both cases, we deduce that the lower oscillation corresponds to a growth rate limited by the arsenic flux.*

II.2. Material characterization

II.2.A. Atomic Force Microscopy (AFM)

The sample surface was examined by Atomic force Microscopy (AFM) using a Digital Nanoscope III system, working in the tapping mode. This tool allows us imaging the surface morphology with a resolution that can reach atomic step in the direction perpendicular to the sample surface. It is one of the foremost tools for imaging, measuring, and manipulating matter at the nanoscale. AFM consists of a cantilever with a sharp tip (probe) at its end used to scan

the sample surface (figure II.9). The cantilever is typically made with silicon with a tip radius of curvature on the order of a few nanometers (~10 nm max). When the tip is brought into proximity of a surface, force gradients between the tip and the sample interact with the harmonic oscillator formed by the cantilever. This effect induces both energy dissipation and frequency shift of the oscillator. A digital 3D image is obtained by scanning the surface and reading the Z movement of the vertical feedback position that allows constant interaction. All our AFM images have been further analyzed using both WSxM [13] and Mountains Map [14] softwares.

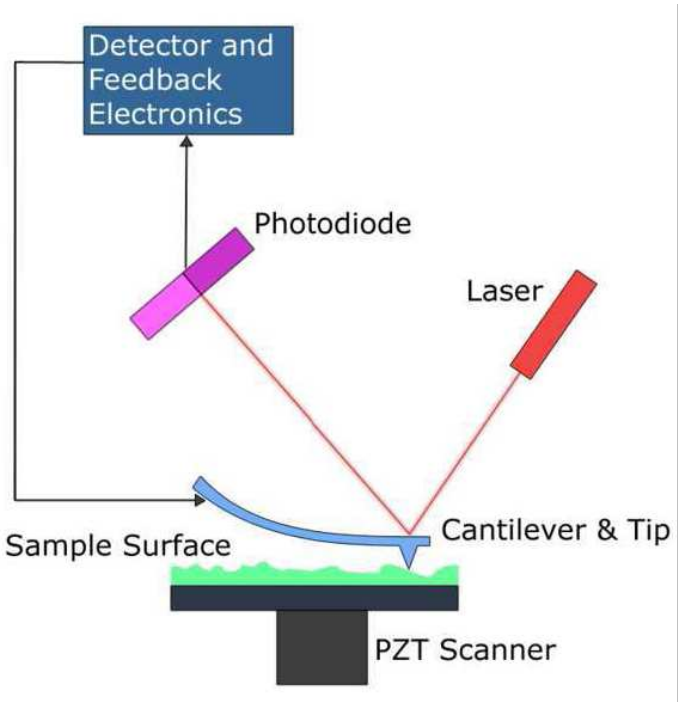

Figure II.9: *Schematic of an atomic force microscope (AFM) [15].*

II.2.B. Transmission Electron Microscope (TEM)

The transmission electron microscope produces images by probing the sample with an electron beam with a very high voltage (40 keV to 400 keV). After being transmitted through the sample, the high energy electron beam provides information about the sample atomic structure. The TEM analyses were performed by Dr. Yi Wang at CIMAP in Caen (France) who pursued his PhD in the frame of the MOS III-V project on the “Misfit dislocation and strain relaxation at large lattice mismatched III-V semiconductor interfaces” [16]. On the other hand,

the samples that were grown on the GaP on Si templates were analyzed by the group of Prof. Kerstin Volz in the Philipps University of Marburg (Germany) [17].

The structural property analyses coming from Caen were carried out on two JEOL microscopes: 2010 LaB6 and 2010 FEG both operated at 200 kV. In $NAsP_{III/V}$, the TEM investigations were done using a Jeol JEM3010 at an acceleration voltage of 300kV. Along with plan-view and cross-section images, double diffraction analysis accompanied with Moiré Fringes experiments were also performed. To determine the atomic type and arrangement of the interface dislocations, the geometrical phase analysis (GPA) of High Resolution TEM (HRTEM) images was applied [18,19] to investigate the local strain distribution which characterizes the dislocation cores. The GPA method relies on the evaluation and interpretation of the geometric phase component Pg(r) by performing a Fourier transform on a HRTEM image. For perfect crystals, the phase of a Bragg-reflection, described by the reciprocal space vector *g*, is constant across the image. However, for a distorted lattice, small deformation can be seen as local lateral shifts of the lattice fringes and consequently as small changes in the phase corresponding to *g*. The phase Pg(r) determined by GPA is related to the displacement field *u* by the expression:

$$P_g(r) = -2g \cdot u(r) \qquad \textbf{(Eq. II.3)}$$

From the local lattice displacements, the two-dimensional strain maps can then be calculated as:

$$\varepsilon_{xx} = \frac{\partial u_x}{\partial x},\ \varepsilon_{yy} = \frac{\partial u_y}{\partial y}, \varepsilon_{xy} = \frac{1}{2}\left(\frac{\partial u_x}{\partial y} + \frac{\partial u_y}{\partial x}\right) \qquad \textbf{(Eq. II.4)}$$

Figure II.10a shows an example of a HRTEM image of a GaSb/GaAs interface and figure II.10b shows the ε_{xx} component of the strain field (deformation along the [001] growth direction) derived from figure II.10a.

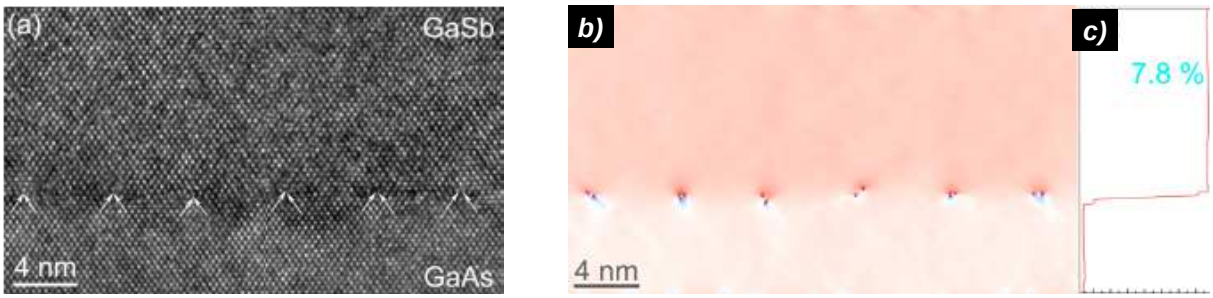

Figure II.10: a) *Cross-sectional HRTEM images of the GaSb on (001) GaAs,* ***b)*** *Strain ε_{xx} components corresponding to the HRTEM image by applying the GPA method [20] and* ***c)*** *Projection of the ε_{xx} images along the interface direction.*

On these images the dislocation cores are easily delineated at the nanometer scale. Projecting the strains on the growth direction allows calculating the average value which can be related to the relaxation state of the layers in figure II.10c. These profiles also provide an idea of the thickness of the highly strain interfacial layer thickness.

Besides the strain distribution, the fine structure of the dislocation core has been analyzed using the method proposed by Kret et al. [21,22] considering the continuum theory of the dislocation. This approach provides a quantitative determination of the Burgers vector of the misfit dislocation and direct insight on their position at the interface. Figure II.11 shows the α_{13} components (where $\alpha_{13} = -\frac{\partial \varepsilon_{xy}}{\partial x} + \frac{\partial \varepsilon_{xx}}{\partial y}$ and $\alpha_{23} = -\frac{\partial \varepsilon_{yy}}{\partial x} + \frac{\partial \varepsilon_{yx}}{\partial y}$) of the tensorial distribution of the dislocation cores derived from the HRTEM image of figure II.10a. In these kinds of images, the dislocation core density tensor takes non-zero values only close to the dislocation core. Integrating the α_{13} over the dislocation core region, we can obtain the in-plane components of the Burgers vector as shown in figure II.11. The detailed processes of all these analyses have been reported in details in Dr. Wang's PhD thesis [16].

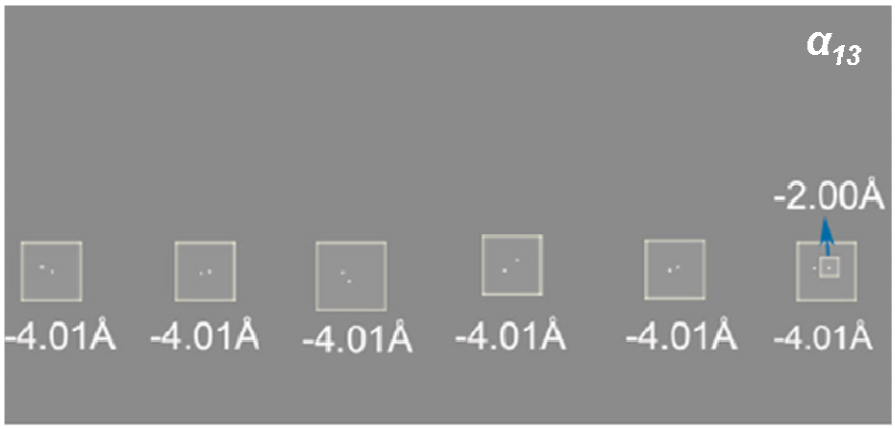

Figure II.11: *The α_{13} component of the dislocation distribution tensor field, the quantified Burgers vectors have been indicated in the images.*

II.2.C. Hall effect measurements

As it's mentioned before, the electron mobility in InAs quantum wells is a very important electronic property in terms of device performance. On the other hand, it is found that many structural aspects influence the transport properties of InAs/AlSb heterostructures like surface and bulk donors, interfacial bonding, anion intermixing, etc… [23]. In addition, some of the samples in this work presented an anisotropic behaviour in terms of transport and

material properties. Therefore, we were interested to determine the electron mobility, the resistivity and the electron density in the InAs channel of the heterostructure. We hence used two of the most commonly used techniques: the Van der Pauw (VdP) measurements for the mean value of electron density and mobility and Hall Bridge measurements to get the electron mobility and density of the InAs channel in both [110] and [1-10] directions.

A HL 5500 PC system is installed at IEMN for these kinds of measurements at room temperature as well as at the temperature of liquid nitrogen (77K). Since a suitable shape specimen is required for this system before any measurement, a photolithography process is needed (figure II.12). In our case, a positive resist (AZ 1512) is first spun onto the sample surface (a). The sample is then exposed to UV light through a chromium mask (b). The development step (MIF 726) then removes the exposed photoresist area (c) not protected by the mask. After chemical etching (H_20 (200ml) /H_2O_2 (1ml) /HF (1ml)) the different mesa are isolated and the remaining photoresist is finally removed (e) with a solvent (Acetone).

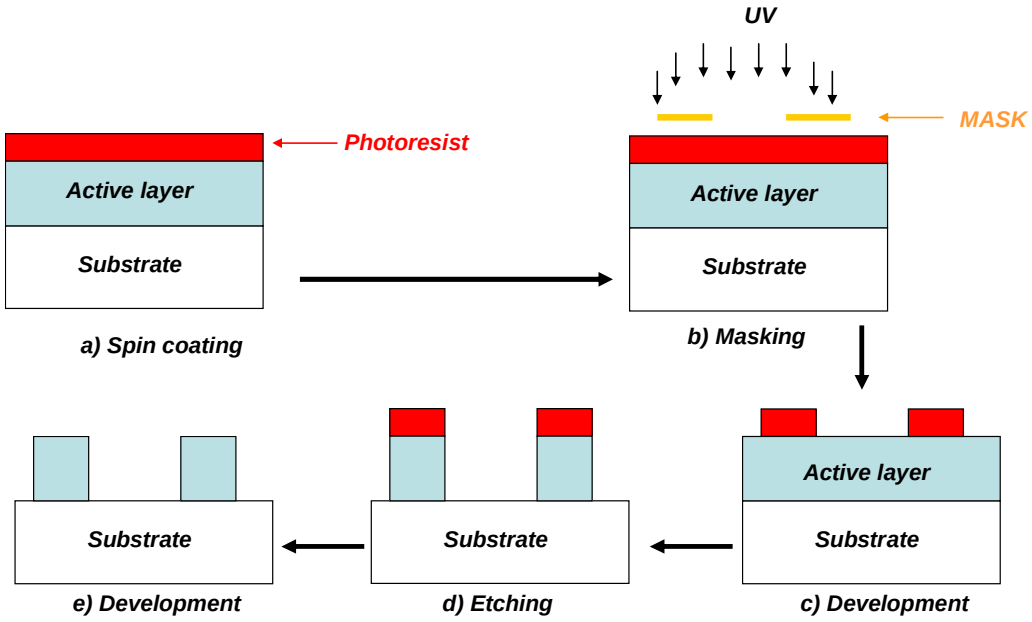

Figure II.12: *Photolitograpy process.*

With the help of an ASTM data sheet and the Clewin Software, we fabricated a new mask that allows us performing Hall measurements for every heterostructure. An example of a prepared sample before measurement is shown in figure II.13a. The corresponding dimensions of the mask are also given. For Ohmic contacts, Indium droplets were placed on the Mesa and the sample was then heated at 200°C leading to indium diffusion in the InAs channel. At last, six probes (or four) are used to contact the Hall bar (or van der Pauw) geometry samples so as to determine Hall Effect with a 0.32 Tesla permanent magnetic field (fig. II.13b).

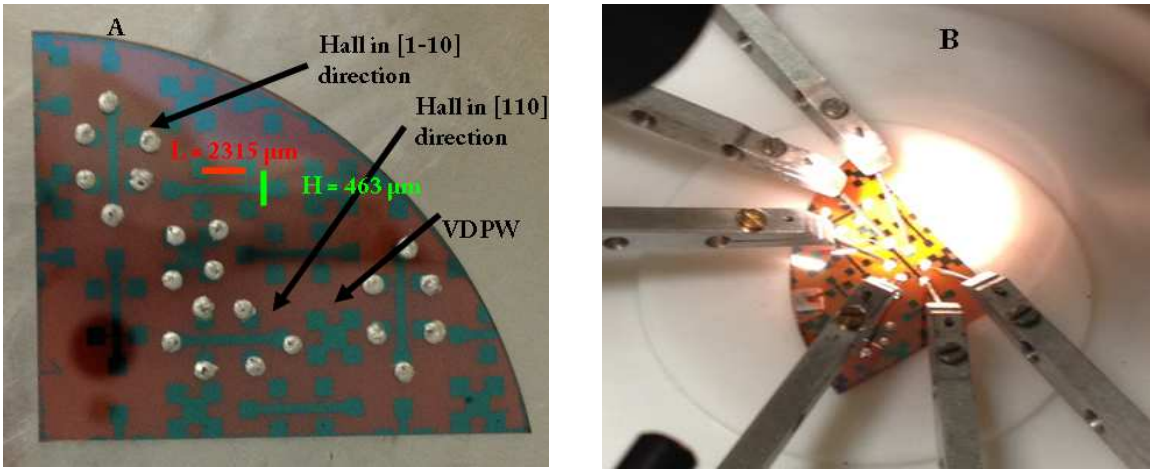

***Figure II.13**: a) AlSb/InAs on GaP after photolithography process and b) HL measurment*

After successive measurements by permuting the contacts, the Hall constant R_H is extracted from the variations of the resistance when applying a magnetic field by the following relationship: R_H (m^3/C) = ΔRxd/(IxB); where ΔR is the resistance variation with the magnetic field, d is the thickness of the layer, B is the magnetic induction and I is the current. The electron mobility is then given by μ(m^2/V.s) = R_H/ρ and n_H (m^{-3}) = 1/(q R_H) where q is 1.6 x 10^{-19} C and ρ is the sample resistivity. Indeed the sign of R_H indicates the type of the charge carriers (n or p).

In this chapter, we have presented the different experimental techniques that were used during this work. In the next chapters, we will give more specific information concerning the growth method of each sample involved in each study. With the aid of the characterization tools (RHEED, AFM, TEM and Hall analysis), we hope to optimize the growth conditions for high quality AlSb/InAs heterostructures on mismatched substrates.

References

[1] G. Gunther, Z. Naturforsh. **13a** (1958) 1081

[2] J.R. Arthur, J. Appl. Phys. **39** (1968) 4032

[3] A.Y. Cho, J. Cryst. Growth **201** (1999) 1

[4] Y. Rouillard, B. Lambert, Y. Toudic, M. Baudet and M. Gauneau, J. Cryst. Growth. 156 (1995) 30

[5] J. Massies, M. Leroux, Y. Martinez, P. Vennegues and S. Laügt, J. Cryst. Growth 160 (1996) 211

[6] B. A. Joyce, Molecular Beam Epitaxy and Heterostructures, edited by L. L. Chang and K. Ploog, NAT

[7] M. Nouaoura, L. Lassabatere, N. Bertru, and J. Bonnet, A. Ismail, J. Vac. Sci. Technol. B **13** (1995) 83

[8] Jürgen Klein, Obtaining the doctoral degree "Epitaxy of doped manganite heterostructures", Faculty of Mathematics and Natural Sciences University of köln (2001)

[9] J. Neave, B. Joyce, P. Dobson, N. Norton, Appl. Phys. A **31** (1983) 1

[10] J. Harris, B. Joyce, P. Dobson, Surf. Sci. **103** (1981) L90

[11] E. Lefebvre, PhD in Material science, « Croissance métamorphique par Epitaxie par Jets Moléculaires et caractérisations physiques pour transistor Bipolaire à Hétérojonction InP/InGaAs sur GaAs », University of Science and Technology- Lille 1, June (2005)

[12] C. Renard, PhD in materials science "Hétérostructures antimoniures/arséniures pour les applications optoélectroniques dans le moyen infrarouge", University of Paris VII, September (2005)

[13] I. Horcas *et al.*, Rev. Sci. Instrum. **78** (2007) 013705

[14] Mountains Map VR Software 6.2 (2011), Digital Surf, see http://www.digitalsurf.fr

[15] www.wikipedia.org

[16] Y. Wang, PhD in condensed matters, materials and devices, « Dislocation et relaxation de contraintes aux interfaces entre semi-conducteurs III-V à large difference de parameter de maille», University of Caen, June (2012)

[17] I. Németh, B. Kunert, W. Stolz, and K. Volz, J. Cryst. Growth 310 (2008) 1595

[18] M. J. Hÿtch, E. Snoek, and R. Kilaas, Ultramicroscopy **74** (1998) 131

[19] S. Kret, P. Ruterana, A. Rosenauer, and D. Gerthsen, Phys. Status Solidi **B 227** (2001) 247

[20] Y. Wang, P. Ruterana, L. Desplanque, S. EI Kazzi and X. Wallart, J. Appl. Phys. **109** (2011) 023509

[21] S. Kret, P. Dluzewski and E. Sobczak J. Phys.: Condens. Mater 12 (2000) 10313

[22] S. Kret, P. Ruterana and G.Nouet, J. Phys.: Condens. Mater 12 (2000) 10249

[23] G. E. Triplett, Obtaining the philosophy doctoral degree, materials and devices, « Process of modeling of InAs/AlSb materials for HEMTs grown by molecular beam epitaxy», Georgia Institute of Technology, January (2004)

CHAPTER III: Nucleation and strain relaxation of GaSb on highly mismatched substrates

We have shown previously that optimizing the growth conditions of the buffer layer is very essential to achieve the best device performance. In this chapter, as a first step, we try to understand the main mechanisms occurring during the nucleation process of the buffer layer growth. More particularly, we investigate by means of RHEED, AFM and TEM analyses the influence of the growth conditions (surface reconstruction, growth temperature, growth rate and V/III ratio) on the nucleation process of GaSb on both GaAs and GaP substrates. We then focus on the influence of these growth conditions on the relaxation and formation of the GaSb epilayer. Finally, we try to draw the main conclusions that can help us to reveal new aspects in the understanding of III-Sb heteroepitaxial growth.

III.1. Surface reconstructions

At the beginning of our work, it is mandatory to explore the nature of the GaAs and GaP surfaces if we consider that GaSb acts differently depending on the initial surface (different dangling bonds, atomic constituents, etc…). The results on the GaSb growth on different reconstructions of GaAs and GaP substrates will help us determining the best surface preparation to start III-Sb growth on highly mismatched substrates.

III.1.A. GaAs surface

III.1.A.1. (001) GaAs considered reconstructions

Since three kinds of atoms enter the game of GaSb growth on GaAs (Ga, As and Sb), three main types of surface are used in the study of the surface reconstruction: As-rich, Ga-rich and Sb-terminated GaAs surfaces. It has been reported that a rich variety of (001) GaAs reconstructions are formed depending on surface stoichiometries, ranging from the most As-rich c(4×4), through (2×4), (6×6) and c(8×2), to the most Ga-rich (4×6) and (4×2) phases [1, 2].

For the As-rich case, the c (4×4) and (2×4) reconstructions shown in figure III.1 are the most commonly observed [3]. The difference between these 2 reconstructions is the As surface

coverage going from 0.75 ML for the (2x4) to 1 ML for the c(4x4)α and reaching 1.75 ML for the c(4x4)β [1].

c(4x4)α(a) and β(b) As-rich GaAs reconstructions (2x4) As-rich GaAs reconstruction

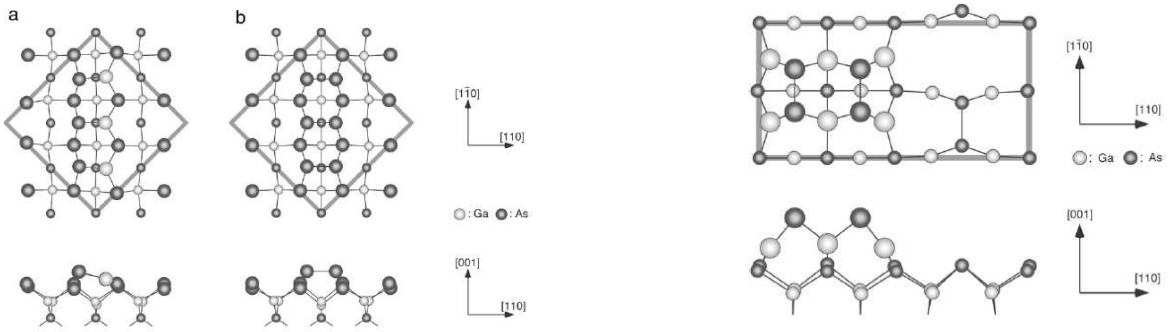

Figure III.1: *As-rich (001) GaAs surface reconstructions [1].*

The (2×4) reconstruction of MBE-grown (001) GaAs is the most stable over a relatively wide range of temperature. During the growth of every GaAs-based sample, the substrate surface needs to be perfectly smooth before any heteroepitaxial growth. Therefore, after deoxidization at ~600°C, 3000 Å of GaAs is grown on the substrate at 580°C with a Ga growth rate of 1 ML/s and a V/III ratio of ~ 6 (figure III.2).

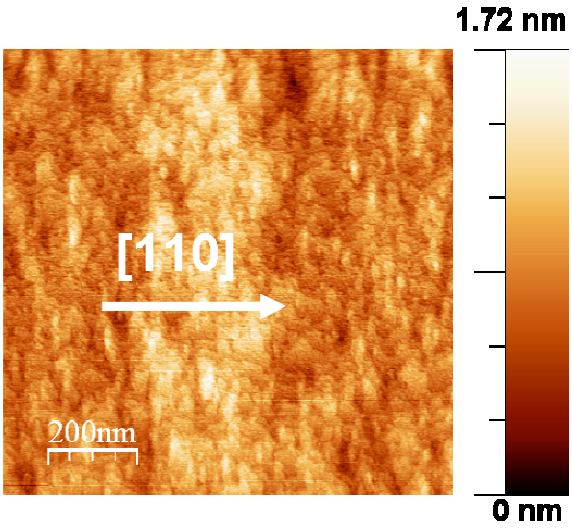

Figure III.2*: (1x1) µm^2 AFM image of MBE growth of GaAs/GaAs with a RMS value equal to 0.2 nm.*

Ga-rich reconstructions are usually obtained by heating the As-rich reconstructions without As flux. Although a rich variety of reconstructions, such as the (3×1), (1×6), (2×6), (3×6), (6×6), (4×6), (4×2), and c(8×2), has been reported, only the atomic structures of the (4x6) and (4x2) reconstructions are well understood [1]. It is important to mention that two kinds of (4x6)

Ga-rich surfaces need to be distinguished: the *so-called* (4x6) which is less Ga-rich compared to the (4x2) phase and the *real* (4x6) phase which is more Ga-rich than the (4x2) one [4]. During our experiments, two methods are used to obtain a Ga-rich surface represented in figure III.3.

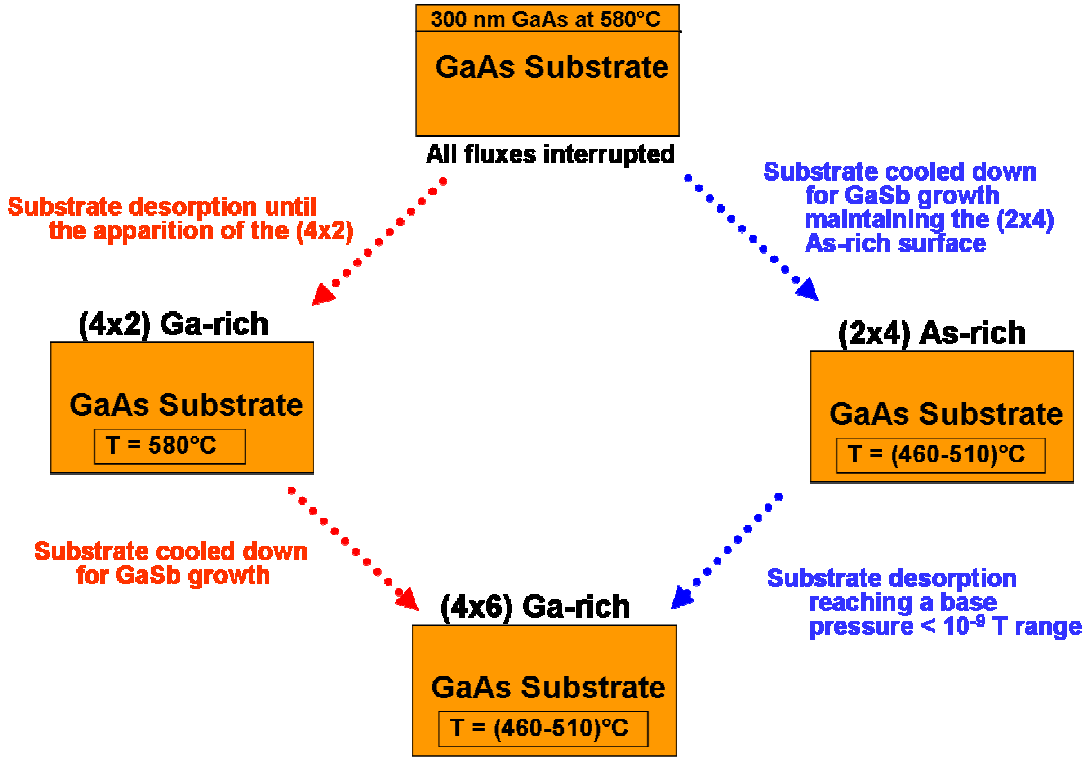

Figure III.3: *Schematic illustration of the 2 methods (red and blue) used to obtain a Ga-rich surface.*

In the first one (red in fig. III.3), the As valve and Ga shutter are closed after homoepitaxial GaAs growth at 580°C. At this temperature, As is progressively desorbed from the surface and as the As partial pressure progressively decreases in the chamber, the RHEED pattern turns to a (4x1) and then to a (4x2) surface reconstruction characteristic of a Ga-rich surface. By decreasing the temperature for GaSb growth (460°- 510°C), the RHEED pattern exhibits a (4x6) reconstruction at 550°C approximately.

The second method (blue in fig. III.3) consists in decreasing the sample temperature just after GaAs homoepitaxy (always without any flux exposure). This allows keeping the (2x4) As-rich surface. However, once the desired temperature is reached and the sample is left for an excess As desorption reaching a base pressure < 10^{-9} T range, the (4×6) reconstruction appears indicating a Ga-rich surface.

The two methods clearly show us that the (4x2) is not stable at temperatures lower than 560°C (also observed in ref 1-2). Moreover, since less As is desorbed at 460-510°C compared to 580°C, the RHEED in this range actually exhibits the *so-called* (4x6) reconstruction which is less Ga-rich compared to the (4x2) reconstruction. Hence, an additional method which consists on sending 1 ML of Ga on the (4x6) reconstruction was also used. This way we are sure that before starting GaSb growth, the top layer of the GaAs surface consists of Ga atoms.

For the Sb-terminated (001) GaAs reconstructions, 4 main reconstructions are often identified: (1x4), (1x3), (2x4) and (2x8) [5]. Moriarty et al. [6] claimed that following Sb deposition on a GaAs suface at low temperatures, a (1x4) phase is observed during annealing in the 200-360°C range; a (1x3) then appears at 360°C. In the 450–560 °C range where Sb starts to evaporate from the surface, a (2x4) Sb-rich reconstruction is present. The (2x8) reconstruction is also observed on GaAs surface when Sb is exposed at normal growth temperatures (i.e. 450°-560°C) [5].

The (2x4) and (2x8) Sb-terminated surfaces are illustrated on figure III.4. The Sb coverage for the (2x4) Sb-rich surface is approximately 0.5 ML/s where both As and Sb dimers are found at the GaAs surface. On the other hand, the (2x8) consists of Sb dimers in three atomic layers, and an Sb coverage larger than 1 ML [7].

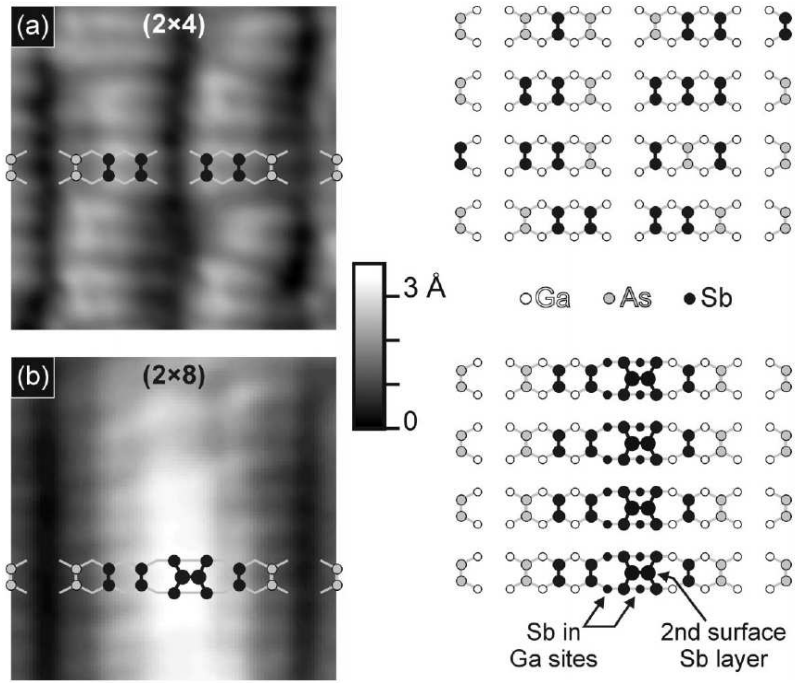

***Figure III.4**: (a) (2×4) and (b) (2×8) reconstructions consistent with both the STM images and Sb coverages. Horizontal direction is [110]. [5]*

To achieve an Sb-rich reconstruction surface on our samples, either Ga-rich or As-rich surfaces are exposed to an Sb flux. An example of the GaAs surface evolution at 480°C in function of Sb exposure time for an Sb flux of 2.5 ML/s is given on figure III.5.

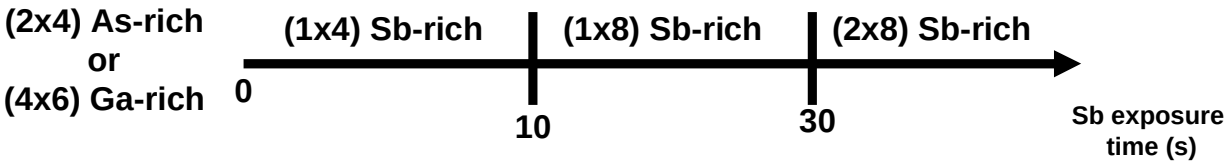

Figure III.5: *RHEED evolution of GaAs surface at 480°C in function of the Sb time exposure for an Sb flux of 2.5 ML/s. If Sb is interrupted at any time the RHEED exhibits a (2x4) Sb-rich GaAs reconstruction.*

Once Sb is sent on the surface, the GaAs reconstruction changes to a (1x4) phase for the both types of surfaces. Then a (1x8) reconstruction appears at 10 s and after 30 s of Sb deposition the surface changes to the most Sb-rich (2x8) reconstruction. Now if Sb flux is interrupted at any time and the sample maintained for desorption, the (2x4) Sb-rich is the present reconstruction. Indeed at very high temperatures (> 580°C) the desorption can lead to a complete evaporation of As and Sb on the surface and a (4x2) Ga-rich surface is present (see also [6]). We note that the observed (1x4) transition phase is not the same as that reported by Moriarty et al. at low temperatures [6]. In our case, this transition phase is probably the (2x4) Sb-rich surface with an unclear x2 in the [1-10] direction. This can be confirmed by the fact that the (2x4) Sb-rich is quickly observed if the Sb flux is interrupted. At last, we should also note that the transition time from one phase to another can vary depending on the used Sb flux and substrate temperature but the surface evolution remains the same.

III.1.A.2. Influence of GaAs reconstruction on GaSb growth

Five samples A, B, C, D and E presented on figure III.6 are used for this study. For all the samples the Ga growth rate is 0.7 ML/s with a V/III ratio equal to 3. For samples A and B, once GaAs smoothing is complete, the substrate is cooled down to 480°C under low As_4 flux. Once the targeted temperature is reached, As is interrupted until the RHEED still maintains the (2x4) As-rich reconstruction. At this time, either the 10 MLs GaSb are deposited opening simultaneously the Ga and Sb shutter (sample A), or the Sb valve is opened and the surface is exposed to Sb_2 for 5 s changing the RHEED pattern to a (1x4) surface reconstruction before the 10 MLs GaSb deposition (sample B). For samples C, D and E the As valve is closed to have a (4x2) Ga-rich surface after GaAs homoepitaxial growth at 580°C (see section II.1.A.1

Ga-rich). The surface is then exposed for 5 s to an antimony flux at 580°C just after the (4x2) reconstruction, changing the surface reconstruction to an Sb-rich (2x4) pattern once the Sb flux is interrupted. The temperature is then decreased at 480°C. At this time, the 10 MLs GaSb are deposited opening simultaneously the Ga and Sb shutters for sample C.

A	B	C	D	E
10 MLs GaSb	10 MLs GaSb	10 MLs GaSb	10 MLs GaSb	10 MLs GaSb
(2x4) As-rich	(1x4) Sb-rich	(2x4) Sb-rich	(1x8) Sb-rich	(2x8) Sb-rich

Figure III.6: *Schematic diagrams of the lay out of the five investigated samples.*

For samples D and E, before the 10 MLs GaSb deposition, the Sb valve is opened and the surface is exposed to Sb_2 for 5 s for sample D and 2 min for sample E changing the RHEED pattern to a (1x8) and (2x8) surface reconstruction, respectively. After a spotty RHEED pattern sequence, a (1x3) surface reconstruction rapidly appears during GaSb deposition.

The evolutions of the in-plane lattice constant (IPLC) and of the specular beam intensity (SBI) extracted from the RHEED pattern records are displayed in figure III.7.

We can notice that the strain relaxation of GaSb coincides with the drop off of the SBI, reaching a final value near the GaSb lattice constant (6.0959 Å). The drop off of the SBI is due to the appearance of a spotty RHEED pattern characteristic of a three dimensional island growth mode. However, by looking more deeply, some oscillations appear on the SBI when GaSb growth begins. These oscillations are evidence of the formation of a GaSb wetting layer (WL) on the GaAs surface at the first stages of growth [8]. We have estimated the thickness of the WL for the different surface preparations going from 1.6 ML for sample A till its disappearance for sample E (fig. III.7f).

The (1x1) μm^2 AFM images of each sample are shown in figure III.8. All the images exhibit islands elongated in the [110] direction with mean heights increasing from approximately 4.6 nm for sample A up to 6.3 nm for sample E. The graph in figure III.8 also illustrates the WL thickness and the mean island height of each sample. The red arrow is a reminder that Sb initial surface coverage increases from sample A to sample E. The value of the mean height is correlated with the WL one: when a thinner WL is formed, higher GaSb islands are present.

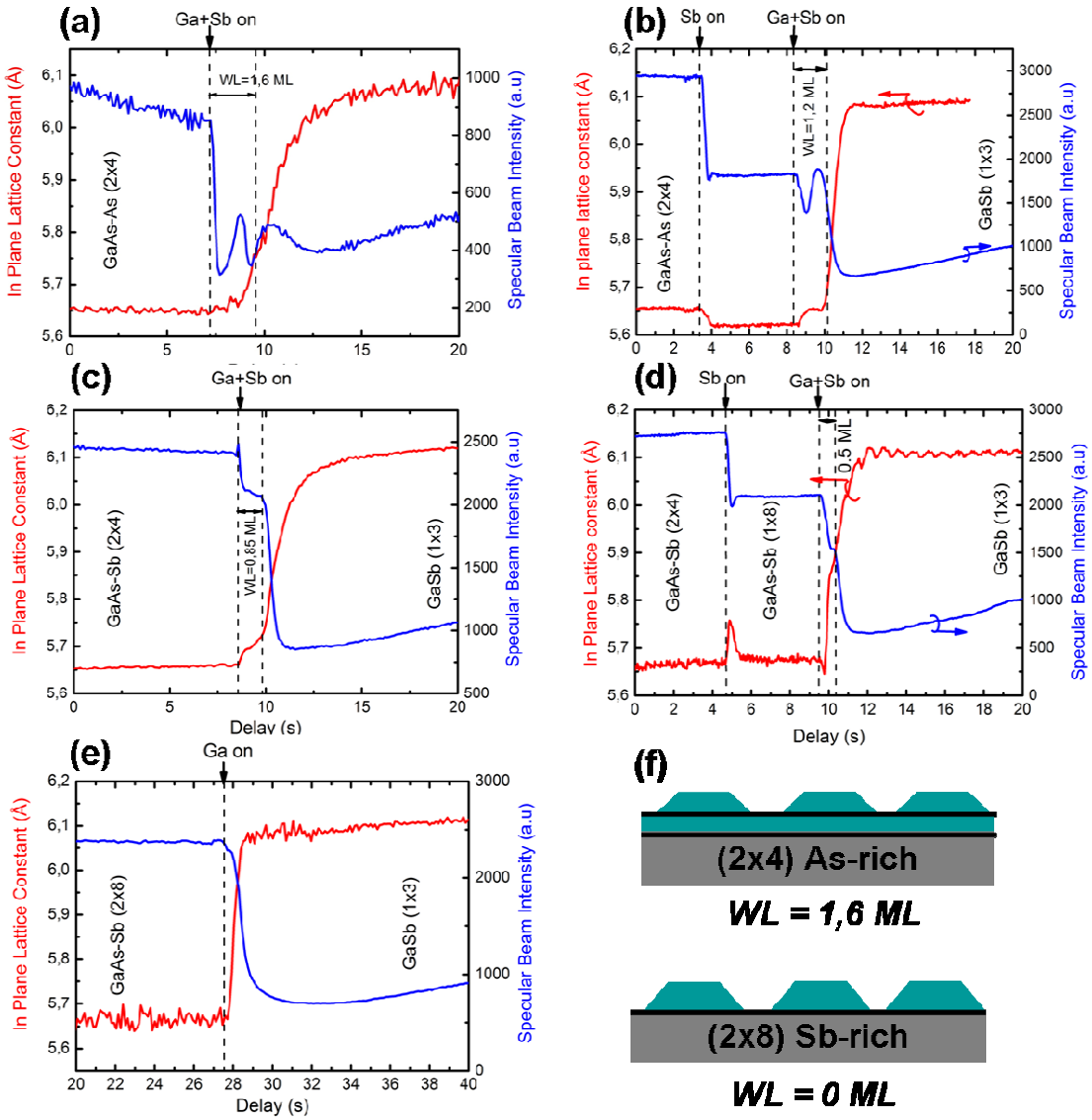

Figure III. 7: *IPLC and SBI evolutions extracted from the RHEED pattern records of samples A (a), B (b), C (c), D (d) and E (e). (f) is a schematic illustration emphasing the difference in GaSb island formation between samples A and E.*

Comparing the first two samples, we notice that the thickness of the wetting layer decreases by sending Sb on the GaAs surface. The WL thickness is further decreased in sample C. We remind that the As desorption at 580°C in sample C is much higher than at 480°C in samples A and B. Obviously, the As desorption reduces both Sb/As intermixing and the WL thickness. This can be also confirmed by increasing Sb coverage on the GaAs surface in samples D and E. The WL thickness further decreases in sample D and can be suppressed using a (2x8) surface reconstruction (sample E).

These results indicate that the thickness of the GaSb wetting layer on the GaAs surface is strongly affected by the initial surface reconstruction and can be suppressed using a (2x8) Sb

terminated GaAs surface reconstruction. The formation of a WL at the interface is an evidence of a S-K growth mode of GaSb on GaAs. On the other hand, the suppression of the WL with the (2x8) Sb-rich surface case leads to GaSb growth in a VW mode.

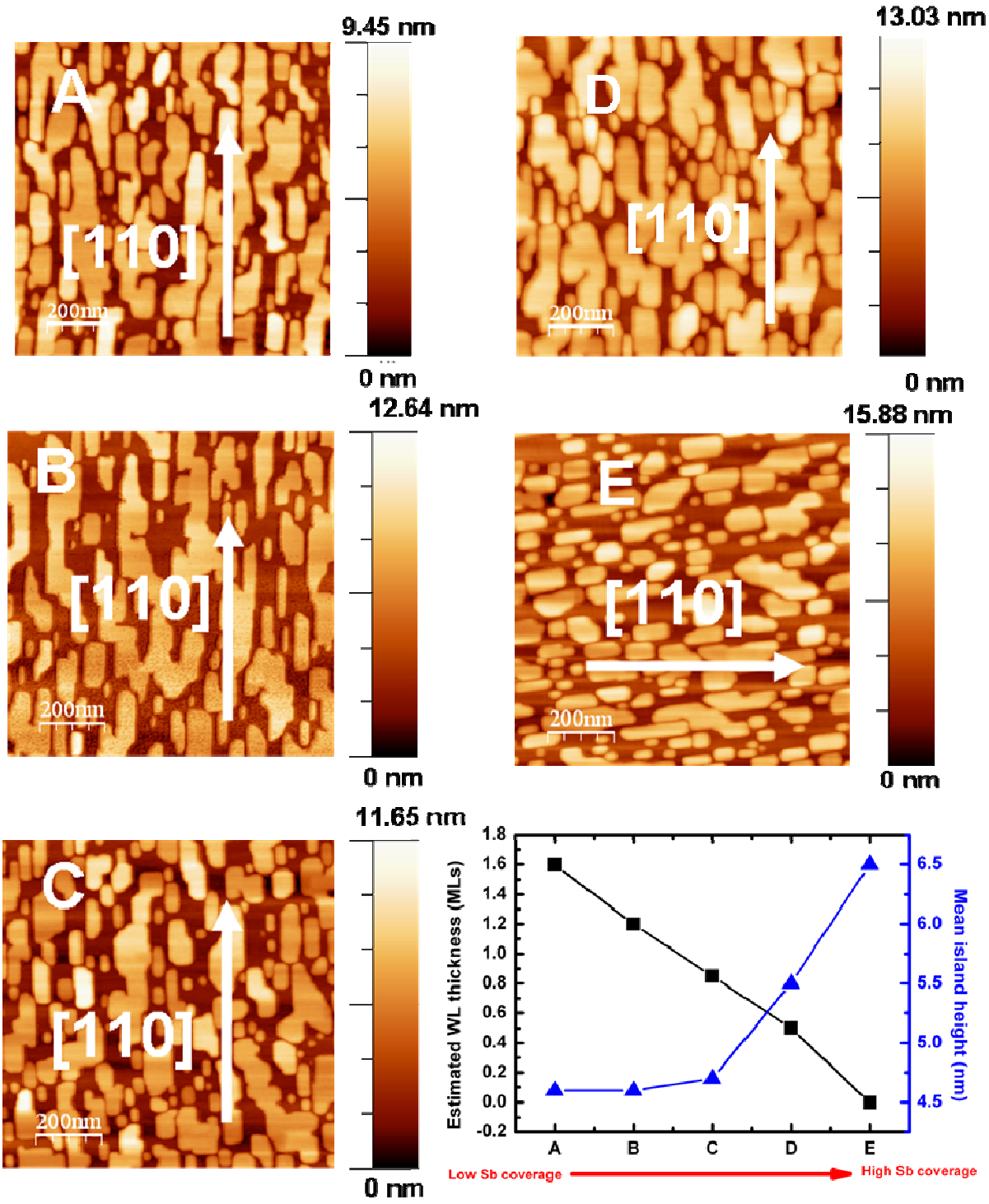

Figure III.8: *The (1x1) μm^2 AFM images of samples A, B, C, D and E. The graph corresponds to the WL thickness calculated from RHEED analysis of figure III.6, and the mean island height from the AFM images.*

Figure III.9 displays the AFM images of 2 new samples A' and E' for which only 3 MLs of GaSb have been deposited in the same conditions as for samples A and E respectively. We notice that sample A' exhibits smaller islands compared to sample E', with roughly the same density (around $4x10^{10}/cm^2$). This is consistent with the different growth modes for these 2 samples (S-K for sample A', V-W for sample E'), resulting in a lower material volume in islands for sample A'.

Since Sb coverage is larger in the (2x8) Sb-rich reconstruction surface, the above results show that increasing the Sb coverage on the initial surface increases the Ga diffusion length. This is confirmed by the difference in island surface coverage between sample A (68%) and E (55%) after 10 ML GaSb deposition.

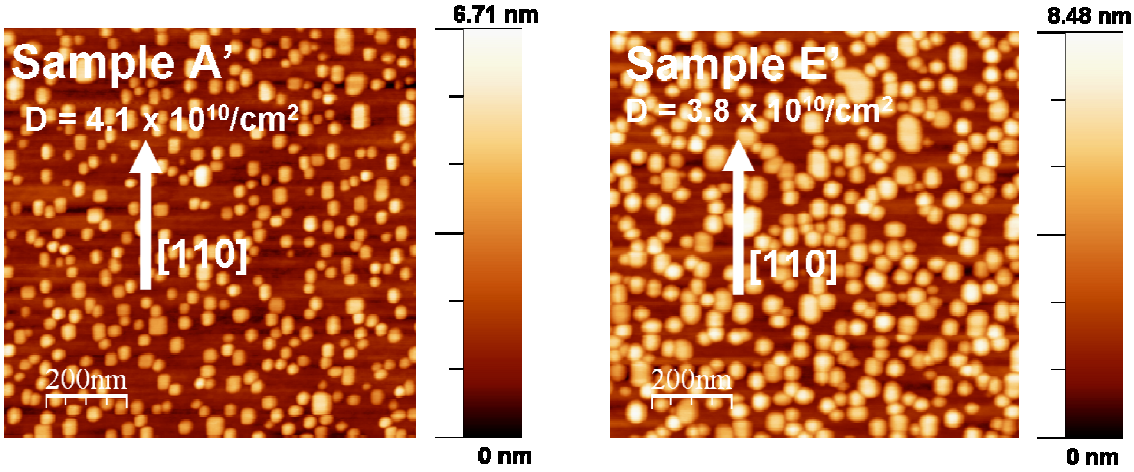

***Figure III.9**: (1x1) µm² AFM images of samples A' and E' after only 3 MLs of GaSb growth. D corresponds to the island density of each sample.*

To study the influence of the surface reconstruction on GaSb relaxation, cross-sections TEM images of samples A and E are depicted in figure III.10. From these cross-sections, we can estimate the mean distance between MDs (d_{mean} in the figure). We can observe a regular array of 90° MDs at the interface for both samples with nearly the same d_{mean}. These 90° MDs are underlined by the geometrical phase analysis (GPA) of the cross sections that reveals the local atomic displacements across the interface. Contrary to the analysis of the TEM images, the strain relaxation calculated from the GPA exhibits different values in each sample. The island in sample E is more relaxed than the one in sample A. To have a statistical estimation of these values in our study, the same measurement was performed on more than ten islands of all the samples in both [110] and [1-10] directions. However, these analyses did not give any precise

conclusion and no overall consistency is found according to the different surface reconstructions involved. Furthermore, due to island size and shape distribution, the error bar is too large to get a clear conclusion. Obviously, the used TEM analyses have not allowed evaluating the influence of the surface reconstruction on the strain relaxation of GaSb islands.

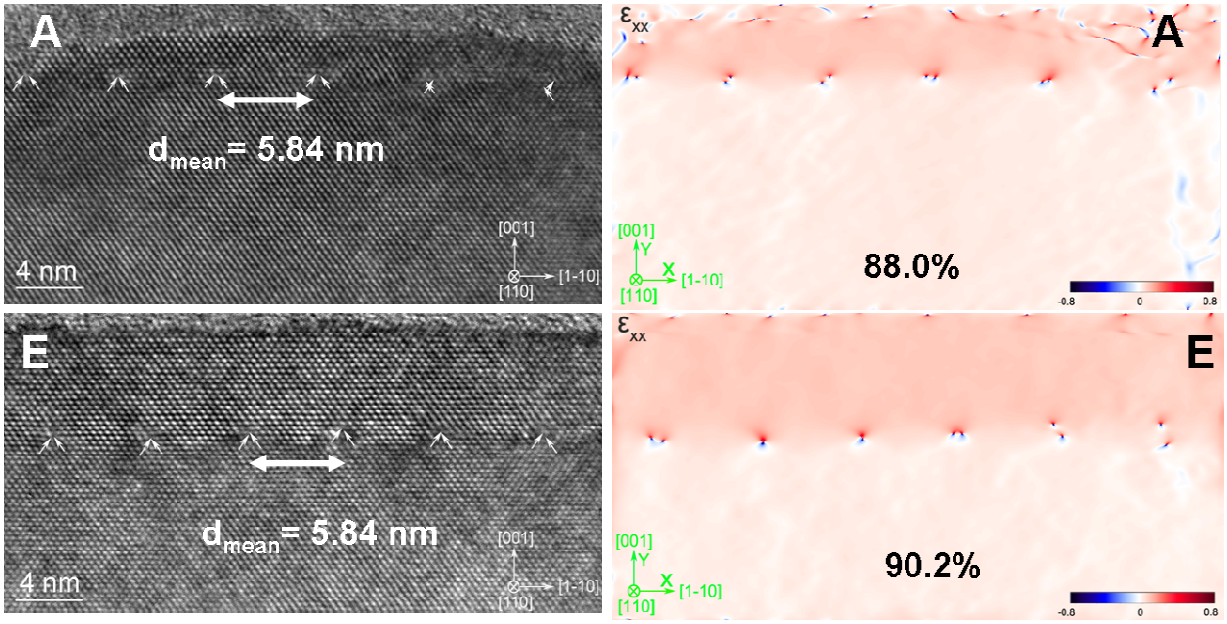

Figure III.10: *Cross-sectional TEM images along the [110] direction of sample A and E and their corresponding GPA*

Two other samples F and G are used to compare the growth of 600 nm of GaSb on a Ga and Sb-rich surfaces, respectively. For sample F, after GaAs homoepitaxy the sample temperature was decreased at 510°C without any flux and once the desired temperature is reached, the sample was maintained for As desorption until the (4x6) Ga-rich reconstruction appears (see section III.1.A.1). Then, 1 Ga ML was deposited before the growth of GaSb. For sample G, the Sb shutter was opened and the As valve was closed after GaAs homoepitaxy. The sample temperature was also decreased at 510°C exhibiting a (2x8) surface reconstruction and once the desired temperature is reached GaSb growth begins. For both samples, the RHEED pattern exhibits a 3D transition when GaSb growth starts at 510°C, but after a few nanometers, we recover a 2D RHEED pattern with a (1x3) surface reconstruction. Figure III.11 exhibits TEM analysis of these two samples and the GPA of the HRTEM images. The averaged densities of threading dislocations estimated from the plan-view TEM images are 7.5×10^8 and 2.2×10^8 TDs/cm^2 for samples F and G, respectively. From the cross-section images of the second and third rows, more 60° MDs can be seen with a Ga-rich surface compared to the Sb-rich surface.

Depending on several images, the mean spacing between the misfit dislocations is determined to be 5.67 nm and 5.46 nm for samples F and G, respectively. Evidently, the average distance of the interface dislocations in sample G almost coincides with the theoretical value (5.51 nm) for GaSb/GaAs interface, indicating a higher strain relaxation state in the epitaxial layer.

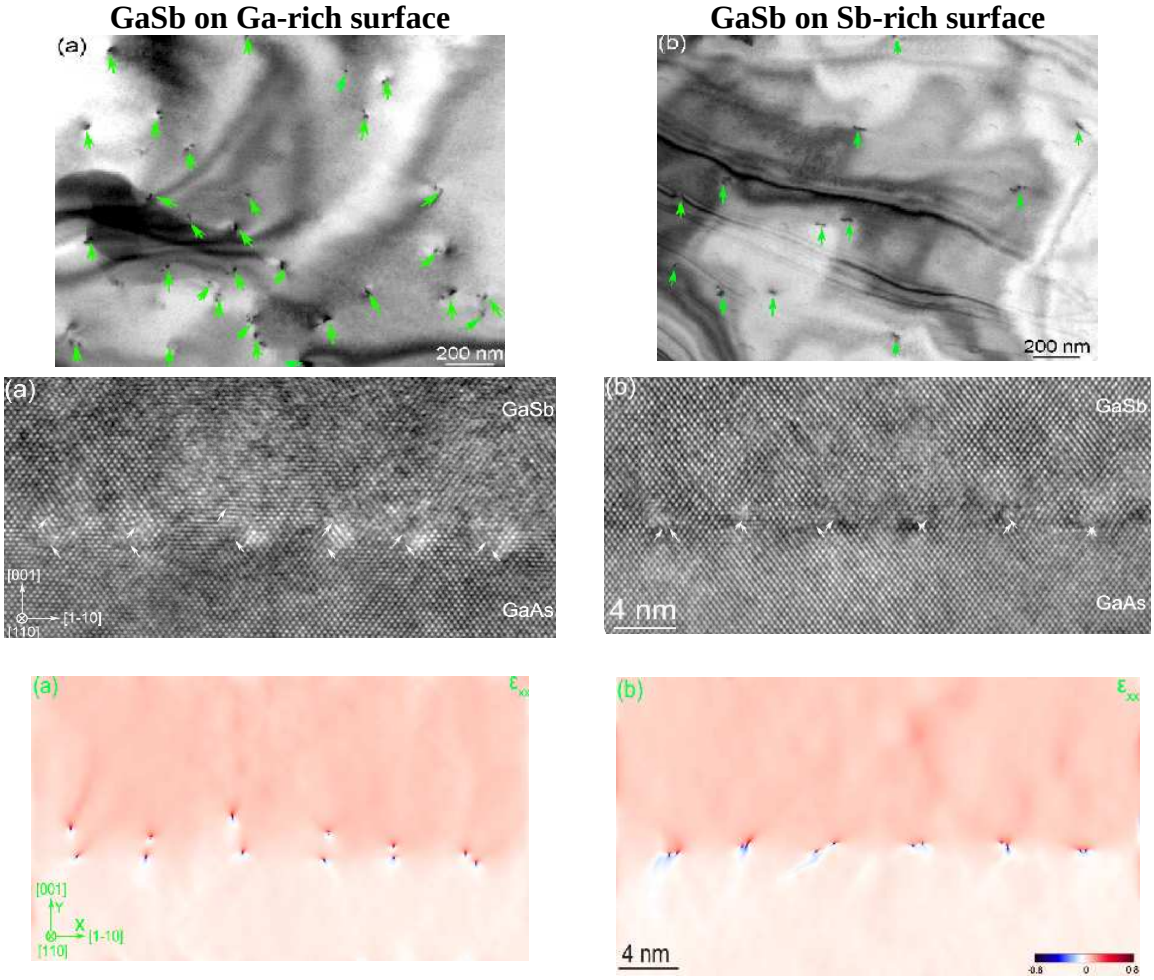

Figure III.11: *TEM analysis of samples F (a) and G (b). In the first row, TDs appear as dark dots on the density background, they are marked by arrows. In the second row, the positions of the interface dislocations have been marked by the additional {111} lattice planes (inclined arrows). Strain ε_{xx} components corresponding to the second row cross-section images are presented in the third row [9].*

Figure III.12 presents the projection of the ε_{xx} component (x axis along the [1-10]) derived from the cross-sectional images. The value of ε_{xx} in sample G is larger than in sample F. Moreover, the abrupt change in the intensity at the interface region reveals that the thickness of the dislocation cores region is 2.93 nm and 0.95 nm for sample F and G, respectively. This

decrease in the thickness of the dislocation core region indicates a sharp interface between the GaSb epitaxial layer and GaAs substrate with an Sb-rich surface treatment.

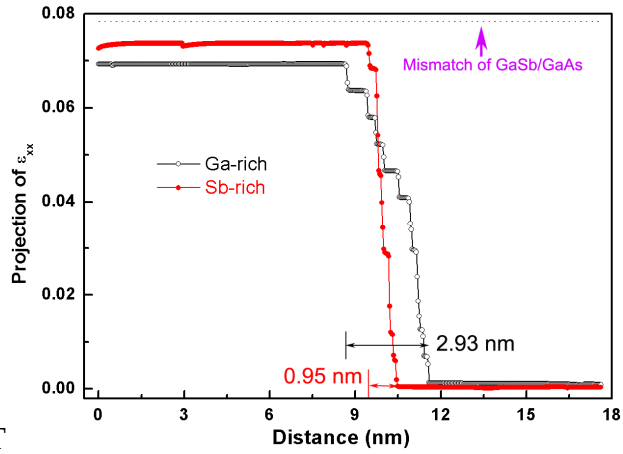

T

Figure III.12: *The corresponding projection of the ε_{xx} images on the growth direction, the vertical part of each curve shows the interfacial layer thickness and the max height corresponds to the relaxation level [9].*

The GaSb epitaxial layer grown on GaAs substrate subsequent to a Sb-rich surface treatment exhibits a lower TD density and a better strain relaxation than on a Ga-rich surface. The HRTEM and GPA analysis have shown that a (001) Sb-rich surface promotes the formation of 90° MDs which are more efficient for strain island relaxation.

III.1.B. GaP surface

III.1.B.1. Observed reconstructions

Even if much progress has been made in understanding the microscopic structure of the growth planes of III-V compound semiconductors, only few studies were reported on GaP. Based on the simple concept of covalent radii, (001) GaP (1.19) surface structures can be expected to deviate from the ones observed for GaAs (1.05) [10]. Till now all observations performed on surfaces prepared either by MBE [11,12] or metalorganic vapor-phase epitaxy [13,14] reveal three main reconstructions with decreasing phosphorus coverage: a (2x2) then a (2x1) and finally a (2x4) one. The evolution of the surface reconstruction versus the annealing temperature for a (001) GaP sample with and without phosphorus flux given by Wallart et al. [15] is shown on figure III.13. An interesting feature is the existence of a Ga-rich (2x4) reconstruction which has no counterpart in the arsenides for which cation-rich surfaces exhibit

a (4x2) reconstruction. During our experiments, the same evolution is observed. Furthermore, at approximately 615°C an additional (4x4) reconstruction is present during annealing without phosphorus flux and remains until the surface degradation for temperatures > 700°C. Even if the sample temperature is decreased without any flux (to nearly 440°C), the (4x4) resists. However, if P flux is exposed to the surface at any time, RHEED pattern changes rapidly to a (2x4) reconstruction.

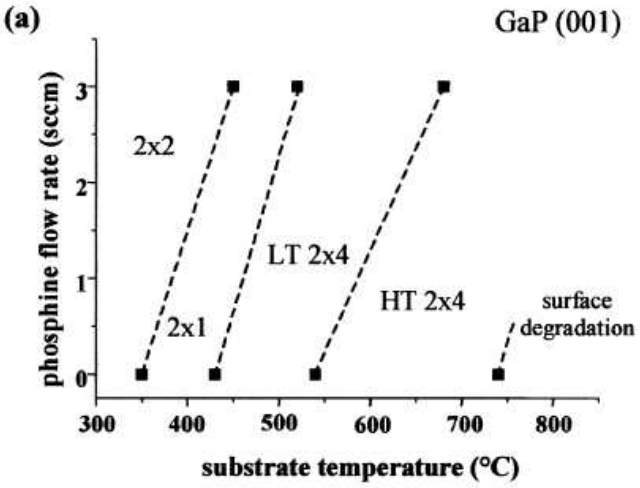

Figure III.13: *Evolution of the surface reconstruction versus the annealing temperature for (0 0 1) GaP with and without phosphorus flux [15].*

Our observations agree with the (4x4) reconstructed surface previously observed by Yoshikawa et al [16]. They defined this reconstruction as a Ga-rich surface with the formation of Ga droplets on a (2x4) reconstructed surface for high amounts of Ga supply.

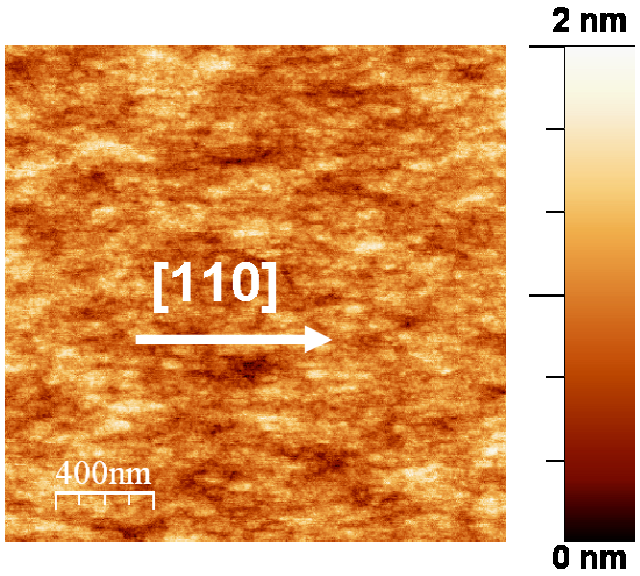

Figure III.14: *AFM images of a 450 nm thick GaP layer grown at 630°C on a (001) GaP substrate.*

As for the GaAs substrates, we were interested in smoothing the GaP substrates at the beginning of any growth. The substrate is first annealed under P flux in the 700° C range. 450 nm of GaP is then grown at 630°C with a growth rate of 1 ML/s exhibiting a sharp (2x4) RHEED pattern. The (2x2) μm^2 AFM image of the GaP homoepitaxial growth is shown in figure III.14. RMS roughness calculated from the images is 0.24 nm exhibiting a good quality and smooth surface.

III.1.B.2. Influence of the surface reconstruction

To our awareness, no report exists on the reconstructed Sb-terminated GaP surface. We therefore decided to use the knowledge we have obtained with GaAs substrates and apply it for the growth of GaSb on GaP substrates. Two samples (I and J) are first grown to study the influence of the GaP surface treatment on the relaxation of 10 MLs GaSb. Figure III.15 is a schematic illustration of 10 GaSb ML growth on an Sb-rich (sample I) and a Ga-rich (sample J) surfaces.

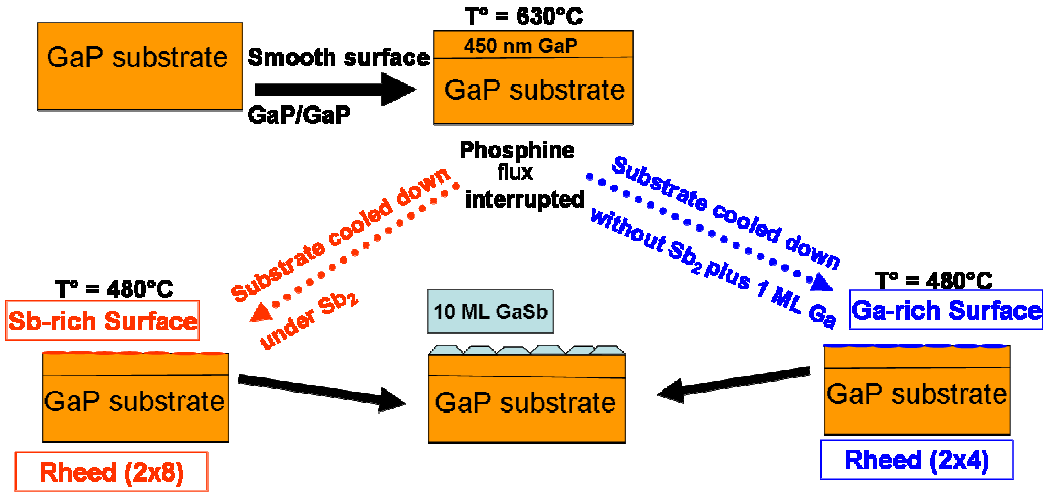

Figure III.15: *Schematic illustration of 10 GaSb ML growth on an Sb-rich (sample I) and a Ga-rich (sample J) surface.*

For sample I, after the interruption of the phosphine flux, the substrate is cooled down to 480°C under Sb_2. The RHEED pattern exhibits a x2 reconstruction in the [1-10] azimuth, whereas a x8 reconstruction is observed in the [110] one. Then the Ga shutter is opened and 10 GaSb MLs are deposited. For sample J, the substrate is cooled down from 610 to 480 °C without any flux, keeping a (2x4) surface reconstruction, and then 1 Ga ML is deposited before the opening of the Sb valve with a subsequent growth of 9 GaSb ML without any interruption.

For both samples, once the GaSb growth begins, the RHEED pattern turns rapidly from a two-dimensional to a 3D one, characteristic of a Volmer–Weber growth mode. After few monolayers, a (1x3) surface reconstruction, characteristic of the (001) GaSb surface, starts to appear.

After deposition of 10 GaSb MLs, the AFM images (fig. III.16) recorded on both samples reveal roughly the same surface morphology, i.e. an island density around 1.8 x 10^{10}/cm^2 and a mean island height of 3.2 (± 0.2) nm.

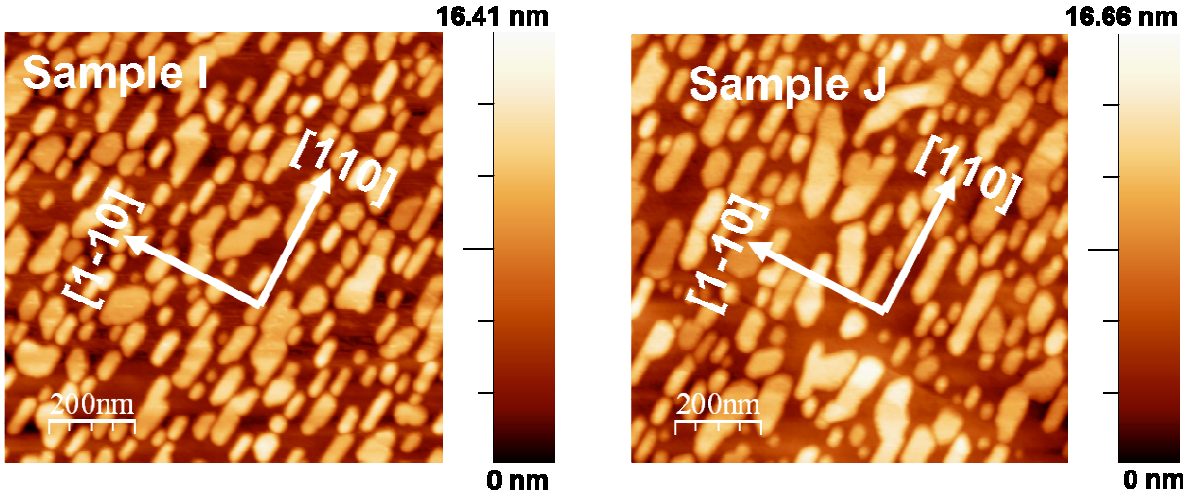

Figure III.16: *(1x1) µm^2 AFM images of samples I and J.*

The IPLC evolution during the first 3 MLs of the GaSb growth and cross-sectional high resolution TEM (HR-TEM) images of samples I and J are presented on figure III.17. For both samples, a quick change from the GaP lattice constant (5.4505 Å) to a value close to that of GaSb (6.095 Å) occurs during the first ML. However, this relaxation is faster for sample I (about 0.7 ML) than for sample J (about 1.6 ML) and the lattice constant after 3 MLs is a bit larger for sample I than for sample J (about 6.1 Å versus 6.05 Å). This suggests a better relaxation for sample I than for sample J. Differences between samples I and J are highlighted more precisely by the HR-TEM images. The interfaces between GaSb and GaP are underlined by MDs, as indicated by the white arrows which mark the termination of the additional {111} lattice planes in the GaP substrate. In these images recorded along the [1-10] zone axis, the core position of 60° and 90° MDs is marked by the termination of one and two additional {111} half lattice planes, respectively. Therefore, sample I shows a regular periodic array of 90° MDs confined at the interface. From the larger cross section image of sample I, we can observe that the different GaSb islands of the sample exhibits {111} facets and the same height and flatness. In contrast, sample J exhibits mainly 60° MDs because the additional half lattice

planes are all separated. The 60° MDs are distributed in a 3 nm wide interfacial zone extending on both sides of the nominal interface.

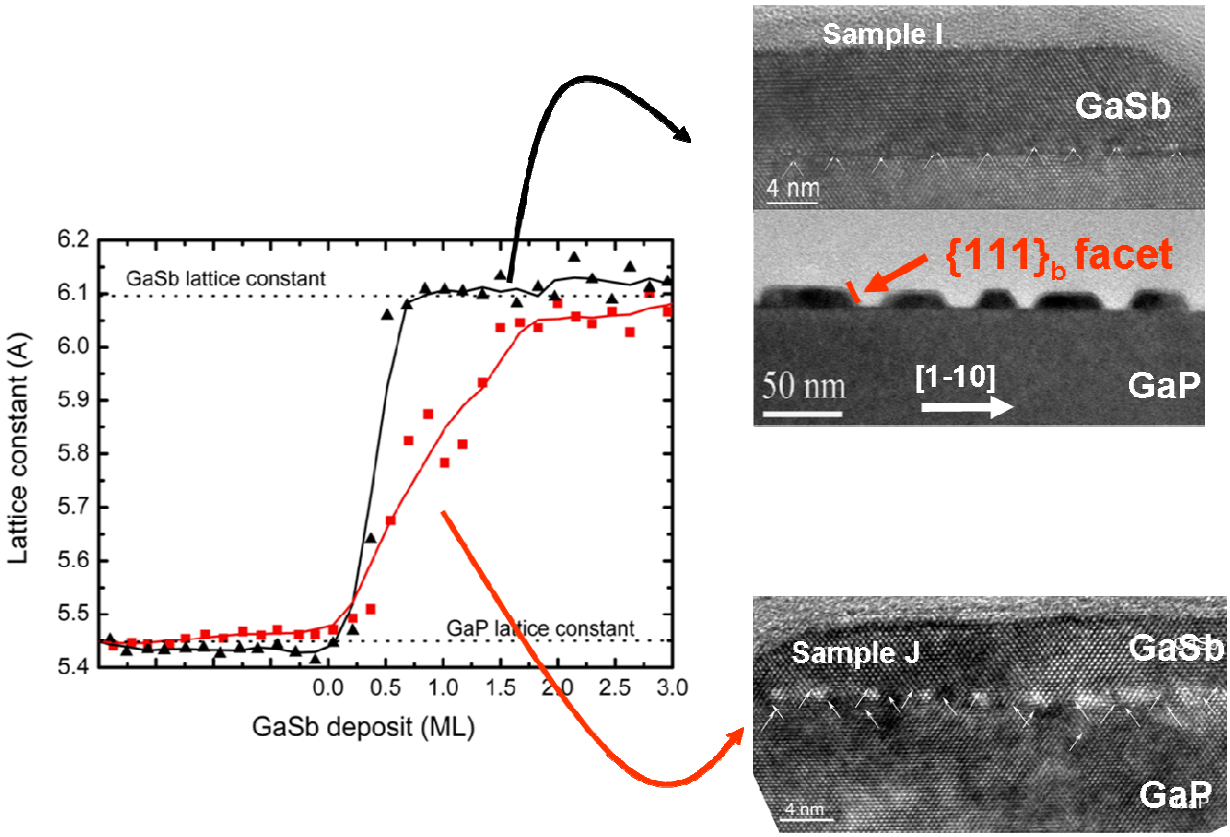

***Figure III.17**: The graph presents lattice constant evolution during the first 3 GaSb ML deposition on an Sb-rich (sample I) and a Ga-rich (sample J) GaP surface. On the right side, cross-sectional high-resolution TEM images of both samples are presented along the [1-10] zone axis [17].*

III.1.C. Conclusion

After studying the influence of the surface reconstruction on the growth of GaSb on the highly mismatched GaAs and GaP substrates, we can conclude that the (2x8) Sb-rich Ga(P,As) surface preparation promotes the growth of relaxed GaSb islands via the formation of a periodic array of 90° MDs at the epilayer/substrate interface. Although we have shown that the (2x8) reconstruction is the best preparation for the relaxation of GaSb, the studies we want to present in the following are not all prepared with this reconstruction. According to the sample involved, we will give detailed information for the surface reconstruction and growth parameters. We will however demonstrate that this won't affect the conclusions that will be drawn.

III.2. Influence of the experimental parameters on the early stages of GaSb growth

All the samples used in this paragraph are presented in Table III.1. The Table is divided into 5 sets of samples Tx, Ty, Tz, Vz and S, each one for a different study. The detailed process for each sample and set is explained during the result presentation.

III.2.A Influence of the growth temperature (Tg)

Three sets of samples T_x, T_Y and T_Z are first used to investigate the role of the growth temperature on the nucleation process of GaSb on GaAs (T_x, T_Y) and GaP (T_Z) substrates. 10 MLs of GaSb are deposited on a (1x4) Sb-rich surface for set T_x and a (2x8) Sb-rich reconstruction for sets T_Y and T_Z. For all the samples, Ga and Sb fluxes are equal to 0.7 and 2.5 ML/s, respectively. As mentioned before, once the GaSb growth begins on a GaP substrate whatever the growth temperature between 450 and 510°C, the RHEED turns rapidly from a two-dimensional to a 3D one due to the very large lattice mismatch between GaSb and GaP (11.7%). On the other hand, the growth on GaAs is different: at low growth temperature (~ 450°C), a quasi-2D growth mode occurs whereas it is three-dimensional (3D) at 510°C with the formation of relaxed islands which subsequently coalesce to give rise to the epilayer [18].
The AFM images of all the samples of the 3 sets are given in figures III.18, 19, 20 for sets T_x, T_Y and T_Z, respectively. In these figures, the GaSb surface coverage and the mean island height along the (1x1) μm^2 AFM images are given in function of the growth temperature. In set T_Z (fig. III.20), the AFM image and analysis of the sample at 530°C (sample T_{z4}) are given for a (5x5) μm^2 scan area to show that two kinds of GaSb islands are formed and a meaningful GaSb surface coverage cannot be established for this sample. This can be attributed to the excessive re-evaporation of Sb at high temperatures leading to a large Ga adatom diffusion length. Larger islands grow due to the coalescence of smaller ones [19]. The behavior of the mean height is the same for all the sets regardless of the starting substrate surface: the mean height increases with the growth temperature. This evolution seems to agree with common kinetics: at low temperatures, the reduced Ga adatom diffusion length should induce a large density of small GaSb islands. Hence, a meaningful density value at 10 MLs cannot be established due to the nearly full coalescence in some samples. Therefore, the surface coverage instead of the island density is presented in function of the growth temperature in the figures.

Sample	Substrate	Initial surface	Growth rate (ML/s)	Temperature growth (°C)	Sb flux (ML/s)
T_{x1}	GaAs	(1x4) Sb-rich	0.7	460	2.5
T_{x2}	GaAs	(1x4) Sb-rich	0.7	480	2.5
T_{x3}	GaAs	(1x4) Sb-rich	0.7	510	2.5
T_{y1}	GaAs	(2x8) Sb-rich	0.7	460	2.5
T_{y2}	GaAs	(2x8) Sb-rich	0.7	480	2.5
T_{y3}	GaAs	(2x8) Sb-rich	0.7	510	2.5
T_{z1}	GaP	(2x8) Sb-rich	0.7	450	2.5
T_{z2}	GaP	(2x8) Sb-rich	0.7	480	2.5
T_{z3}	GaP	(2x8) Sb-rich	0.7	510	2.5
T_{z4}	GaP	(2x8) Sb-rich	0.7	530	2.5
V_{z1}	GaP	(2x8) Sb-rich	0.1	480	2.5
V_{z2}	GaP	(2x8) Sb-rich	0.4	480	2.5
V_{z3}	GaP	(2x8) Sb-rich	0.7	480	2.5
V_{z4}	GaP	(2x8) Sb-rich	1	480	2.5
S_1	GaP	(2x8) Sb-rich	0.7	510	1
S_2	GaP	(2x8) Sb-rich	0.7	510	2.5
S_3	GaP	(2x8) Sb-rich	0.7	510	7.3

Table III.1: *Samples corresponding to the growth of 10 MLs GaSb on (001) GaAs (set T_x) and GaP (sets T_y, T_z, V_z and S) substrates.*

From the three sets, the surface coverage decreases with the temperature. The reduced Ga diffusion length at low temperatures leads to a faster island coalescence inducing a large surface coverage. However, one can notice that decreasing the growth temperature leads to more elongated islands in the [110] direction. For example, the calculated mean aspect ratio $L_{[110]}/L_{[1\text{-}10]}$ (where $L_{[110]}$ and $L_{[1\text{-}10]}$ are the island length along each direction) for the samples of set T_z given on the images of figure III.20 gives 1.86 for sample T_{z2} whereas it is 1.36 for sample T_{z3}.

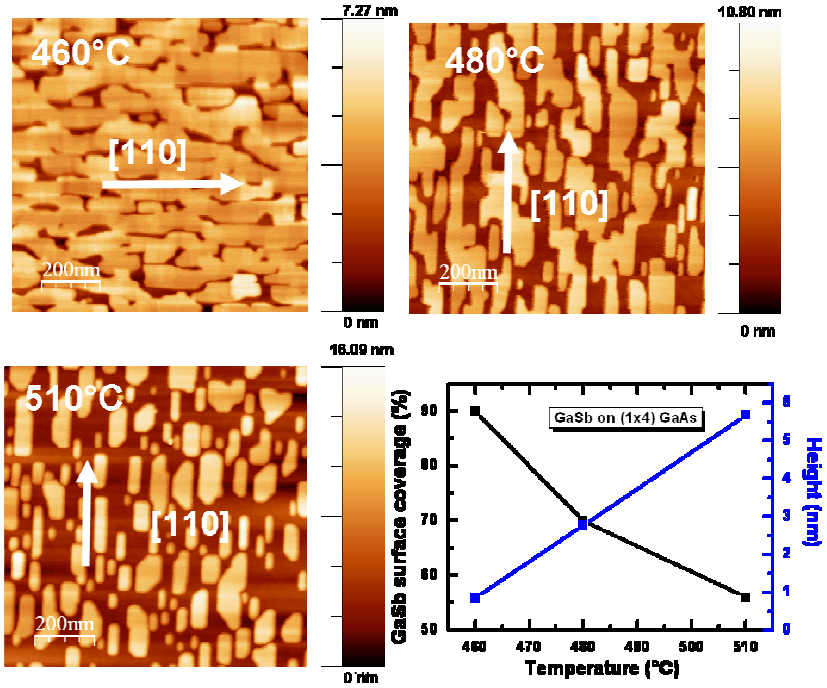

Figure III.18: *AFM images of samples T_{x1} (450°C), T_{x2} (480°C) and T_{x3} (510°C). The graph presents the height and surface coverage of GaSb islands versus growth temperature for set T_x.*

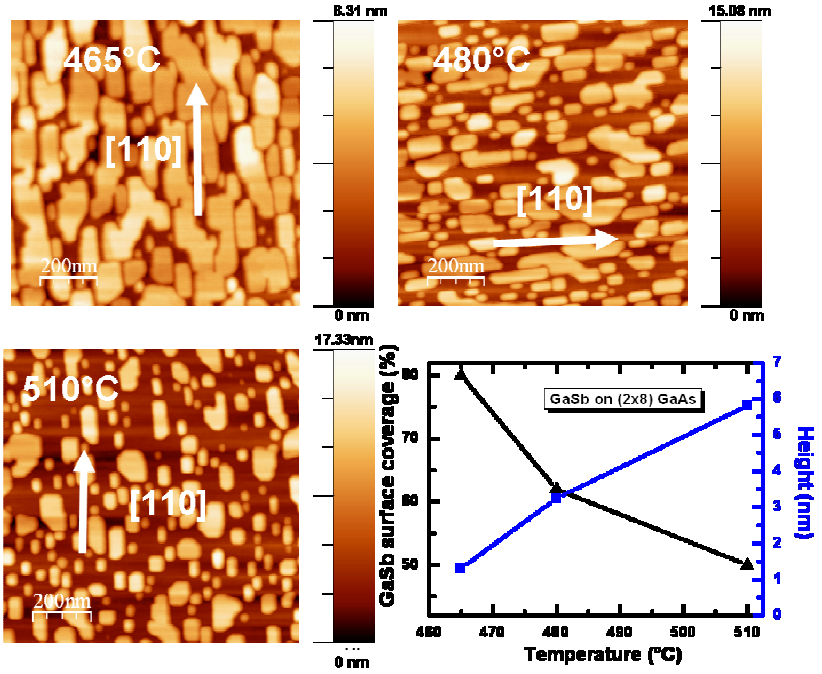

Figure III.19: *AFM images of samples T_{y1} (465°C), T_{y2} (485°C) and T_{y3} (510°C). The graph presents the height and surface coverage of GaSb islands versus growth temperature for set T_y.*

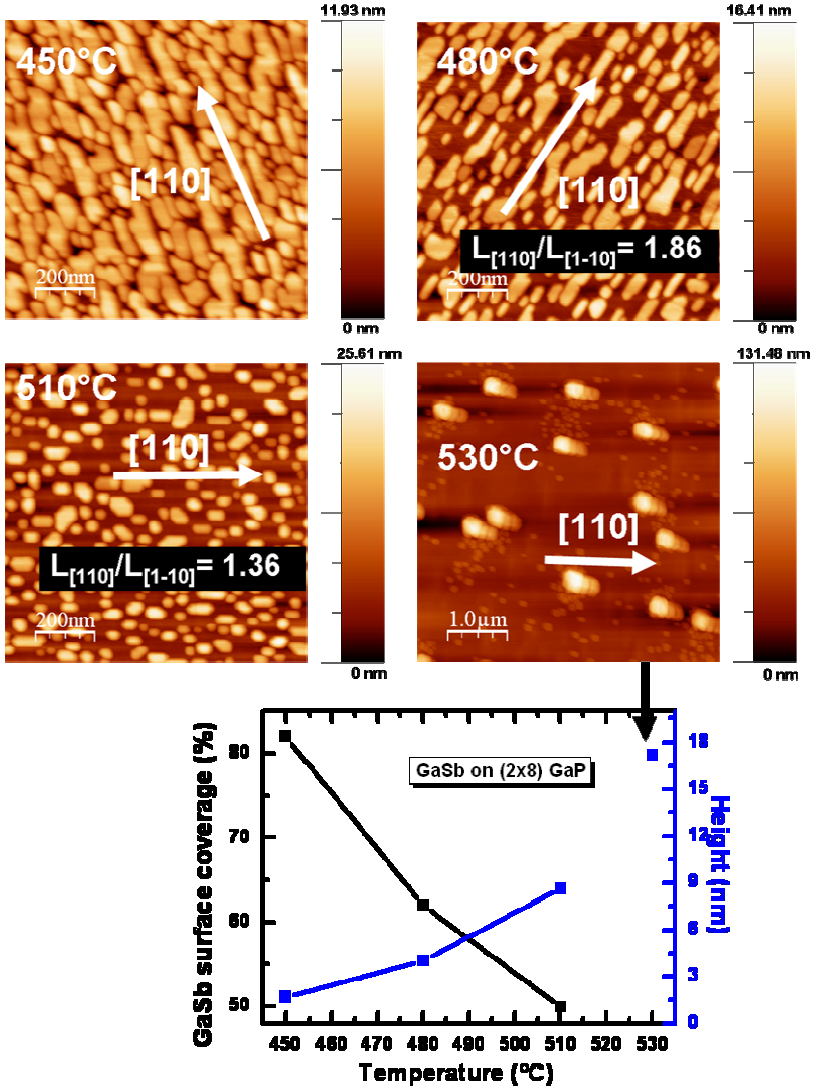

Figure III.20: *AFM images of samples T_{z1} (450°C), T_{z2} (480°C), T_{z3} (510°C) and T_{z4} (530°C). $L_{[110]}/L_{[1-10]}$ represents the mean aspect ratio where $L_{[110]}$ and $L_{[1-10]}$ are the island length along each direction. A meaningful aspect ratio for T_{z1} cannot be established due to a nearly full coalescence at 450°C. The graph presents the height and surface coverage of GaSb islands versus growth temperature for set T_z..*

This would imply an increase of the Ga adatom diffusion length along the [110] direction, unexpected when decreasing the growth temperature [20]. We note that a meaningful aspect ratio in sample T_{z1} cannot be established due to a nearly full coalescence in the [110] direction at these low temperatures.

TEM analyses were then used to investigate the influence of the growth temperature in set T_z on the misfit dislocations at the interface between GaSb and GaP (fig. III.21). As can be seen sample T_{z3} exhibits mainly 60° MDs because the additional half lattice planes are all separated. In contrast, sample T_{z1} shows a regular periodic array of 90° MDs confined at the interface.

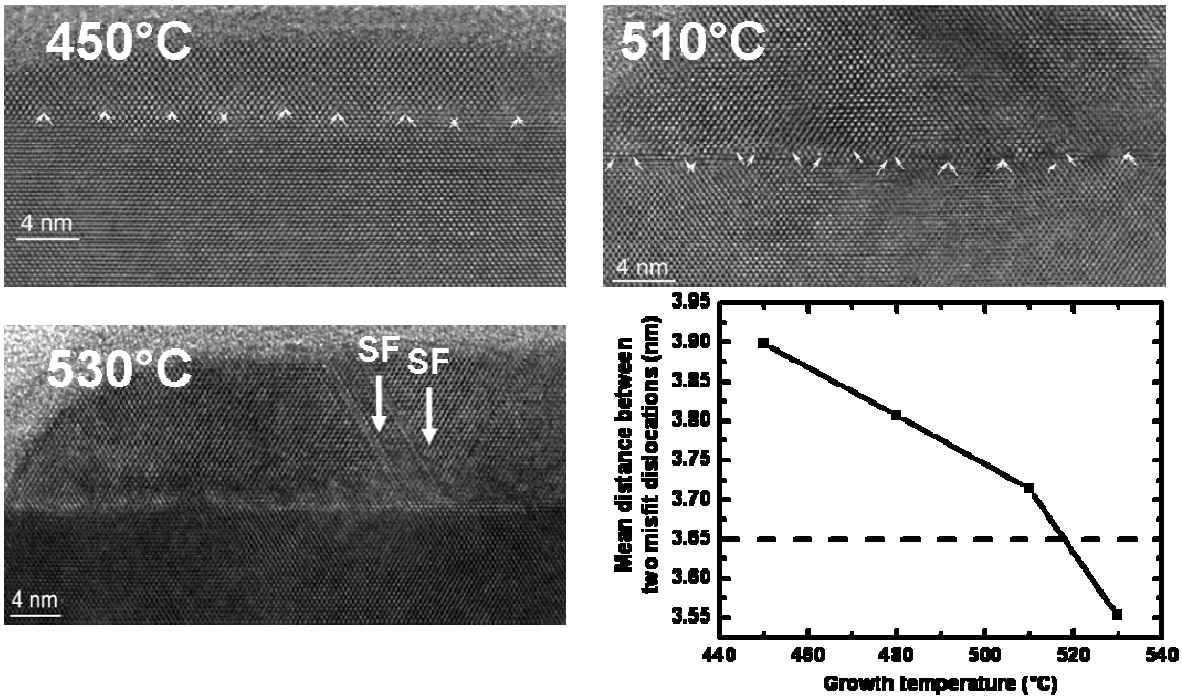

Figure III.21: *Cross-sectional high-resolution TEM images along the [110] zone axis of samples T_{z1}, T_{z3} and T_{z4} grown at 450, 510 and 530°C, respectively. Arrows indicate 60° and 90° MDs at the interface between the substrate and buffer layer. The graph presents the mean distance between MDs at the GaSb/GaP interface vs GaSb growth temperature. The ideal distance for a perfect relaxation by 90° MD is indicated by the horizontal dashed line [17].*

The mean value corresponding to the spacing of the MDs is presented in the graph of figure III.21. This mean value is statistically obtained after the TEM cross section observations on several islands. The same measurement is performed for all the growth temperatures from 450 to 530°C. For the GaSb/GaP system, the theoretical distance between two 90° dislocations for full strain relaxation amounts to 3.65 nm (dashed line in the graph). This graph shows that high growth temperatures promote island relaxation (510°C). Furthermore, the measured distance between dislocations at 530°C is smaller than the theoretical value: this is actually due to the formation of many 60° MDs. This result is consistent with the above results relative to the surface preparation. Indeed, the increase of the growth temperature favours Sb re-evaporation turning back to the case of a Ga-rich surface, where 60° MDs appear rather than 90° MDs. The TEM image of this sample (T_{z4}) confirms this conclusion where SFs are observed which will contribute with the MDs to the strain relaxation of the island.

The fine structure of the misfit dislocations of samples T_{y1} and T_{y3} grown at 465°C and 510°C observed along the [110] direction are given on figure III.22. The insets show the α_{13}

component of the dislocation tensor field derived from the highlighted area of the two TEM images. Here, we have chosen to define 90° (or Lomer) MDs as two additional intersecting lattice planes and a core separation lower than 1 nm whereas the closely spaced 60° dislocations are characterized by a core distance larger than 1 nm. As can be noticed, the cores of the MDs at 465°C are more compact than those at 510°C. The distances between the pair of cores have been determined in many areas (more than 50 pairs of dislocations for each sample); the results are presented in the graph of figure III.22. The spacing of the pair cores are highly related to the growth temperature. In the samples with 10 and 15 MLs grown at 465 °C (2D growth mode), most of the misfit dislocations are 90° MD type. At higher growth temperature (3D growth mode), both 90° MDs and closely spaced 60° dislocation pairs are observed.

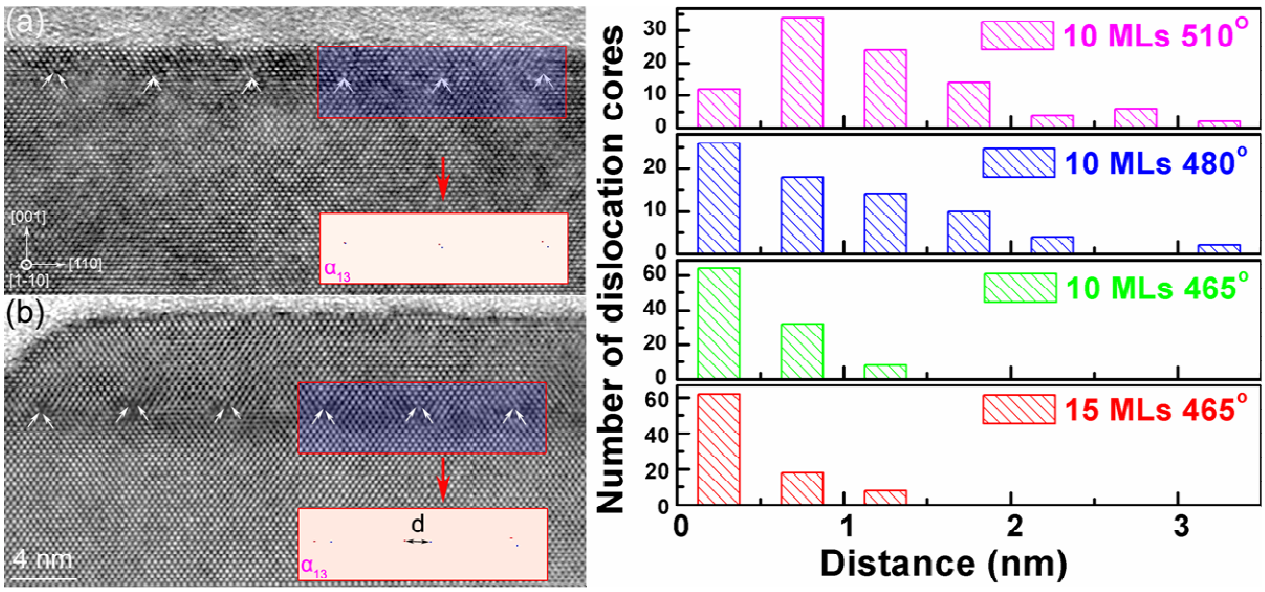

Figure III.22: *Cross-sectional HRTEM images of GaSb on GaAs observed along [1-10] orientation.In the inset figures, the dislocation cores are easily determined from the highlighted area of HRTEM by GPA. The graphs present the distance (d, as shown in the insets) between the interface 60° dislocation pair vs. the growth conditions [18].*

In summary, the results on the influence of the growth temperature on GaSb island formation on both GaAs and GaP substrates show strong similarities. The AFM analyses show that the temperature decrease favours the island coalescence in the [110] direction. TEM analyses indicate that the type of the MDs is highly dependent on the growth temperature. Our observations on the two substrates suggest that low temperatures (where also Sb re-evaporation

is lower i.e. Sb overpressure is higher) promote 90° MDs formation whereas 60° dislocations and closely spaced 60° pairs are predominant at higher temperatures.

To understand the behaviour of the strain relaxation in function of the growth temperature, we use the explanation proposed by Wang et al. [18] who used a 60° dislocation glide model in combination with surface effects to explain the formation of Lomer, 60°, and 60° dislocation pair at high or low mismatch hetero-interfaces between zinc-blende materials.

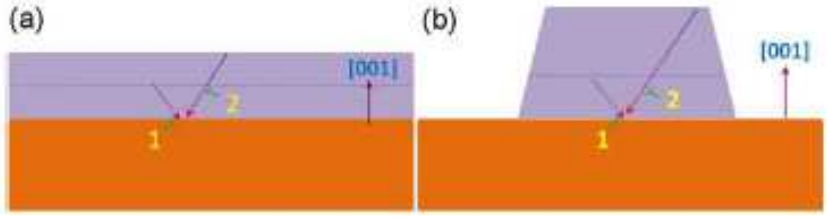

Figure III.23: *The schematic formation mechanism of the misfit dislocations in 2D (a) and 3D (b) growth modes. The dotted horizontal line shows the critical thickness for the formation of the first set of misfit dislocation [18]*

They showed that the distance between the second and first set of dislocations in the 3D islands (high growth temperature) is expected to be larger than in the 2D layer (or low growth temperature) (see fig. III.23). This will help in the formation of two 60° dislocations that have opposite screw components ($b_{1s} = -b_{2s}$) in the 2D growth mode and confines the lattice mismatched strain at the hetero-interface of GaSb. In contrast, 60° dislocations and closely spaced 60° pairs are predominantly generated in the 3D growth mode since 60° pairs have parallel screw components ($b_{1s} = b_{2s}$).

At the end of this study, it is clear that the core distance between two 60° MDs increases with the growth temperature. Low temperatures decrease this distance leading to very well confined 90° MDs. This will however also reduces the distance between two Lomer MDs leading to a much lower strain relaxation.

III.2.B. Influence of the growth rate (V_{Ga})

Four samples V_{z1}, V_{z2}, V_{z3} and V_{z4} are used to investigate the influence of the Ga growth rate on the GaSb island formation on GaP. For all the samples, the Sb flux is fixed at 2.5 ML/s. 10 MLs of GaSb are deposited on a (2x8) GaP reconstruction surface at 480°C by varying the Ga growth rate from 0.1 for sample V_{z1} up to 1 ML/s for sample V_{z4}. The density,

the mean height and the aspect ratio $L_{[110]}/L_{[1\text{-}10]}$ along the (1x1) μm^2 AFM images are given in function of the Ga growth rate in figure III.24:

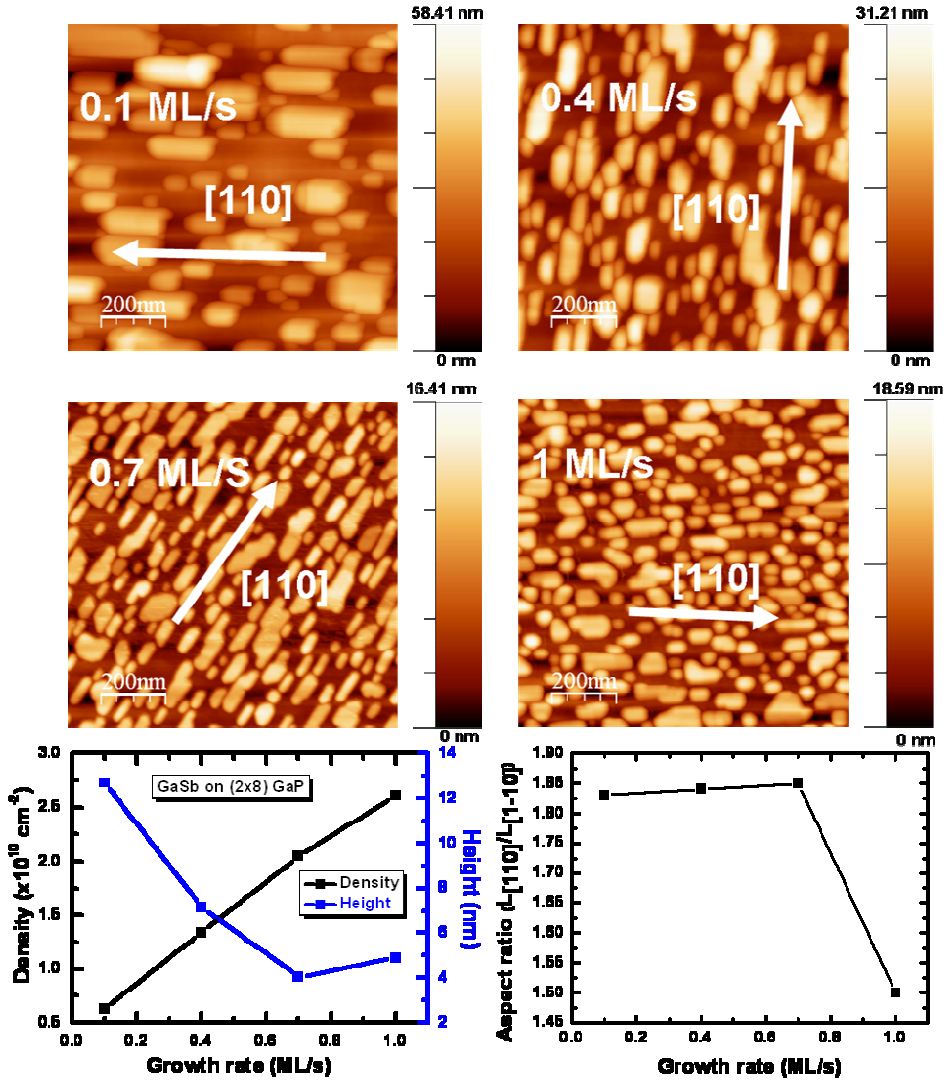

Figure III.24: *AFM images of samples V_{z1} (0.1 ML/s), V_{z2} (0.2 ML/s), V_{z3} (0.7ML/s) and V_{z4} (1 ML/s). The left graph presents the height and density of GaSb islands versus growth rate for set V_z. whereas the right graph presents the aspect ratio $L_{[110]}/L_{[1\text{-}10]}$ in function of the growth rate.*

The AFM analyses show that the island density increases with the growth rate. This result is in agreement with the evolution predicted by classical nucleation theory. High growth rates decrease the diffusion length of Ga adatoms leading to a larger density of small islands. This can be also confirmed by the mean height evolution. However, one can notice a small increase of the mean height between sample V_{z3} and V_{z4} (see explanation in the discussion section). The islands recorded on all the samples are elongated in the [110] direction with a mean aspect

ratio $L_{[110]}$ / $L_{[1-10]}$ around 1.85 for the first three samples. However, at very high Ga growth rate (1 ML/s) the aspect ratio drops off to nearly 1.5 (see also the discussion section).
The mean spacing of the MDs and the mean relaxation calculated by GPA are given for set V_z in function of the growth rate on figure III.25.

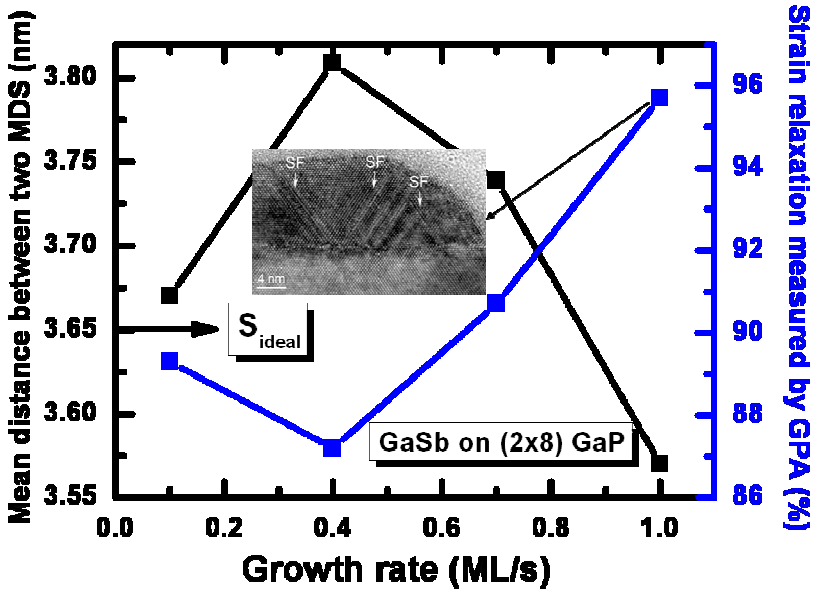

Figure III.25: *Relaxation of GaSb islands from RHEED analysis in the [1-10] direction vs. distance between MDs from cross-section TEM images. The ideal distance for a perfect relaxation by 90° MD is indicated by the horizontal dashed line [24].*

The sample at 1 ML/s exhibits the highest strain relaxation but the measured distance between dislocations is smaller than the theoretical value: this is due to the formation of many 60° MDs. This result is also consistent with the above results relative to the surface preparation and the growth temperature. Indeed, the increase of the growth rate implies a decrease of Sb overpressure turning back to the case of a Ga-rich surface, where 60° MDs appear rather than 90° MDs. The TEM image of this sample also shows many SFs (inset given in the graph). This means that both stacking faults and misfit dislocations contribute to the strain relaxation in sample V_{z4} and thus a higher strain relaxation is observed.

Obviously from the studies of the growth temperature and the growth rate influence, one should take into account the influence of the Sb overpressure. Indeed, decreasing the growth rate as well as the growth temperature with a constant Sb flux induces an increase of the V/III ratio. Therefore Sb overpressure can be probably the key factor in the islands formation. In the next section we study the influence of the Sb flux variation on the growth of GaSb islands.

III.2.C. Influence of the Sb flux

Three samples S_1, S_2 and S_3 are grown at 510°C on GaP with a constant Ga growth rate of 0,7 ML/s and an Sb flux of 1 ML/s, 2.5 ML/s and 7.3 ML/s, respectively, during GaSb deposition. For all the samples, the Sb flux is fixed at 2.5 ML/s while preparing the (2x8) reconstruction surface before the 10 ML GaSb growth. Figure III.26 displays AFM images of GaSb islands on GaP within a (1 x 1 μm^2) scan area of the samples S_1, S_2 and S_3. In sample S_1, the formation of two kinds of GaSb islands (L and S) can be attributed to the large Ga adatom diffusion length under very low Sb flux. This result is consistent with the above result relative to sample T_{z4} and V_{z4}. Figure III.26d displays the density and the mean aspect ratio $L_{[110]}/L_{[1-10]}$ of GaSb islands in function of the Sb flux.

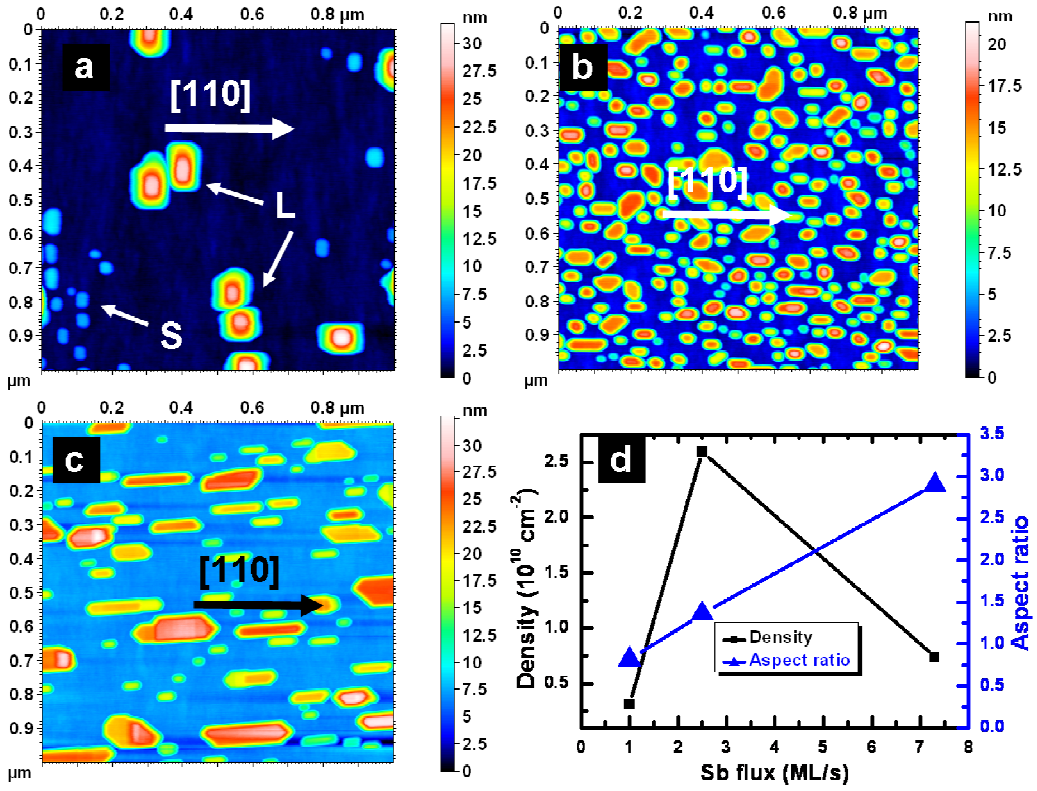

Figure III.26: *AFM images of samples S_1, S_2 and S_3: 10 ML GaSb grown on GaP at 510°C with a Sb flux of 1ML/s (a), 2.5 ML/s (b) and 7.3 ML/s (c), respectively. (d) Density (black squares) and mean aspect ratio (blue triangles) of GaSb islands in function of the Sb flux during GaSb island growth [25].*

For the first two samples, the density increases with the Sb flux, which is a common behaviour observed during III-V MBE growth where a high group-V element flux reduces the group-III element diffusion length [11]. However for very high Sb fluxes (sample S_3) this behaviour is

completely reversed and a lower density of large islands is observed. GaSb islands are slightly elongated in the [1-10] direction at low Sb flux and in the [110] direction when this flux is increased. An aspect ratio near unity corresponds to the maximum island density.

Cross-sectional HRTEM images of samples S_1, S_2 and S_3 are shown on figure III.27. Sample S_1 exhibits islands with a nearly elliptical shape with SFs as indicated by the pink arrows in figure 27a. As can be seen in the figure, in addition to the interface misfit dislocations, stacking faults form inside the two (111) families of lattice planes and run over to the surface.

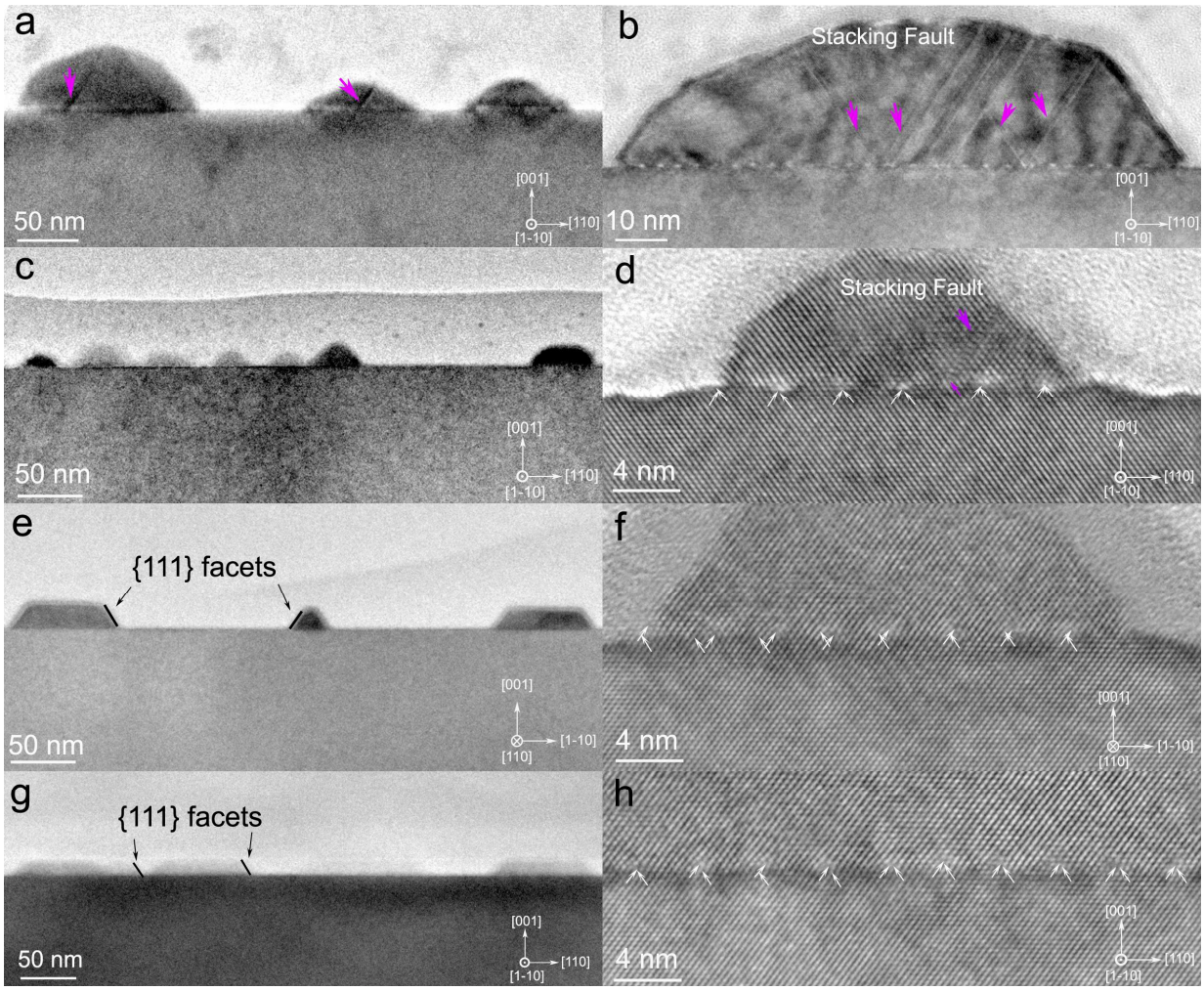

Figure III.27: *Cross-sectional high resolution TEM images of samples S_1 (a, b) and S_2 (c,d) in the [110] direction. Cross-sectional HRTEM images of sample S_{13} in the [1-10] (e,f) and [110] (g,h) directions, respectively. White arrows mark the termination of {111} lattice planes in the GaP substrate. Pink arrows on figures b and d underline the presence of stacking faults [25].*

As for T_{z4} and V_{z4}, this may indicate that the islands reach a complete strain relaxation by the formation of such high densities of defects, at the interface and in their volume.

In sample S_2 (fig. III.27c), the shape of the island evolves with facets that start to appear. As shown in figure III.27d, an array of misfit dislocations also forms at the interface and in this case very few stacking faults can be seen (arrow). Figures III.27 e-h show the islands in sample S_3 along the [110] (fig. III.27 e-f) and [1-10] (fig. III.27 g-h) directions. These islands are flat with a tetragonal shape and are limited by well defined {111} and {001} facets with no stacking faults. In these HRTEM images, the 90° dislocation array forms in both [110] and [1-10] directions.

III.2.D. Discussion

Coming back to the evolution with the growth temperature, one can conclude from the V/III ratio observations that two effects are competing and acting conversely on the Ga adatom diffusion length. Lowering the growth temperature reduces this length inducing a large density of islands, but since a larger V/III ratio is reached at low Tg, the length is increased in the [110] direction, leading to a fast island coalescence. On the other hand, decreasing the growth rate also increases the V/III ratio, and hence the Ga diffusion length.

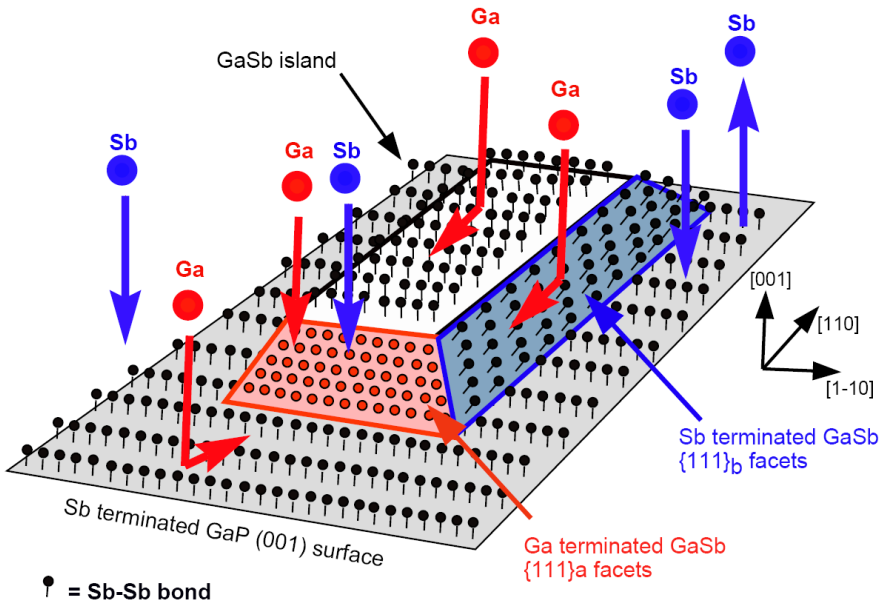

Figure III.28: *Schematic illustration of the Ga adatom behavior and growth mechanism of {111}-facetted islands at high Sb overpressure leading to [110] elongated islands [25].*

To explain the above depicted behaviours, one should take into account the Sb coverage of the surface in each case. At high Sb overpressure, an Sb coverage larger than 1 ML with the formation of Sb-Sb bonds on the surface has been reported for both the (001) GaSb [26] and the (2x8) Sb-terminated (001) GaAs surfaces [27]. In our study, the (2x8) reconstruction is a

strong indication of the formation of Sb-Sb bonds at the substrate surface. Since the strengths of Ga-Sb and Sb-Sb bonds on the surface are rather similar [28], the driving force to break an Sb-Sb bond and form a Ga-Sb one is rather low. Then the Ga incorporation is reduced and its diffusion is enhanced. As mentioned before, high Sb fluxes promote the formation of fully relaxed islands with well-defined {111} facets. As illustrated in figure III.28, on the Sb-terminated $\{111\}_b$ facets, the Sb-Sb bonds on the surface will impede Ga adatom incorporation and favours it on Ga-terminated $\{111\}_a$ facets. These latter advance faster leading both to the observed [110] island elongation and to the reduced island density.

After connecting the experiments of the growth temperature, the growth rate and the V/III ratio on either GaAs or GaP substrates, we present in figure III.29, a sketch displaying the effect of these growth conditions on the adatom diffusion length λ_{Ga}.

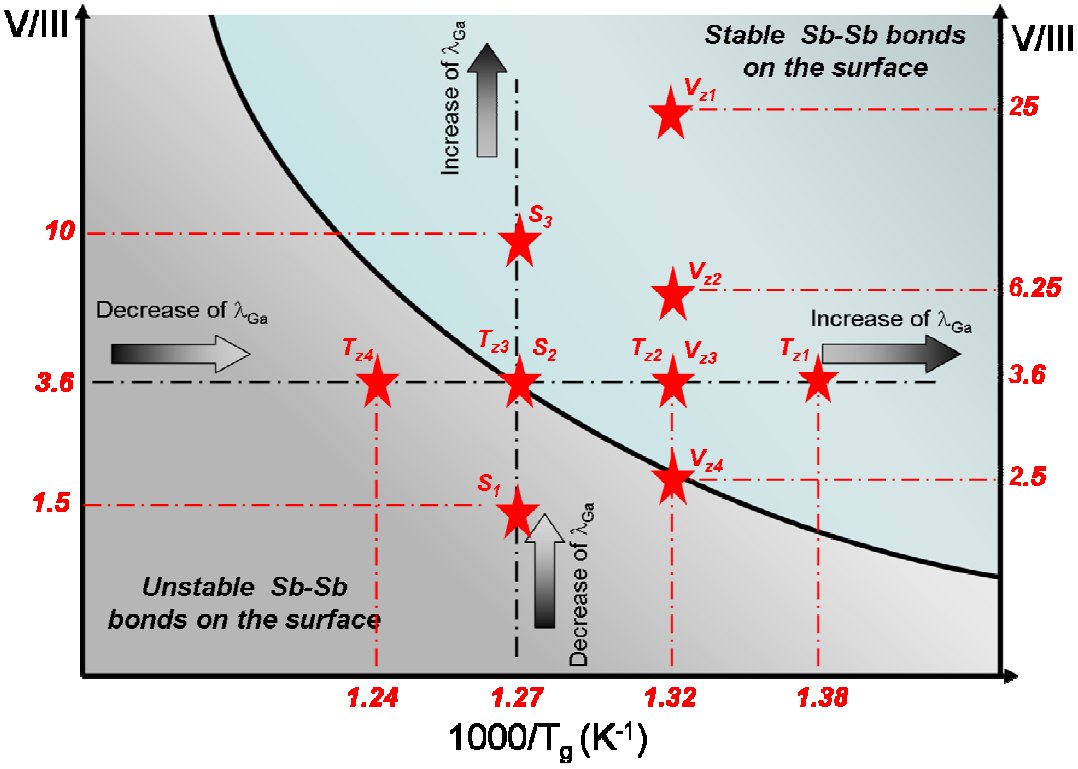

Figure III.29: *Qualitative description of the evolution of Ga adatom diffusion length versus growth conditions. The black line separates two domains (stable Sb-Sb bonds and unstable Sb-Sb bonds) where the influence of the growth condition is reversed. The positions in the two domains corresponding to the growth conditions used for the different samples are indicated by red stars.*

The black line separates two domains of growth conditions, depending on whether or not stable Sb-Sb bonds are present on the surface. Above the line, stable Sb-Sb bonds reduce Ga incorporation and lead to an increased Ga diffusion length in agreement with the evolutions

observed in samples T_{z1} (or T_{x1} and T_{y1}), T_{z2} (or T_{x2} and T_{y2}) and T_{z3} (or T_{x3} and T_{y3}), in samples S_2 and S_3 and in samples V_{z1}, V_{z2} and V_{z3}.

Below the line, only standard kinetics governs the evolution of the Ga adatom diffusion length. The evolution observed between samples T_{z3} and T_{z4} and between S_1 and S_2 enters completely this domain. Furthermore, the evolution between samples V_{z3} and V_{z4} happens at the limit of the black line. This could be an explanation why a slight increase of the height is observed in sample V_{z4} compared to sample V_{z3} where the V/III ratio effect on the Ga adatom diffusion length begins to decrease. This can be also confirmed by the drop off of the aspect ratio in sample V_{z4} (see fig. III.24).

It is important to mention that the above effect is directly related to the relative strength of Sb-Sb and Ga-Sb bonds. For arsenides and phosphides, even if stable V-V bonds are formed on the surface, they don't much affect the group-III element diffusion length since As-As and P-P bonds are significantly weaker than Ga-As and Ga-P ones [28]. This peculiar behaviour is also linked with the typical growth conditions for antimonides, for which the principle of the 3 temperatures (see chapter II) is not completely fulfilled, T_V being equal or higher than T_S.

III.2.E. Conclusion

In conclusion, we have studied the influence of the growth conditions on the initial nucleation process of GaSb islands on highly mismatched substrates. It is shown that between low and medium Sb overpressure values, standard kinetics drive the GaSb island formation. A low Sb overpressure promotes the appearance of elliptical shape islands with a lot of 60° MDs. This will hence induce the formation of a high density of stacking faults with a higher strain relaxation. By increasing the Sb overpressure the relaxation is progressively favoured by 90° misfit dislocations at the GaSb/Ga(As,P) interface with less SFs. Under high Sb overpressures, the GaSb islands are more elongated in the [110] direction with the formation of {111} facets at the islands edge, their density decreases and they are relaxed by the formation of 90° MDs at the island-substrate interface. We relate this observation to an enhancement of Ga diffusion due to the strength of Sb-Sb bonds present on the surface when the effective Sb flux on the surface is increased. The experiments varying the growth temperature and the growth rate at fixed Sb flux confirm this finding.

III.3. Towards island coalescence

A study was performed to investigate the influence of the epilayer thickness on both GaSb relaxation and misfit dislocation behaviour. Table III.2 presents all the samples that were used for this study. The Table is divided into 3 sets of samples A, B and C corresponding to the growth of GaSb on a (2x8) GaAs surface at 460, 480 and 510°C, respectively.

Sample	Surface reconstruction	Temperature growth (°C)	Thickness (ML)
A1	**(2x8) Sb-rich**	**465**	**10**
A2	**(2x8) Sb-rich**	**465**	**27**
A3	**(2x8) Sb-rich**	**465**	**40**
B1	**(2x8) Sb-rich**	**485**	**10**
B2	**(2x8) Sb-rich**	**485**	**27**
B3	**(2x8) Sb-rich**	**485**	**100**
C1	**(2x8) Sb-rich**	**510**	**10**
C2	**(2x8) Sb-rich**	**510**	**27**
C3	**(2x8) Sb-rich**	**510**	**300**

Table III.2: *All the samples correspond to the growth of GaSb on (001) GaAs substrates. The Ga growth rate in GaSb is 0.7 ML/s for a V to III ratio equal to 3.5.*

The (1 x 1) μm^2 AFM images of all the samples are given on figure III.30. In the graph of this figure we present the GaSb coverage in function of the growth temperature of all the samples. As expected, the coalescence happens faster at low temperatures: the surface coverage reaches nearly 97 % for 27 MLs of GaSb growth at 460°C (set A) whereas at 510 °C (set C), even for 300 MLs, the surface coverage is only 90%. From this latter result, one can doubt that a satisfying surface morphology can be achieved after a reasonable buffer thickness (about 0.6 µm) grown at 510°C. On the other hand, a low growth temperature promotes the formation of 90° dislocations but limits the strain relaxation.

An additional observation on the MD behaviour is shown on figure III.31. Here we have studied the growth of GaSb by increasing the thickness of sample T_{x1} (GaSb on (1x4) GaAs surface at 460 °C) until 40 MLs keeping the 2D growth mode. As can be noticed, there is an improvement of the strain relaxation state (blue open square). The average distance of Lomer dislocations (red open circle) seems also to decrease with the thickness.

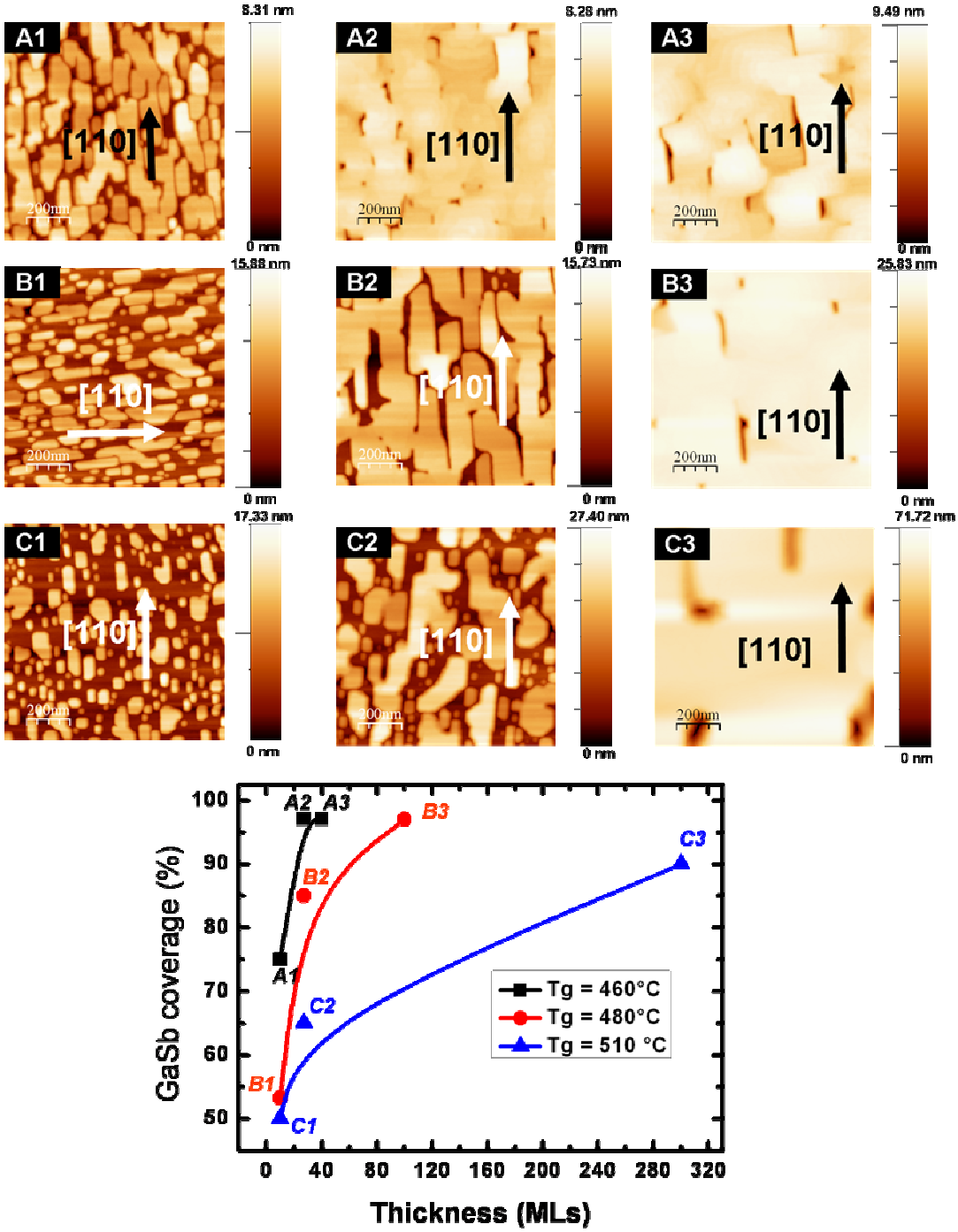

Figure III.30: *AFM images of all the samples of sets A, B and C. The graph presents the surface coverage of GaSb islands versus the growth thickness for different growth temperatures.*

This result is in agreement with the one already observed by Babkevitch et al. [29] using high-resolution x-ray diffraction techniques, who claimed that the spacing between the dislocations for both the [110] and [1-10] directions decreases as the layer thickness increases. However the final relaxation state is still far from full accommodation.

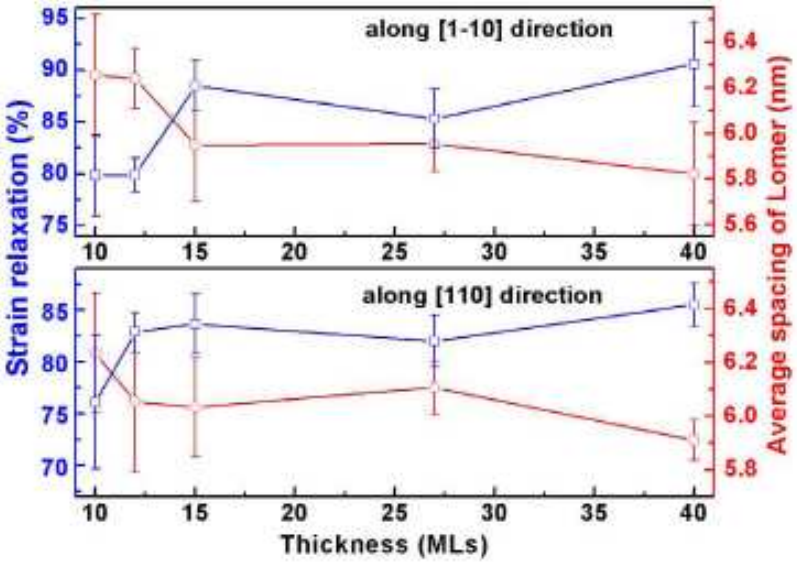

Figure III.31: *(Colour on-line) The strain relaxation (blue open square) and average distance of Lomer dislocations (red open circle) as a function of epitaxial layer thickness in 2D growth mode [19].*

In summary, starting the nucleation at low temperature seems to be required to promote both rapid coalescence and nice 90° MD cores. However, it also impedes the strain relaxation even with increasing the thickness. Then, one way to circumvent this problem could be to perform an annealing of the low temperature grown fully coalesced nucleation layer.

III.4 Conclusion

In this chapter, we have made a detailed study of the influence of the experimental conditions on the growth of GaSb on GaAs and GaP, highlightening similar critical parameters for both substrates. After showing that the (2x8) is the best surface reconstruction for the strain relaxation of GaSb by an interfacial 90° MD array, we present a summary on the main conclusions deduced from this chapter.

1) Growth temperature

- Low growth temperatures promote 2D growth and GaSb relaxation via 90° MDs, but strain relaxation remains partial.
- Increasing the growth temperature leads to a larger Ga diffusion length inducing a small density of large and well relaxed GaSb islands. However, the growth mode is mainly 3D with a delayed coalescence; 60° dislocations and closely spaced 60° pairs are predominant at high temperatures with the formation of SFs.

2) Growth rate

- At very low growth rates, a small density of large GaSb islands is formed where only 90° MDs are responsible for the strain relaxation.
- Higher growth rates decrease the Ga diffusion length inducing a large density of small GaSb islands that are relaxed with 60° misfit dislocations and the formation of SFs.

3) V/III ratio

- At low V/III values, standard kinetics drive the GaSb island formation. A low Sb flux promotes the appearance of elliptical shape islands with more 60° MDs and SFs.
- By increasing the Sb flux, the relaxation is progressively favoured by 90° misfit dislocations at the GaSb/Ga(As,P) interface with less SFs. Under high Sb flux, the GaSb islands are more elongated in the [110] direction with the formation of {111} facets at the islands edge, their density decreases and are relaxed by only the formation of 90° MDs.

In the light of these results, two ways can be considered for the growth of the nucleation layer:

1) a high growth temperature combined with a high V/III ratio to achieve fully relaxed flat islands with an optimized 90° MD network. However, a 3D growth mode cannot be avoided in this case and the question arises about the impact of island coalescence on threading defects.

2) A low growth temperature with a lower V/III ratio to promote a 2D growth mode and compact 90° dislocation cores. However, the mismatch is only partially accommodated in this case and further plastic deformation is required for full relaxation.

The impact of these two approaches on the transport properties of AlSb/InAs heterostructures will be evaluated on both GaAs and GaP substrates in the next chapter.

References

[1] A. Othake, Surf. Sci. Reports **63** (2008) 295

[2] B. A. Joyce, Rep. Prog. Phys. **48** (1985) 1637.

[3] N. Grandjean, PhD in physics "Phénomènes de surface en croissance épitaxiale fortement contrainte de (In,Ga)As sur GaAs : relaxation élastique, transition 2D-3D, effet surfactant", University of Nice-Sophia Antipolis, February (1994)

[4] Q. Xue, T. Hashizume, J. M. Zhou, T. Sakata, T. Ohno and T. Sakurai, Phys. Rev. Lett. **74** (1995) 3177

[5] L. J. Whitman, B. R. Bennett, E. M. Kneedler, B. T. Jonker, B. V. Shanabrook , Surf. Sci. **436** (1999) L707

[6] P. Moriarty, P. H. Beton, Y. R. Ma, D. A. Woolf and M. Henini, Phys. Rev. B **53** (1996) R16148

[7] P. Laukkanen, R. E. Perala, R. L. Vaara, and I. J. Vayrynen, Phys. Rev. B **69** (2004) 205323

[8] J. Massies and N. Grandjean, Phys. Rev. Lett. **71** (1993) 1411

[9] Y. Wang, P. Ruterana, L. Desplanque, S. El Kazzi and X. Wallart, Mater. Res. Soc. Symp. Proc. **1324** (2011)

[10] A. M. Frisch, W. G. Schmidt and J. Bernholc, M. Pristovsek, N. Esser, and W. Richter, Phys. Rev. B **60** (1999) 2488

[11] B. X. Yang, Y. Ishikawa, T. Ozeki, H. Hasegawa, Jpn. J. Appl. Phys. **35** (1996) 1267

[12] V. P. LaBella, Z. Ding, D. W. Bullock, C. Emery, P. M. Thibado, J. Vac. Sci. Technol. A **18** (2000) 1492

[13] N. Esser, W. G. Schmidt, J. Bernholc, A. M. Frisch, P. Vogt, M. Zorn, M. Pritovsek, W. Richter, F. Bechstedt, Th. Hannapel, S. Visbeck, J. Vac. Sci. Technol. B **17** (1999) 1691

[14] L. Li, Q. Fu, C. H. Li, B. K. Han, R. F. Hicks, Phys. Rev. B **61** (2000) 10223

[15] X. Wallart, Surf. Sci. **506** (2002) 203

[16] M. Yoshikawa, A. Nakamura, T. Nomura, and K. Ishikawa, Jpn. J. Appl. Phys. **35** (1995) 1205

[17] S. El Kazzi, L. Desplanque, C. Coinon, Y. Wang, P. Ruterana, and X. Wallart, Appl. Phys. Lett. **97** (2010) 192111

[18] Y. Wang, P. Ruterana, L. Desplanque, S. El Kazzi and X. Wallart, Euro. Phys. Lett. **97** (2012) 68011

[19] T. Wang and A. Forchel, J. Appl. Phys. **85** (1999) 2591

[20] O. Suekane, S. Hasegawa, M. Takata, T. Okui, and H. Nakashima, Mater. Sci. Eng. B **88** (2002) 158

[21] Joyce B. A., Vvedensky D. D., Avery A. R., Belk J. G., Dobbs H. T. and Jones T. S., Appl. Surf. Sci. **130-132** (1998) 357.

[22] Snyder C. W., Mansfield J. F. and Orr B. G., Phys. Rev. B. **46** (1992) 9551.

[23] LeGoues F. K., Reuter M. C., Tersoff J., Hammar M. and Tromp R. M., Phys. Rev. Lett. **73** (1994) 300

[24] Y. Wang, PhD in condensed matters, materials and devices, « Dislocation et relaxation de contraintes aux interfaces entre semi-conducteurs III-V à large difference de parameter de maille», University of Caen, June (2012)

[25] S. El Kazzi, L. Desplanque, C. Coinon, Y. Wang, P. Ruterana, and X. Wallart, J. Appl. Phys. **100** (2012) 123506

[26] L. J. Whitman, P. M. Thibado, S. C. Erwin, B. R. Bennett, and B. V. Shanabrook, Phys. Rev. Lett. **79** (1997) 693

[27] B. R. Bennett, B. V. Shanabrook, and M. E. Twigg, J. Appl. Phys. **85** (1999) 2157

[28] B. Paulus, P. Fulde, and H. Stoll, Phys. Rev. B. **54** (1996) 2556

[29] A Yu Babkevich, R A Cowley, N J Mason and A Stunault, J. Phys.: Condens. Matter **12** (2000) 4747

CHAPTER IV: Growth of high electron mobility AlSb/InAs heterostructures

As mentioned in chapter I, AlSb/InAs heterostructures show promising characteristics for the realisation of high electron mobility transistors. The pioneering work of Chang et al. [1] on these heterostructures has shown a large number of growth difficulties to overcome. In this chapter, we present the main problems that occur during the growth of this heterostructure and try to solve them. Eventually, we demonstrate that the results of our work are very promising for the integration of InAs-based heterostructures for the high speed and low power consumption devices for either analog or digital applications.

IV.1 Generalities

IV.1.A AlSb/InAs HEMTs

A typical InAs-based HEMT structure, depicted in figure IV.1, is composed of:

- A semi-insulator (S.I) **substrate** (GaAs, Si, etc…) separated usually from the channel by a **metamorphic buffer layer** with a large band gap energy. The main target of this buffer is to accommodate the mismatch between the channel and the substrate.
- The **channel** is the material with a low band gap energy (InAs) that receives the 2D electron gas. It determines the transistor performances in terms of transport properties.
- The **spacer layer** is a high band gap energy material (AlSb in our case) that separates the electron donor layer from the channel. The thickness of the spacer layer determines the electron transfer efficiency from the doping plane to the channel but also the degree of Coulomb interactions between travelling electrons in the channel and ionized donor impurities of the doping plane. It thus impacts directly the electron density and mobility in the channel.
- The **doping plane** consists of a donor layer inserted in the barrier material. It provides free electrons to the channel. Both Si and Te can be used for InAs HEMTs. For the former, as Si is a p-type dopant in AlSb, the doping plane must be inserted in a very thin InAs quantum well to be efficient (see section IV.2).
- The **Schottky layer** is designed to complete the gate contact after etching the capping layer (recess).

- The **capping layer** consists of a n-doped low gap material necessary to achieve low resistive ohmic contacts to the drain and source.

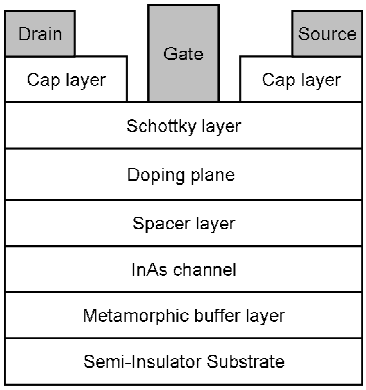

Figure IV.1: *Typical InAs HEMT cross section structure.*

IV.1.B Electron Mobility in heterostructure systems

In devices such as HEMTs for which a low resistivity is a requirement, it is necessary to optimize both the carrier mobility and the concentration in the two dimensional electron gas (2DEG) since the electron mean free path l_e (at low bias) is directly proportional to the mobility, μ, and the square root of the carrier concentration, n_e:

$$l_e = \frac{h}{e\sqrt{2\pi}}\mu\sqrt{n_e} \qquad \textbf{(Eq. IV.1)}$$

The electron mobility depends on the effective mass and on the different electron scattering mechanisms and can be calculated in function of the average transport lifetime as:

$$\mu = \frac{e\langle\tau_{tr}\rangle}{m^*} \qquad \textbf{(Eq. IV.2)}$$

where the inverse of τ_{tr} is the sum of individual scattering rates:

$$\frac{1}{\tau_{tr}} = \frac{1}{\tau_{po}} + \frac{1}{\tau_{ac}} + \frac{1}{\tau_{bgi}} + \frac{1}{\tau_{rii}} + \frac{1}{\tau_{\text{int}}} \qquad \textbf{(Eq. IV.3)}$$

τ_{po} and τ_{ac} are the characteristic times for optical and acoustic phonon scattering respectively. For impurity scattering, background impurities τ_{bgi} and remote ionized impurities in the doping layers τ_{rii} are the most important. A fourth source of scattering comes from the variations of the interfaces, which is exclusive to heterostructure systems, where the roughness of the interface may cause a change in the energy of the confined states [2]. Previous observations [3-4] have shown that at 300 K phonons are dominant in the electron scattering. However, in narrow well samples, interface roughness scattering can be as important as remote impurity scattering at

low temperatures. For example, figure IV.2 exhibits temperature-dependant mobility of an InSb qantum well structure given by Orr et al [2] along with the contributions of the individual scattering mechanisms mentioned above.

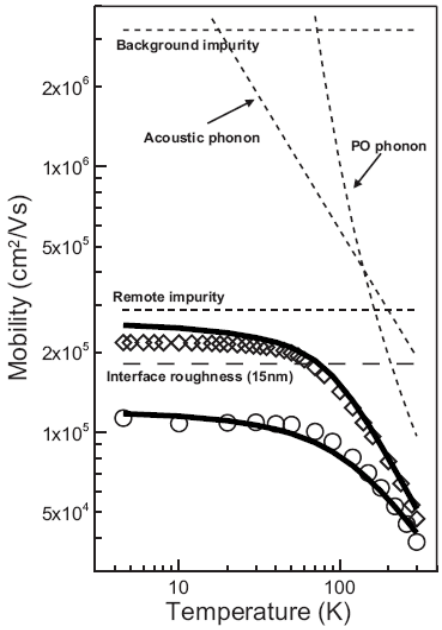

Figure IV.2: *Mobility for a typical 30 nm InSb quantum well heterostructure with a 20 nm spacer (open diamonds) with a theoretical fit (solid line) and a typical 15 nm InSb quantum well (open circles) with a theoretical fit (solid line) using the transport lifetime model. The contributions of individual scattering mechanisms are shown as dashed lines [2].*

This figure shows that the temperature dependence of the mobility is mainly governed by the phonon scattering evolution. As this mechanism is weak at low temperature, the mobility is nearly constant under 77K as the scattering becomes dominated by the impurity scattering terms and, especially in narrow wells, interface roughness scattering.

In the same vein, Mishima et al. [5] investigated the effects of deformation potential scattering due to dislocations in InSb quantum well samples. They calculated the mobility in function of the dislocation density as introduced by Jena and Mishra [6]:

$$\mu_{disl}^{strain} = \frac{2e\hbar^3\pi k_f^2}{N_{disl}m^{*2}b_e^2a_c^2}\left(\frac{1-\gamma}{1-2\gamma}\right)^2\frac{1}{I(n_s)} \qquad \textbf{(Eq. IV.4)}$$

where e is the electronic charge, $\hbar$ is the reduced Planck's constant, $k_f = \sqrt{(2\pi ns)}$ is the Fermi wave vector (n_s is the sheet carrier density in the 2DEG), N_{disl} is the density of TDs, m^* is the electron effective mass, b_e is the magnitude of the Burgers vector, a_c is the conduction band

deformation potential, γ is Poisson's ratio and $I(n_s)$ is a dimensionless integral which depends only on n_s.

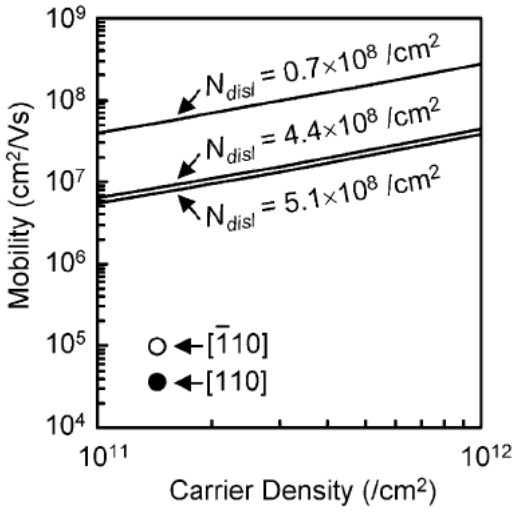

Figure IV.3: *Calculated mobilities in InSb due to dislocation-originated deformation potential scattering for different dislocation densities. Filled and open circles show the measured mobilities in the [110] and [1-10] directions, respectively [5].*

Their calculations presented in figure IV.3 show that the calculated mobilities are larger than the measured mobilities by about two orders of magnitude. Their result indicates that the high density of threading dislocations has a limited impact in the mobility degradation but other structural defects (like microtwins) and above mentioned mechanisms are dominant in the electron scattering.

IV.1.C Anisotropic transport properties in AlSb/InAs

As many groups who have reported on the anisotropic behaviour of strained III-V alloys [7,8], the above study of Mishima reported on the anisotropy of the low temperature mobility between the [110] and [1-10] directions. They declared that their mobility behaviour correlates with the trench densities measured in the two different orientations of the InSb channel surface. With the help of TEM analysis and their calculations, they affirmed that these trenches are due to structural defects, such as micro-twins (rather than threading dislocations). In the AlSb/InAs case, Moschetti et al. [9] have also reported anisotropic behaviour on InP substrates. They showed that threading defects coming from the buffer layers (fig. IV.4a)

induce trenches in the [1-10] direction in the InAs channel (fig.IV.4b) leading to a decrease in the electron mobility in the [110] direction (figure IV.4c).

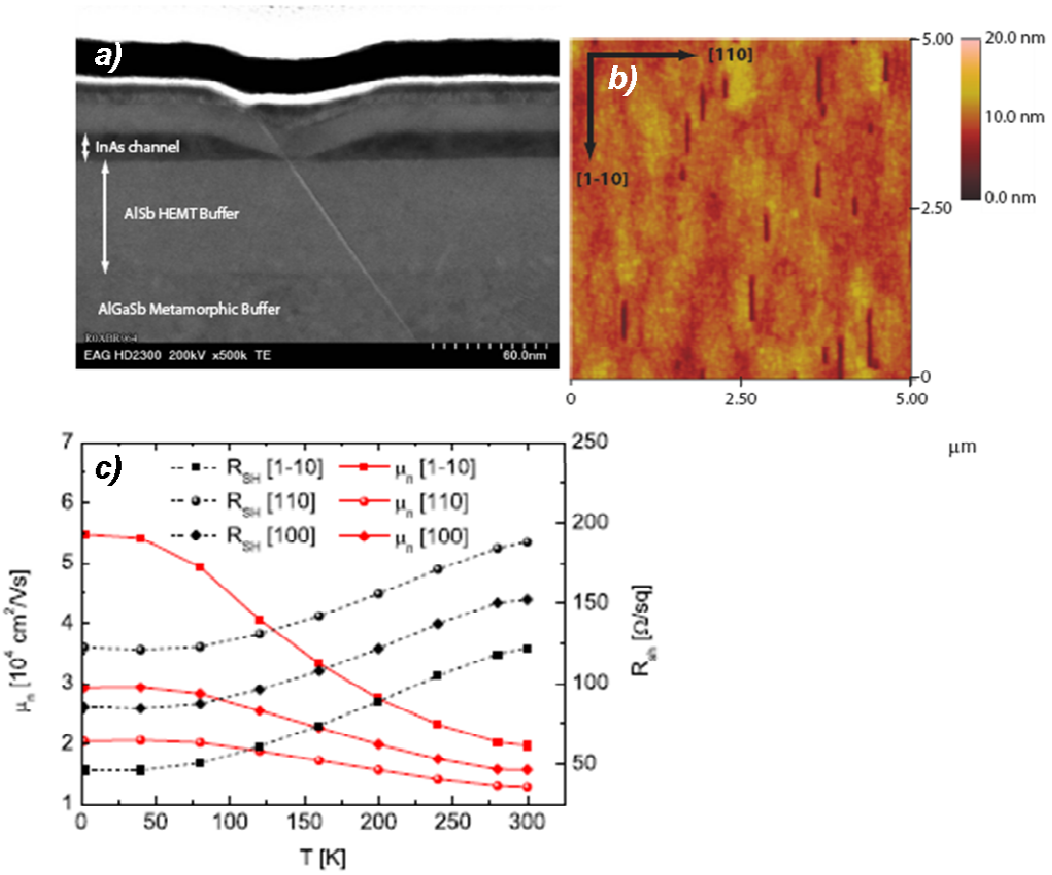

Figure IV.4: ***(a)*** *STEM picture of the InAs/AlSb HEMT cross-section cut along the [110] direction showing clearly the trenches in the [110] direction seen in the AFM image* ***(b)*** *are caused by a threading defect originating from the metamorphic AlSb/InP bulk interface.* ***c)*** *R_{sh} and μ_n for InAs/AlSb Hall bar structures as a function of temperature for [1-10], [110] and [100] directions [12].*

They explained this behaviour by a much larger electron scattering along the [110] direction (i.e. τ_{tr} is smaller) since the trenches are along the [1-10] direction. This hypothesis is supported by the increase in the anisotropy at low temperature, implying that the mobility in the [110] cannot increase with decreasing temperature as the mean free path of the electrons becomes larger than the separation between the trenches. The same observation has been reported by J. Bergman [10], with a channel sheet resistance about 15% higher in the [110] direction compared to the [1-10] one. In his study, he claimed that after increasing the As beam flux the trench density decreases along with the anisotropy.

In our work, we try to clarify the origin of this anisotropic behaviour and optimize the growth conditions to achieve the best transport properties.

IV.2. Growth of AlSb/InAs heterostructures on highly mismatched III-V substrates

The purpose of our work is the growth of AlSb/InAs heterostructures on both GaAs and GaP substrates. In the case of GaAs, HEMT devices for low power and high frequency applications are targeted and hence require an insulating buffer layer: that is why we use AlSb as buffer material. In the case of GaP, an insulating buffer is not mandatory since digital applications via GaP/Si templates are considered, which allows the use of GaSb as buffer material. Nevertheless, in both cases, we study a modulation-doped structure to reveal the transport properties. More particularly, since the effective V/III seems to play an important role in the nucleation process of III-Sb (as shown in chapter III), we investigate in this section the influence of this parameter on the electron mobility in AlSb/InAs heterostructures. Finally, we use the gained knowledge to grow the heterostructure directly on silicon.

IV.2.A. AlSb/InAs heterostructure design

Two different AlSb/InAs heterostrucures are designed depending on the used substrates. The first one (structure 1 in figure IV.5) corresponds to an AlSb/InAs HEMT structure grown on GaAs substrates.

Contact layer	InAs:Te (7x 10^{18} cm^{-3})	5 nm
Protection layer	$Al_{0.5}In_{0.5}As$	4 nm
Schottky layer	AlSb	10 nm
Doping plane	Te	4.5x 10^{12} cm^{-2}
Spacer	AlSb	6.5 nm
Channel	InAs	15 nm
Bottom barrier	AlSb	10 nm
Buffer	$Al_{0.5}Ga_{0.5}Sb$	250 nm
Buffer	AlSb	550 nm
Nucleation layer	AlSb	50 nm
Buffer	GaAs	300 nm
Substrate	GaAs (SI)	

Structure 1

Contact layer	InAs:Si (6 x 10^{18} cm^{-3})	5 nm
Bottom barrier	AlSb	8 nm
	InAs	2 MLs
Doping plane	Si	4.5x 10^{12} cm^{-2}
	InAs	2 MLs
Spacer	AlSb	20 nm
Channel	InAs	15 nm
Bottom barrier	AlSb	50 nm
Buffer	GaSb	600 nm
Nucleation layer	GaSb	50 nm
Buffer	GaP	500 nm
Substrate	GaP (SI)	

Structure 2

Figure IV.5: *Cross section structure of the Te (Si) doped AlSb/InAs heterostructures on GaAs (GaP) substrates.*

On the other hand, the second structure (structure 2 in figure IV.5) is not grown for a purpose of device fabrication. Our main target here is to achieve for the first time the growth of

AlSb/InAs on GaP with interesting transport properties. Before presenting the grown samples we mention hereafter some of the features that should be taken into account for the two types of heterostructures.

1) First, it has been shown that the choice of a GaSb buffer (0.6 μm) generates smoother interfaces than AlSb. For instance, with AlSb buffers, Blank et al. [11] obtained low-temperature (12 K) mobility three to seven times lower than the ones achieved with GaSb. With the latter, a 12 K mobility of 944 000 cm^2V^{-1} s^{-1} was reached with a 1.4 μm buffer thickness. Therefore, we have decided to grow the AlSb/InAs heterostructure on GaP with GaSb buffer layers. Unfortunately, the GaSb buffer resistivity is too low and the use of AlSb buffer layer is very essential for the realisation of HEMT transistors on GaAs. Since AlSb suffers from strong oxidization when exposed to air [12], a 250 nm AlGaSb buffer layer is grown on top of the AlSb buffer to minimize the exposure of pure AlSb during processing and the need for an air-bridge technology [13].

2) In both structures, an AlSb bottom barrier is used to improve electron confinement. However, it is shown that the formation of an AlAs interface between AlSb and InAs induces a high concentration of As on Al antisite defects [14]. Furthermore, this type of interface causes some strain relaxation which degrades the subsequent InAs channel growth. On the other hand, with an InSb-like interface a strain compensation occurs which leads to a streaky reflection high-energy electron diffraction (RHEED) pattern during the channel growth. Therefore, we made sure that an InSb-like interface is always achieved by exposing the AlSb layer to an In flux without group-V elements for the deposition of 1ML of In just before opening the As cell.

3) The InAs channel thickness was determined depending on previous observations especially the ones of Bolognesi et al. who measured mobilities in undoped AlSb/InAs quantum wells as a function of InAs thickness [4]. They found the highest mobilities (~30 000 $cm^2.V^{-1}.s^{-1}$ at 300 K for undoped structures) for channel thicknesses of 125-150 Å. The mobility then rolls off for wider wells most likely due to the onset of scattering by misfit dislocations originating from the lattice mismatch between AlSb and InAs, but even at 250 Å the mobility was still above 20 000 $cm^2.V^{-1}.s^{-1}$ despite the 1.3 % lattice mismatch. On the other hand, the mobility decreases (sheet concentration increase) with the well width (< 100 Å) due to the dominance of interface roughness scattering in the narrower wells.

4) 6.5 nm of AlSb spacer is grown for structure 1 whereas it is 20 nm for structure 2. For the doping plane, both Si and Te appear to be viable for InAs/AlSb heterostructures. However, since Si is amphoteric in III-V compounds (Te acts as a donor in any AsSb alloy) and acts as a

p-type dopant (acceptors) in antimonide-based materials, a special design is needed to achieve an efficient Si doping. This consists in the insertion of the Si doping plane in a few monolayers of InAs in the AlSb barrier [15]. A decrease in the growth temperature at this stage of the growth is also required to minimize Si segregation into AlSb.

5) In structure 1, an $Al_{0.5}In_{0.5}As$ protection layer was then placed between the AlSb Schottky layer and the InAs contact (cap) layer. This protection layer protects the AlSb layer from oxidizing during the gate-recess etch. Furthermore, even if AlSb/InAs heterostructure provides superior ΔEc to any III-V semiconductor compound due to its type II alignment [16], no natural energy barrier for holes exists (type II). The $Al_{0.5}In_{0.5}As$ layer should also act as a blocking barrier to prevent a hole leakage current flowing from the channel to the gate. The structure was finally caped with 5 nm of 7 x 10^{18} cm^{-3} Te-doped InAs. Since on GaP the heterostructure is not used for device fabrication, the structure is finally capped with 5 nm of 6 x 10^{18} cm^{-3} Si-doped bulk InAs without any Schottky or protection layers.

IV.2.B. Samples

Two set of samples presented in tables IV.1 and IV.2 are investigated for the study of AlSb/InAs on GaAs (set 1) and GaP substrates (set 2). For all the samples, after smoothing the substrate surface, a (2x8) Sb-terminated surface is prepared. The growth rates are 0.8 ML/s for Al and 0.7 ML/s for Ga during the growth of the buffer layer for sets 1 and 2, respectively. In the active layer, In and Al growth rates are 0.5 ML/s for both sets.

For set 1, different Sb fluxes from 2.5 to 1 ML/s are used all along the antimonide parts of the structure (samples A to D). After 50 nm of the AlSb nucleation layer grown at 510°C, the growth temperature is increased to 540°C for the remaining AlSb buffer and decreased again to 510°C for the final AlGaSb part and finally to 490°C during the active layer. In order to distinguish between the role of the Sb flux during the AlSb nucleation layer and its impact on the remaining part of the buffer and heterostructure part, we perform another sample A' with an Sb flux of 1 ML/s during the first 50 nm AlSb nucleation layer. The remaining part of the epilayer is grown at 2.5 ML/s as for sample A.

For set 2, different Sb fluxes from 0.9 to 7.5 ML/s and growth temperatures from 450°C to 510°C are tested during the growth of the first 50 nm GaSb. The remaining part of the 600 nm GaSb is then always grown at 510°C with a Sb flux of 2.5 ML/s. During the active layer, the structure is also grown with an Sb flux of 2.5 ML/s.

Sample Reference	A	B	C	A'	D	G	H
Growth temperature of the AlSb nucleation layer (°C)	510	510	510	510	510	560	580
Sb/Al	3.5	2	1.7	1.4	1.2	3.5	3.5
300K n_s(x10^{12} cm^{-2})	-3.4	-3.0	-3.0	-3.4	-2.6	-3.1	-3.2
300K VdP Electron mobility ($cm^2.V^{-1}.s^{-1}$)	15 100	18 600	20 400	19 400	22 000	18700	16600
300K [110] Electron mobility ($cm^2.V^{-1}.s^{-1}$)	10 800	14 600	16 900	16 500	19 700	16500	15400
300K [1-10] Electron mobility ($cm^2.V^{-1}.s^{-1}$)	22 000	21 900	23 200	20 700	23 200	19500	17300
77K VdP Electron mobility ($cm^2.V^{-1}.s^{-1}$)	25 000	36 600	44 900	39 200	54 600	-	-
77K [110] Electron mobility ($cm^2.V^{-1}.s^{-1}$)	16 100	24 400	30 900	27 700	39 500	-	-
77K [1-10] Electron mobility ($cm^2.V^{-1}.s^{-1}$)	60500	57100	67100	49100	67200	-	-

Table IV.1: *Schematic of the Te doped AlSb/InAs heterostructure grown on GaAs (set 1).*

Sample Reference	P1	P2	P3	P4	P5	P6	P7
Growth temperature of the GaSb nucleation layer (°C)	510	510	510	480	480	450	450
Sb/Ga	2	3.5	10.7	2	3.5	1.2	3.5
300K n_s(x10^{12} cm^{-2})	1.74	1.55	1.53	1.65	1.76	1.65	1.72
300K VdP Electron mobility ($cm^2.V^{-1}.s^{-1}$)	10100	19500	15200	24000	18700	27800	19700
300K [110] Electron mobility ($cm^2.V^{-1}.s^{-1}$)	7610	17100	12800	21500	15000	26500	13300
300K [1-10] Electron mobility ($cm^2.V^{-1}.s^{-1}$)	9450	18500	15800	26200	23900	28400	22000
77K n_s(x10^{12} cm^{-2})	-	-	-	1.4	1.4	1.43	-
77K VdP Electron mobility ($cm^2.V^{-1}.s^{-1}$)	-	-	-	79300	43700	120000	-

Table IV.2: *Schematic of the Si doped AlSb/InAs heterostructure grown on GaP (set 2).*

The substrate temperature is then further decreased during the growth of the active layer reaching 460°C during the Si doping plane and the two subsequent InAs monolayers to avoid Si segregation into AlSb.

From these two tables, one can notice that the n_s values in set 1 are much higher than the ones in set 2. We relate this to the spacer thickness in both sets. Indeed, the thicker AlSb spacer in set 2 is expected to induce a lower electron sheet density in the channel but also a reduced ionized impurity scattering. This latter effect is confirmed by the higher mobilities at 77 K measured in set 2 compared to the ones in set 1. However, at 300K, both sets exhibit similar mobility values. This is due to the fact that the effect of ionized impurity scattering on the electron mobility is more marked at 77 K than at 300 K (see figure IV.2), where phonon scattering dominates.

IV.2.C. Influence of the Sb flux on the electron mobility of AlSb/InAs heterostructures grown on mismatched substrates

IV.2.C.1. Study on GaAs substrates

Figure IV.6 exhibits the 300 K Hall electron mobility measured on the samples A, B, C and D grown on GaAs at 510°C, using a Van der Pauw configuration and Hall Bridges oriented along the [1-10] and [110] directions in function of the V/III ratio during AlSb buffer layer growth.

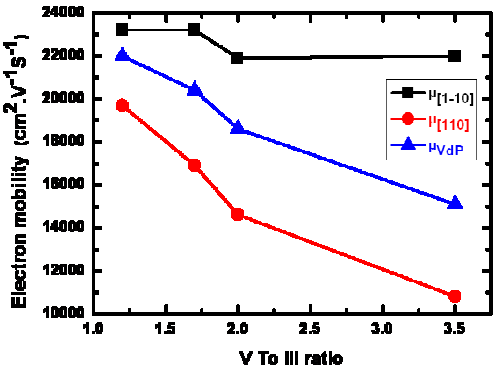

Figure IV.6 : *Hall electron mobility measured on AlSb/InAs heterostructures using a Van der Pauw configuration (μ_{VdP}, triangles), Hall Bridges oriented along [1-10] direction ($\mu_{[1-10]}$,squares) and Hall Bridges oriented along [110] direction ($\mu_{[110]}$, circles) in function of the V /III ratio during antimonide layer MBE growth [17].*

As can be noticed, the room temperature electron mobility in the [110] crystallographic orientation is strongly reduced by increasing the V/III ratio during the growth whereas that in

the [1-10] direction is nearly constant. The evolution of the Van der Pauw mobility is consistent with this observation with a mean value between the two orthogonal orientations. Concerning the sheet carrier density, a higher Sb flux during the doping plane leads to a slightly higher doping efficiency (see table IV.1). Since the [1-10] electron mobility is nearly not affected by this variation, it cannot explain the strong reduction of electron mobility in the [110] orientation. The ratio of electron mobility measured in the [1-10] and [110] directions is plotted in Figure IV.7.

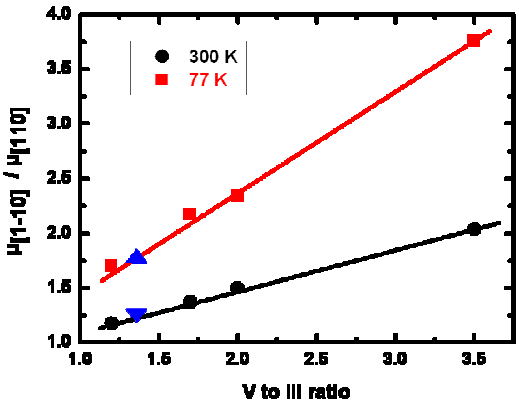

Figure IV.7: *Ratio of electron mobility measured on Hall Bridge oriented respectively in the [1-10] and [110] orientations at 300K (circles) and 77K (squares) for a different V/III ratio during the antimonide layers of the structure. Down- and up- triangles show respectively the value of electron mobility measured at 300K and 77K on the same heterostructure with a V/III ratio of 1.4 during the initial 50 nm part of the AlSb buffer, the V/III ratio was 3.5 during the rest of the buffer layer and AlSb/InAs heterostructure [17]*

An increasing V/III ratio leads to a linear increase in the mobility anisotropy both at room temperature and 77 K. The anisotropy measured on the sample with a reduced Sb flux during the AlSb nucleation layer (sample A', triangles in Figure IV.7) follows exactly the evolution observed with the first set of samples. This result demonstrates that the origin of the electron mobility anisotropy is directly related to the V/III ratio during the first stage of the AlSb growth.

To observe the influence of the Sb flux during the buffer layer on the morphology of the InAs channel, two specific samples, E and F have been grown, similar to sample A and D respectively, but the growth was interrupted just after the InAs channel to avoid any roughening of the substrate by the top InAlAs barrier. The morphologies of samples E and F are shown in the AFM images of Figures IV.8a and 8b. As can be deduced from these images, the anisotropy of mobility observed on the previous samples is directly related to the density of

trenches oriented in the [1-10] direction, the interaction of these defects with travelling electrons in the [110] direction being much more detrimental. From the AFM images, the density of trenches for a 2.5 ML/s Sb flux is about 3 x 10^8 cm^{-2}, whereas it is about 0.7 x 10^8 cm^{-2} for a 0.9 ML/s Sb flux.

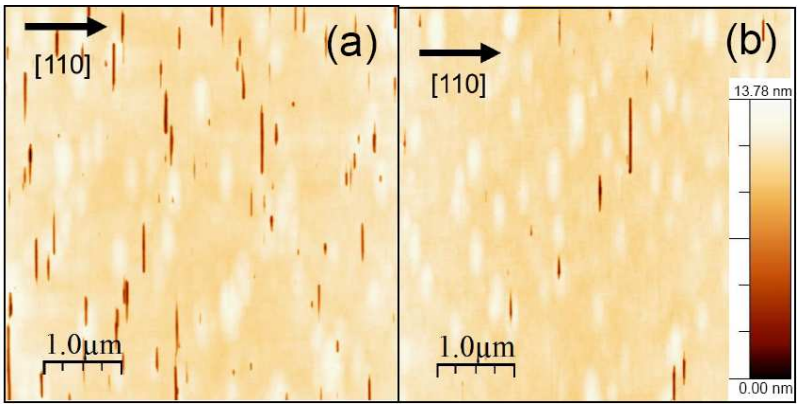

Figure IV.8 : *AFM measurement on sample E (a) and F (b) with respectively 2.5 and 0.9 ML/s Sb overpressure during antimonide layers [17].*

In Figure IV.9, the cross section TEM observations along the [110] zone axis of sample E show that the trenches are induced by threading defects coming from the AlSb buffer layer Their orientation with respect to the growth direction (about 35°) indicates that these defects are in the (111) planes. The HRTEM images of Figures IV.9(b) and 9(d) give precise evidence that these defects are micro-twins.

A semi-quantitative understanding of the influence of the trench density on the mobility is explained considering the electron mean free path l_e in the InAs 2D electron gas. In the [1-10] direction which is nearly not affected by the trenches, the measured mobility of 22 000 $cm^2/V.s$ associated with a sheet carrier density of $3x10^{12}/cm^2$ leads to an electron mean free path around 0.6 µm at room temperature. This means that the critical trench density above which trenches will reduce the electron mean free path and hence the mobility amounts to $1/(l_e)^2$ = 2.5 x $10^8/cm^2$. This is in semi-quantitative agreement with our measurements for which a strong mobility reduction in the [110] direction is observed for a trench density of 3 x $10^8/cm^2$ whereas the effect is less for a trench density of 0.7 x $10^8/cm^2$. At 77K, of course, the mean free path increases (around 1.7 µm) and the effect of the trenches on the [110] mobility is stronger, even for the lowest trench density.

To understand the origin of micro-twins at high V/III ratio, we need to go back to the observations we have already mentioned on the influence of the V/ III ratio on the formation of

GaSb islands (chapter III). A high V/III ratio promotes the formation of large {111} facetted islands that are elongated in the [110] direction and relaxed with 90° MDs at the interface. In this work, in which growth starts with the deposition of AlSb islands on GaAs, rapid AlSb oxidization prevents one from studying the early stages of the growth but the spotty RHEED pattern observed during the nucleation reveals that AlSb islands are initially formed. We may then infer that under high V/III ratios (or high Sb overpressure), micro-twins are generated during the coalescence of the {111} advancing facets of the relaxed AlSb islands.

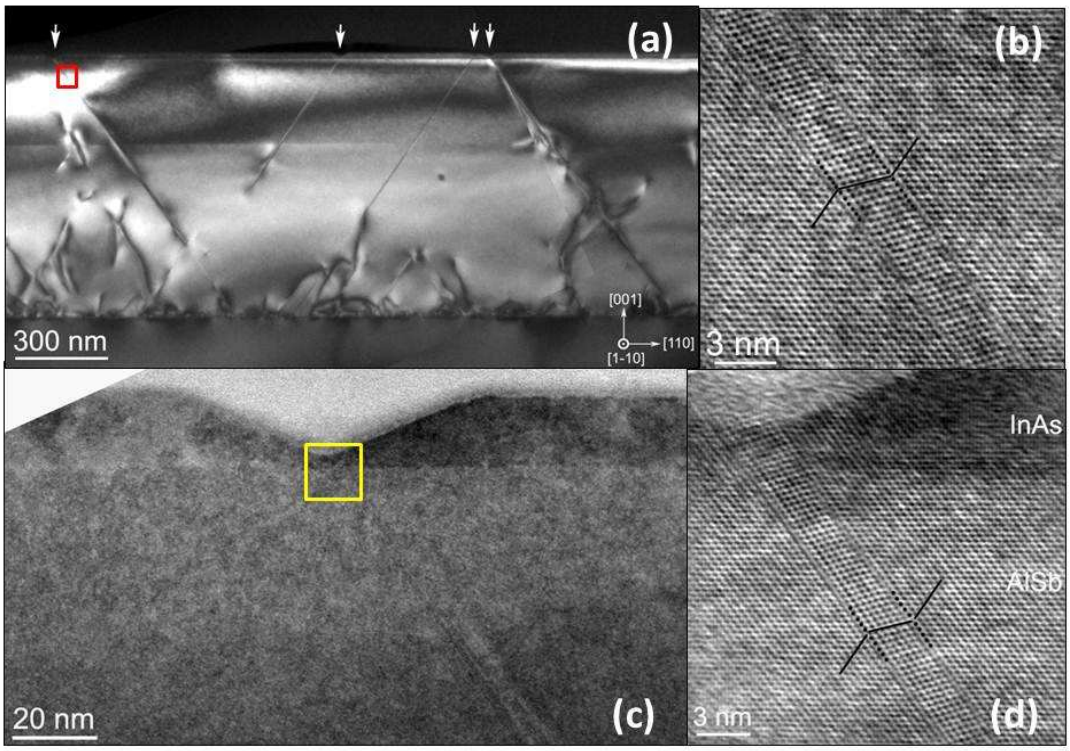

Figure IV.9: *Image (a) displays a TEM cross-section measurement (g=002 dark field) on the sample with the highest Sb flux (sample E). The white arrows indicate the presence of trenches in the InAs layer coming from the threading defects originating from the AlSb/GaAs interface. Image (b) is an HRTEM image of a threading defect from the highlighted area of figure (a): The atomic configuration of the defect is underlined evidencing a micro-twin. Image (c) shows a TEM cross-section of one of the InAs trenches in sample E. Image (d) is a HRTEM image of the highlighted area of figure (c) showing the connection between the InAs trench and the micro-twin [17].*

IV.2.C.2. Study on GaP substrates

The same electron mobility measurements in function of the Sb flux during the nucleation layer are performed on the samples of set 2 grown on GaP substrates for different temperatures. The results are presented in figure IV.10.

For all the heterostructures, a sheet carrier density from 1.5 x 10^{12} to 1.7 x 10^{12} cm^{-2} is measured. In figure IV.10a, a poor electron mobility (about 10 000 $cm^2/V.s$) is observed at 510°C. This can be explained from the AFM image of the sample given on figure IV.11. Since the surface suffers from a large Sb reevaporation at 510°C, an Sb flux of 1.4 ML/s is not sufficient to satisfy an effective Sb/Ga flux ratio higher than unity. Therefore a strong degradation of the surface morphology appears, inducing a poor electron mobility. However, when this fundamental condition is fulfilled (2.5 ML/s Sb flux), a further increase in the Sb flux (or V/III ratio) results in a degradation of the electron mobility in the InAs channel. This is consistent with the previous experiments on GaAs.

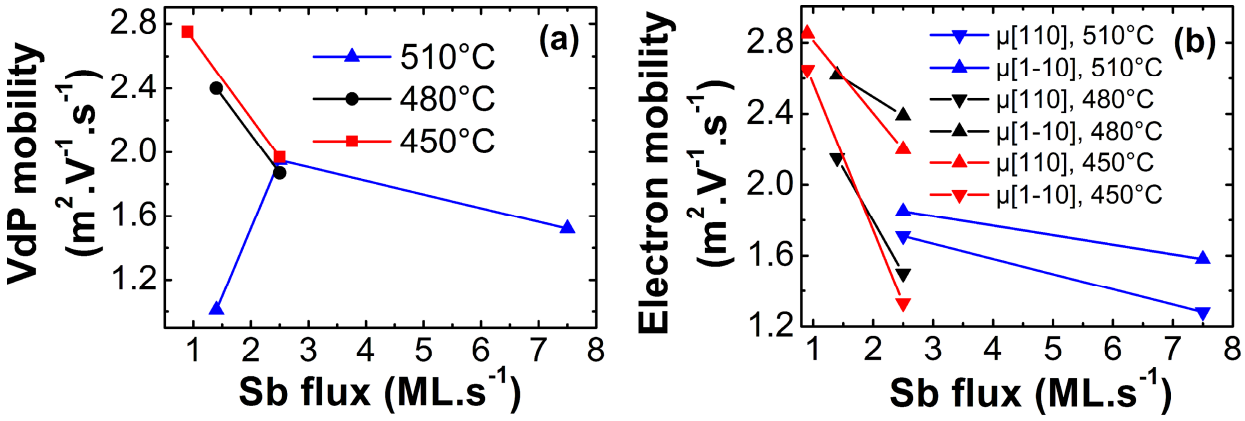

Figure IV.10: *Transport measurements on the heterostructures grown on GaP substrates with different temperatures and Sb fluxes during the first 50 nm of the GaSb buffer layer: (a) room temperature Van der Pauw electron mobility and (b) Hall Bridge measurements in the two crystallographic orientations*

On the other hand, we have mentioned previously that the Sb flux does not affect in the same way the electron mobility in the [110] and in the [1-10] directions. In figure IV.11b, this observation is confirmed at 450°C. However, at 510°C the Sb flux seems to have a reduced influence. It seems that the anisotropy behaviour changes with the growth temperature.

Figure IV.12 presents the anisotropy of the electron mobility in function of the Sb flux for different growth temperatures. From this figure, the anisotropy always increases with the Sb flux. However, the slope of this variation depends on the growth temperature. By extrapolating the data to a Sb/Ga flux ratio near unity, it seems that whatever is the temperature, the same mobility in [110] and [1-10] directions can be achieved. However, this condition can't be reached for the highest temperatures as a part of the Sb flux is needed to compensate Sb reevaporation. If this condition is not fulfilled, a degradation of the surface morphology as the one seen on figure IV.11 occurs, leading to a poor electron mobility in both directions. As a

consequence, the influence of the Sb flux on the surface morphology and the electron mobility in the heterostructure is linked to the growth temperature and these two parameters must simultaneously be considered.

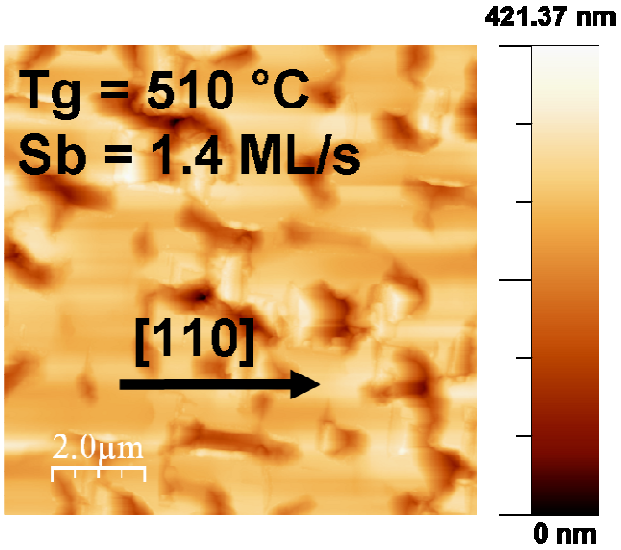

Figure IV.11: *(10x10) µm² AFM image of sample P1 grown with a Sb flux of 1.4 ML/s at 510°C during GaSb nucleation*

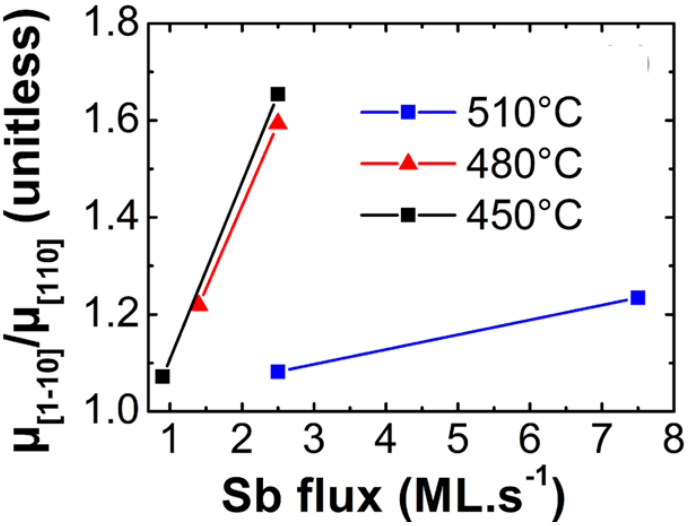

Figure IV.12: *Anisotropy of electron mobility deduced from figure IV.11b*

IV.2.D. Influence of the growth temperature on the electron mobility of AlSb/InAs heterostructures grown on mismatched substrates

To understand the effect of the Sb flux at different temperatures, we perform AFM measurements on the different samples grown on GaP. The results are shown on figure IV.13.

As for the case of GaAs, the AFM images of figures IV.13c, d, e and f exhibit trenches in the [1-10] direction. However, for the samples grown at 510°C (figure IV.13a and b), the morphology is slightly different since trenches oriented in the [110] direction also appear and are connected to trenches oriented in the [1-10] direction. This kind of defects is dominant at low Sb flux whereas most of the defects at large Sb fluxes are [1-10] trenches. Therefore, we measured the mean distance between these different trenches which are quantitatively estimated from their density on (10x10) μm^2 AFM images. Figure IV.14 exhibits this distance in the [110] and [1-10] directions in function of the GaSb growth temperature for a fixed Sb flux of 2.5 ML/s.

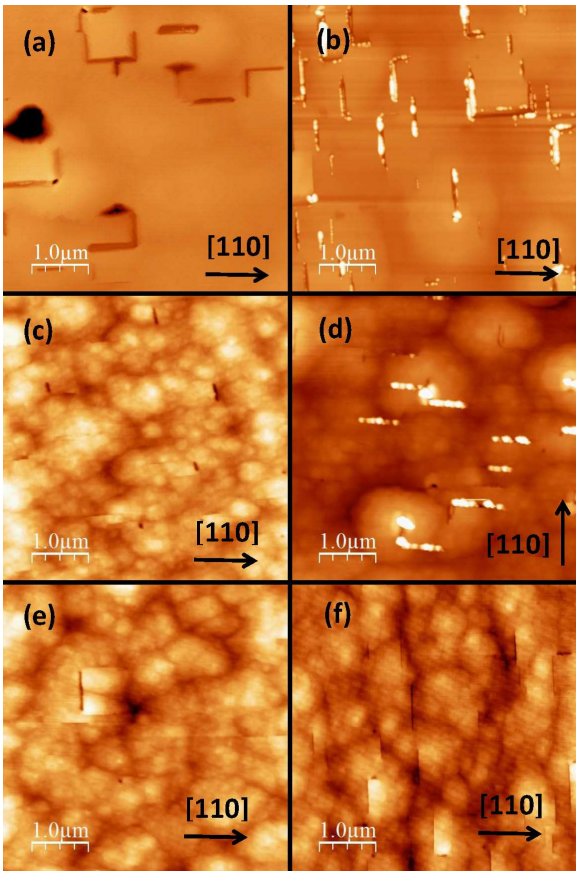

Figure IV.13 : *AFM images of AlSb/InAs heterostructures grown on GaP substrate for a GaSb nucleation layer grown at 510°C with a Sb flux of 2.5 ML/s (a) and 7.5 ML/s (b); at 480°C with a Sb flux of 1.4 ML/s (c) and 2.5 ML/s (d) and at 450°C with a Sb flux of 0.9 ML/s (e) and 2.5 ML/s (f). The bright spots on images b and d are attributed to AlSb oxidization when exposed to air within the trenches.*

From this graph, we note that the two distances in the two directions are in a range comparable with the electron mean free path (~1 µm for sample P1). This is why we can relate the mobility

variation in both directions to both [110] and [1-10] trenches. Secondly, it appears that the increase in the growth temperature has two effects:

(i) It increases the mean distance between the [1-10] trenches. Since the effective Sb/Ga flux ratio is reduced at high temperature, the trench density in the [1-10] direction decreases. This result is also confirmed with the increase of the [110] electron mobility with the temperature.

(ii) The growth temperature increase from 450 to 480°C slightly influences the mobility in the [1-10] direction. This result is consistent with the influence of the V/III ratio on the [1-10] mobility shown in figure IV.6. However, a further increase of the growth temperature promotes the formation of [110] trenches (the mean distance between trenches in the [110] direction decreases) and hence degrades the electron mobility in the [1-10] direction.

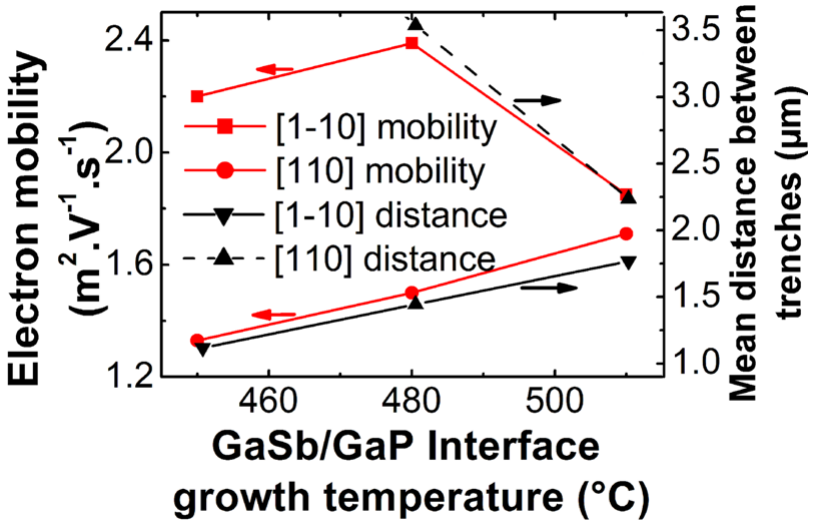

Figure IV.14: *Hall Bridge measurements (red) in the two crystallographic orientations for a fixed Sb flux of 2.5 ML/s and different temperatures during the GaSb nucleation layer and mean distance between [110] or [1-10] trenches (black) evaluated from the trench density measured by AFM.*

To understand the two effects of the growth temperature, one should take into account what we have previously mentioned on the influence of the Sb overpressure on the GaSb nucleation process. Actually, when strong Sb reevaporation occurs at 510°C, a low Sb/Ga flux ratio causes stacking faults accommodating the strain in individual islands (see figure III.27). These stacking faults are probably at the origin of the [110] trenches observed at the surface of AlSb/InAs heterostructures. On the other hand, a high Sb/Ga flux during the initial stage of the GaSb growth results in the formation of [110] elongated islands. This delays the island coalescence and induces microtwins (or trenches in the [1-10] direction).

In the same vein, we present on figure IV.15a the electron mobility of samples A, G and H in function of the growth temperature of the AlSb nucleation layer on GaAs substrate. As for the case of GaP, we notice that increasing the growth temperature to 560°C, the electron mobility measured in the [110] direction is improved. In comparison with sample A, samples G and H (figures IV.15c and d) exhibit much lower trench density in the [1-10] direction. However, a small decrease in the [110] mobility appears at 580°C. We attribute this decrease to the fact that an Sb flux of 2.5 ML/s at 580°C is too low to satisfy an effective Sb/Al flux ratio higher than unity. Therefore, even if a lower [1-10] trench density is achieved, the mobility in both [110] and [1-10] decreases. The evolution of the Van der Pauw mobility is consistent with this observation. On the other hand, the decrease of the electron mobility in the [1-10] direction with the temperature is consistent with previous observations where trenches in the [110] direction appear at high temperatures as it's evidenced by the AFM images of samples G and H.

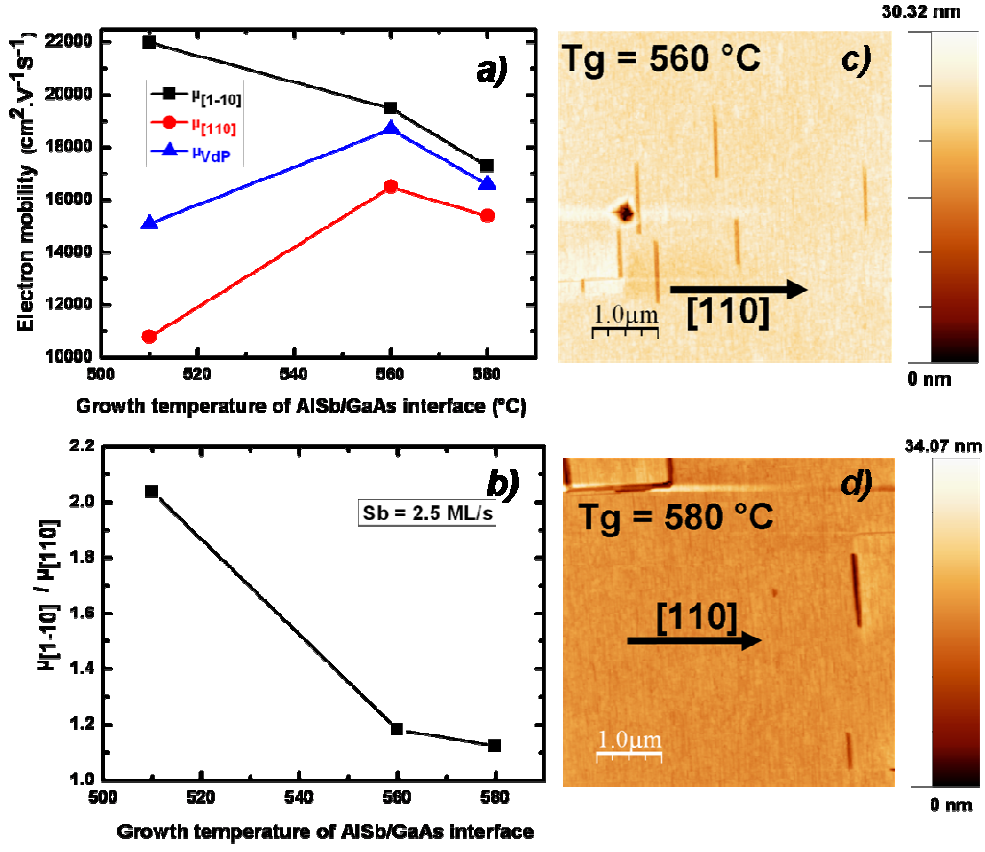

Figure IV.15: *(a) Hall electron mobility measured on AlSb/InAs heterostructures using a Van der Pauw configuration (μ_{VdP}, triangles), Hall Bridges oriented along [1-10] direction ($\mu_{[1-10]}$,squares) and Hall Bridges oriented along [110] direction ($\mu_{[110]}$, circles) in function of the AlSb nucleation layer growth temperature on GaAs substrates [18].(b) Anisotropy of electron mobility deduced from (a). (c) and (d) correspond to the (5 x 5) μm^2 AFM images of samples G and H, respectively.*

IV.2.E. Summary

From the above observations, a trade-off between GaSb (AlSb) relaxation and rapid island coalescence must be found by reducing both the growth temperature and the Sb flux during the nucleation layer. After full coalescence of the GaSb (AlSb) layer, the Sb flux and growth temperature can be simultaneously increased to improve surface roughness. Following these conditions, the sample P6 (figure IV.13e), for which the nucleation layer was grown at 450°C with an Sb flux of 0.9 ML/s exhibits a RMS surface roughness of 0.8 nm and a trench density below 4 x 10^6/cm^2. The Van der Pauw electron mobility reaches 27 800 and 120 000 cm^2.V^{-1}.s^{-1} at 300K and 77K respectively, for a sheet carrier density around 1.5 x 10^{12} cm^{-2}. For comparison, with the similar structure on a GaAs substrate, the mobility value amounts to 30 000 and 143 000 cm^2.V^{-1}.s^{-1} at 300K and 77K respectively.

As regards the influence of the threading dislocation density (TDD), the values determined for AlSb/InAs heterostructures from plan view TEM images lie in the 2-4x10^8cm^{-2} range on both GaAs and GaP substrates. This confirms the estimation of Mishima et al. [5] on the influence of threading dislocations on the electron mobility (figure IV.3): TDDs in the 1x10^8cm^{-2} range are not a limiting factor for mobility below a few 10^6 cm^{-2}V^{-1}s^{-1}.

In the following, we use the above optimized conditions for the growth of an AlSb/InAs heterostructure on an exactly oriented (001) Si substrate using GaP on Si template.

IV.3. Integration of AlSb/InAs heterostructure on direct (001) Si substrate via GaSb/GaP accomodation layer

To our knowledge, the best results on the growth of InAs-based heterostructures directly on a Si substrate are those of Y. C. Lin *et al.* from NTT [18] and K.-M. Ko *et al.* from the Hanyang University [19]. The NTT group reported a RT electron mobility of 27 300 cm^2/V.s for an $Al_{0.5}Ga_{0.5}Sb$/InAs HEMT grown on a 6° off-cut toward the [110] direction Si substrate by using more than 6 µm of AlGaSb, GaAs and Ge/$Ge_{0.9}Si_{0.05}Sb$/ $Ge_{0.9}Si_{0.1}$ buffer layers (see figure IV.16a). This is the highest mobility achieved so far for any HEMT structure grown on a Si substrate. However, no low temperature mobility value has been reported and the sheet density of 3x10^{12}/cm^2 (obtained without any doping plane) seems very high compared to other reported values for the same electron mobility in the InAs-based systems (see chapter I, figure I.5).

a)

GaSb	3 nm
$Al_{0.5}Ga_{0.5}Sb$	13 nm
InAs	15 nm
$Al_{0.5}Ga_{0.5}Sb$	50 nm
GaSb/AlSb	(2.5 nm/2.5 nm) x 10
$Al_{0.5}Ga_{0.5}Sb$	1 μm
GaSb/AlSb	(2.5 nm/2.5 nm) x 10
AlSb	100 nm
GaAs	1 μm (by MBE)
GaAs	1.5 μm (by MOCVD)
Ge	1 μm
$Si_{0.05}Ge_{0.95}$	0.8 μm
$Si_{0.1}Ge_{0.9}$	0.8 μm
Si substrate	

b)

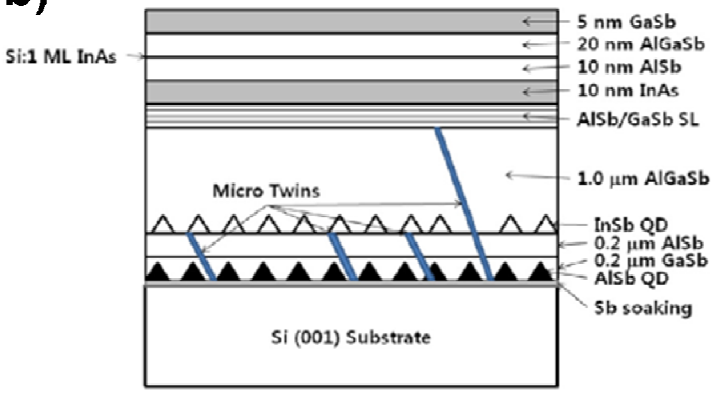

***Figure IV.16**: Structure of the AlGaSb/ InAs HEMT grown on the Si substrate from a)[18]and b)[19]*

On the other side, Ko *et al.* used an InSb quantum dot layer as a dislocation filter at the AlSb/Si interface for the growth of AlGaSb/InAs HEMTs (fig. IV.16b). A thinner buffer layer of AlGaSb was achieved with a low defect density (~10^6 cm^{-2}). However, the electron mobility value of 16 000 cm^2/V.s with a sheet density of 2.5 x 10^{12}/cm^2 remains below state-of-the art values.

Coming back to our study, the $NAsP_{III/V}$ GmbH start-up from the Philipps-University of Marburg provided us with (4 x 4) cm^2 samples cleaved out from a GaP/Si template grown by MOVPE on a 300 mm (001) +/- 0.5° p-doped Si wafer. We used this sample as a substrate for the MBE growth of the same AlSb/InAs heterostructure than that grown on GaP (structure 2 on figure IV.5). The template consists of a 1000 nm thick n-doped Si buffer layer followed by a 46 nm thick GaP nucleation film. The MOVPE growth on exactly oriented 300 mm Si substrates is carried out in a Close Couple Showerhead reactor (Crius-R) from Aixtron SE applying triethylgallium, tertiarybuthylphosphine and silane as group-III-, group-V- and Si-precursors, respectively. After the deposition of about 30 nm GaP the III/V layer is free of antiphase disorder. Before the MBE growth, the GaP nucleation layer is completely pseudomorphically strained to Si without any misfit or threading dislocations. More details about the growth conditions and crystal quality are published elsewhere [20-22].

The same growth conditions and structure than sample P6 have been used on the GaP/Si template (figure IV.17a). The AFM image of figure IV.17b reveals a very smooth surface exhibiting a RMS roughness value of only 0.8 nm. No trench can be observed in this image but a larger scale view indicates a trench density of about 2x10^6 cm^{-2}.

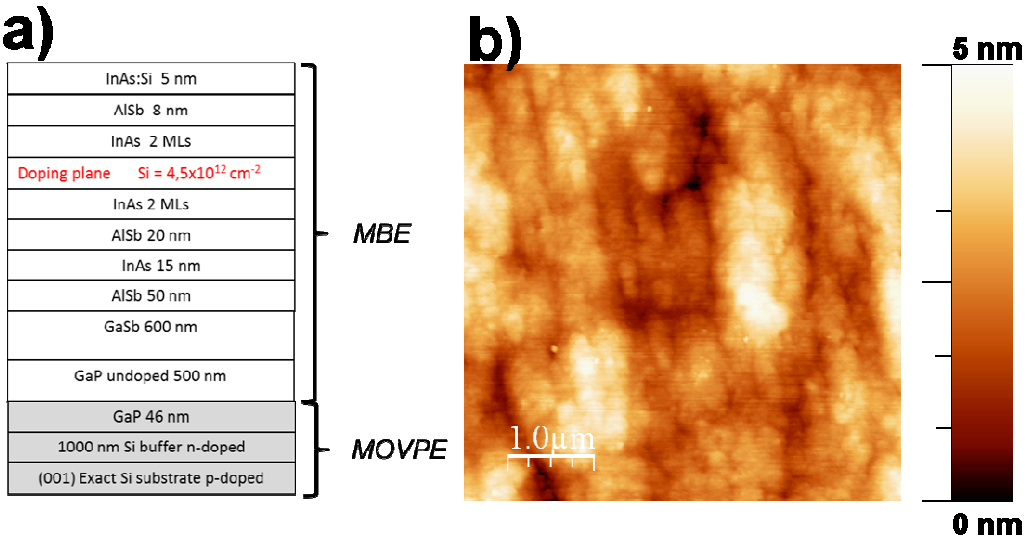

Figure IV.17: a) *Schematics of the AlSb/InAs heterostructures grown on Silicon substrate and* ***b)*** *is its AFM surface image.*

On the X-ray Diffraction (XRD) mapping of the sample (figure IV.18), the diffraction spots of the different layers can be identified and information about strain relaxation can be deduced using X'pert Epitaxy Software. This analysis reveals a fully relaxed GaP layer and a 101% strain relaxation in both direction for the GaSb one with parallel and perpendicular mismatches with Si of 12.44% and 12.07% respectively (the theoretical one is 12.24%).

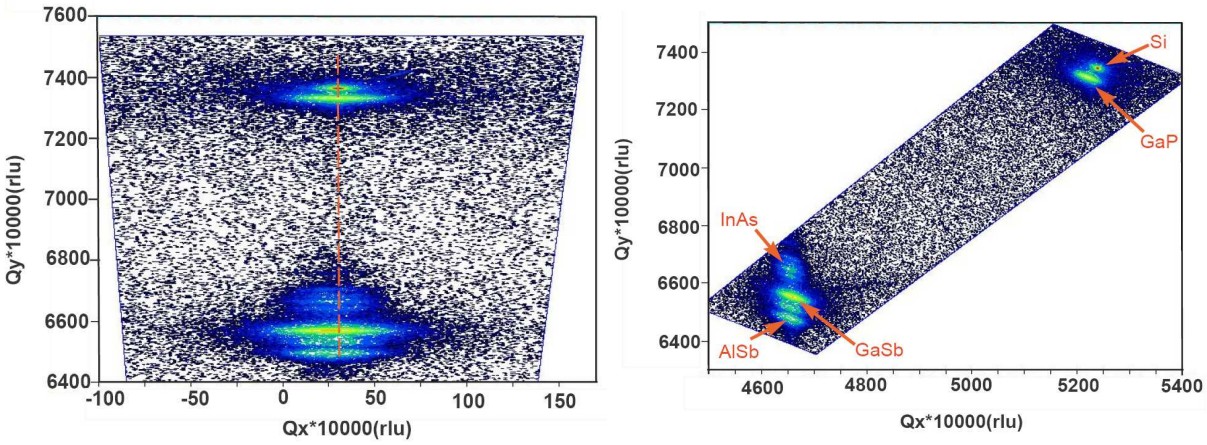

Figure IV.18: *004 (up) and 224 (down) RSM of the heterostructure grown on silicon. The dash red line on 004 RSM indicates the position of full relaxation.*

This tensile strain in the GaSb layer can seem quite unexpected but can be understood considering the different thermal expansion coefficients of GaSb (7.75 x 10^{-6} K^{-1}) and Si (2.6 x 10^{-6} K^{-1}). Diffraction spots corresponding to AlSb and InAs layers can also be observed on the

XRD mapping. Their position with respect to the GaSb spot reveals their respective compressive and tensile strained nature. Concerning InAs, the multiple spots are attributed to Pendellösung oscillations confirming the high quality of the channel material.

Figure IV.19 displays the TEM dark-field cross section of the sample grown on silicon. As can be noticed, APDs that could form at the GaP/Si interface are rapidly self-annihilated and no defects reaching the GaSb/GaP interface can be observed.

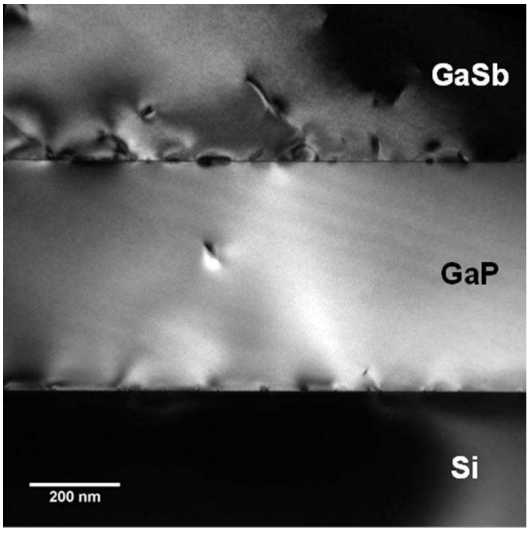

Figure IV.19: *002 dark field cross section of the GaSb/GaP/Si template.*

The HRTEM image of the GaP/Si interface (figure IV.20a) and the ε_{yy} component of the strain tensor (figure IV.20b) reveal an interface misfit dislocation resulting from the relaxation of the GaP layer.

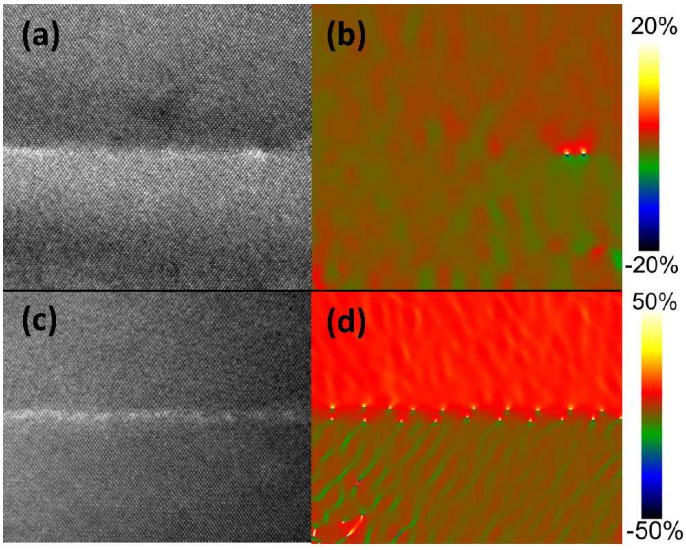

Figure IV.20: *HRTEM cross sections of the GaP/Si interface (a) and the GaSb/GaAs interface (c) and their associated ε_{yy} component of the strain tensor (respectively b and d).*

Concerning the GaSb/GaP interface, most of the mismatch is accommodated by closely spaced 60° MDs resulting in a regular array of 90° MDs with a period of about 3.7 nm (figure IV.20c and d). Some imperfections of this MD array result in the formation of few threading dislocations as can be noticed on figure IV.19. However, no microtwins, much more detrimental for electron mobility in the InAs channel, can be observed.

Hall measurements performed on this heterostructure results in a RT Van der Pauw electron mobility of 27 800 $cm^2.V^{-1}.s^{-1}$ with a sheet carrier density of $1.5x10^{12}$ cm^{-2}. At 77K, the electron mobility increases up to 111 000 $cm^2.V^{-1}.s^{-1}$ without anisotropy (μ[110] =106 000 $cm^2.V^{-1}.s^{-1}$ and μ[1-10]=109 000 $cm^2.V^{-1}.s^{-1}$), confirming the high quality of the InAs channel.

IV.4. Conclusion

In conclusion, we have found that reducing the growth temperature and the Sb flux during the nucleation layer of a III-Sb layer on a mismatched III-V substrate improves the transport properties in the active layer. After optimizing the growth of AlSb/InAs on a GaP substrate, the same structure was grown on a Si substrate via a GaP/Si template. A high electron mobility AlSb/InAs heterostructure of 27 800 $cm^2.V^{-1}.s^{-1}$ and 111 000 $cm^2.V^{-1}.s^{-1}$ respectively at 300 and 77 K was achieved. In comparison with references [18] and [19], our results show the usefulness of a GaSb/GaP accommodation layer to grow highly mismatched III-V materials on exactly oriented (001) Si substrate with only 0.6 µm of III-Sb buffer layer.

References

[1] C. A. Chang, L. L. Chang, E. E. Mendez, M. S. Christie, and L. Esaki, J. Vac. Sci. Technol. B **2** (1984) 214

[2] J. M. S. Orr, A. M. Gilbertson, M. Fearn, O. W. Croad, C. J. Storey, L. Buckle, M. T. Emeny, P. D. Buckle and T. Ashley, Phys. Rev. B **77** (2008) 165334

[3] W. P. Hong, J. Singh and P. K. Bhattacharya, IEEE Electron Device Lett. **7** (1986) 480

[4] C. R. Bolognesi, H. Kroemer and J. H. English, Appl. Phys. Lett. **61** (1992) 213

[5] T. D. Mishima, J. C. Keay, N. Goel, M. A. Ball, S. J. Chung, M. B. Johnson, M. B. Santos, Physica E **21** (2004) 770 [5] S. Sasa, Y. Yamamoto, S. Izumiya, M. Yano, Y. Iwai and M. Inoue, Jpn. J. Appl. Phys. **36** (1997) 1869

[6] D. Jena, U. K. Mishra, Appl. Phys. Lett. **80** (2002) 64

[7] P. Hiesinger, T. Schweizer, K. Kohler, P. Ganser, W. Rothemund, and W. Jantz, J. Appl. Phys. **72** (1992) 2941

[8] F. Peiró, J. C. Ferrer, A. Cornet, J. R. Morante, M. Beck, and M. A. Py, Mater. Sci. Eng. B **44** (1997) 325

[9] G. Moschetti, H. Zhao, P. Å. Nilsson, S. Wang, A. Kalabukhov, G. Dambrine, S. Bollaert, L. Desplanque, X. Wallart and J. Grahn, Appl. Phys. Lett. **97** (2010) 243510

[10] J. Bergman, Partial Fulfilment Of the Requirements for the Degree of Doctor of Philosophy in the School of Electrical and Computer "Development of Indium Arsenide Quantum Well electronic circuits", Georgia Institute of Technology, July (2004)

[11] H. R. Blank, M. Thomas, K.C. Wong, H. Kroemer, Appl. Phys. Lett. **69** (1996) 208

[12] T. Shibata, J. Nakata, Y. Nanishi and M. Fujimoto, Jpn. J. Appl. Phys. **33** (1964) 1767

[13] B. R. Bennett, B. P. Tinkham, J. B. Boos, M. D. Lange, and R. Tsai, J. Vac. Sci. Technol. B **2** (2004) 688

[14] G. Tuttle, H. Kroemer, J. H. English, J. Appl. Phys. **67** (1990) 3032

[15] B. R. Bennett, M. J. Yang, B. V. Shanabrook and D. Park, Appl. Phys. Lett. **72** (1998) 1193

[16] M. Malmkvist, Thesis for the degree of Philosophy "Optimization of Narrow Bandgap HEMTs for Low-Noise and Low-Power Applications", Chalmers University of Technology, Göteborg (2008)

[17] L. Desplanque, S. El Kazzi, J.-L. Codron, Y. Wang, P. Ruterana, G. Moschetti, J. Grahn and X. Wallart, Appl. Phys. Lett. **100** (2012) 262103

[18] Y. C. Lin, H. Yamaguchi, E. Y. Changa and Y. C. Hsieh, M. Ueki, Y. Hirayama, C. Y. Chang Appl. Phys. Lett. **90** (2007) 023509

[19] K.-M. Ko, J.-H. Seo, D.-E. Kim, S.-T. Lee, Y.-K. Noh, M.-D. Kim and J.-E. Oh, Nanotech. **20** (2009) 225201

[20] I. Németh, B. Kunert, W. Stolz, and K. Volz, J. of Cryst. Growth **310** (2008)1595

[21] K. Volz, A. Beyer, W. Witte, J. Ohlmann, I. Németh, B. Kunert and W. Stolz, J. of Cryst. Growth **315** (2011) 37

[22] A. Beyer, J. Ohlmann, S. Liebich, H. Heim, G. Witte, W. Stolz, and K. Volz, J. Appl. Phys. **111** (2012) 083534

CONCLUSIONS AND PERSPECTIVES

The most important result of this study is probably that our working strategy turned out to be very promising for the integration of III-V materials directly on large scale exactly oriented (001) silicon platforms. After presenting the main challenges needed to be overcome in chapter I, we first focused on the III-Sb initial stages of growth on mismatched GaAs and GaP substrates. The knowledge we have gained from this study presented in the third chapter opened the way to optimize the growth conditions of AlSb/InAs heterostructures in chapter IV.

The main conclusions that we have obtained are:

1) A high Sb overpressure promotes the formation of 90° MDs which are then the dominant mechanism for the strain relaxation of the GaSb islands. However, a high Sb overpressure also favours the formation of facetted low density islands inducing slow island coalescence. This will lead to the formation of {111} microtwins and a high density of [1-10] trenches at the InAs channel surface. Thus, a lower mobility in the [110] direction is observed resulting in an increase in the mobility anisotropy.

2) A very low Sb overpressure promotes the formation of stacking faults which, along with 60° MDs, dominate the strain relaxation of the GaSb islands. These SFs can be the reason of the formation of square cracks which decrease the mobility in both directions.

3) The required trade-off in the growth conditions of III-Sb buffer layers to get very good transport properties should take into account two main considerations. First, a maximum density of islands is needed to avoid as much as possible the formation of micro twins at the coalescence step. Secondly, these islands should relax without any SF. If these two conditions are fulfilled and islands relaxed with only 90° MDs are formed, high mobility can be achieved.

4) Previous papers claimed that a decrease in the threading dislocation density (TDD) is essential to achieve high quality optoelectronic devices. In our case, a high density of threading dislocations is not the main limiting factor for the mobility in the InAs/AlSb heterostructure but other threading defects like microtwins or stacking faults are more detrimental to device performance.

Considering the future work, although we obtain high electron mobility in AlSb/InAs heterostructures, the TDD remains high. For devices where a high TDD can be detrimental, further experiments must be carried out on these III-Sb buffer layers to reduce it. More

precisely, as mentioned in chapter I, in the case of a GaSb buffer layer, an AlSb interfacial layer could be inserted to minimize the TDD during the full strain relaxation of GaSb. We have performed a first attempt, introducing 4 AlSb MLs at the GaSb/GaAs interface in the growth sequence of an AlSb/InAs heterostructure [1]. This leads to a moderate reduction of the TDD from 2.2 to 0.64×10^8 cm^{-2}: further significant improvement using this recipe remains to be evaluated as well as the involved mechanism. This latter is probably related to the small diffusion length of Al adatoms which helps in keeping a low density of small islands even at a temperature sufficiently high to get a good strain relaxation.

A more detailed study is also needed to determine what's really happening at the island coalescence. Although our results clearly show that the trenches in the [1-10] direction come from the microtwins, no clear evidence shows that the latter are created from island coalescence. The same remark holds for the case of the square cracks which are related to the creation of SFs. A detailed study of the coalescence process and strain relaxation for different layer thicknesses has to be considered.

As long-term perspectives, this work validates the strategy of integration on Si via Si/GaP templates for electronic devices as a viable alternative to the most popular approach using Si/GaAs or Si/Ge/GaAs buffer layers. We can particularly emphasize the low surface roughness measured (RMS : 0.8 nm) for a relative thin buffer compared to recent published results where RMS values larger than 4 nm were reported for the metamorphic growth of InGaAs/InAlAs heterostructures on Si [2].

On the other hand, despite the high mismatch between InAs and GaP, the high electronic mobility reported demonstrates that good transport properties can be maintained in field effect devices. This could be further evaluated on MOS transistors since the 6.1Å material family offers both opportunity for NMOS (InAs) and PMOS (Ga(In)Sb) [3].

References

[1] Y. Wang, P. Ruterana, L. Desplanque, S. El Kazzi S., and X. Wallart, J. Appl. Phys. **109** (2011) 023509

[2] N. Mukherjee, J. Boardman, B. Chu-Kung, G. Dewey, A. Eisenbach, J. Fastenau, J. Kavalieros, W. K. Liu, D. Lubyshev, M. Metz, K. Millard, M. Radosavljevic, T. Stewart, H. W. Then, P. Tolchinsky, and R. Chau, 2011 IEEE International Electron Devices Meeting (IEDM) Proceedings (2011) 821-824

[3] J. Nah, H. Fang, C. Wang, K. Takei, M. H. Lee, E. Plis, S. Krishna, and A. Javey, Nano Letters **12** (2012) 3592

LIST OF COMMUNICATIONS

Publications:

1- **Monolithic integration of high electron mobility InAs-based heterostructure on exact (001) Silicon using a GaSb/GaP accommodation layer**
L. Desplanque, S. El Kazzi, C. Coinon, S. Ziegler, B.Kunert, A. Beyer, K. Volz, W. Stolz, Y. Wang, P. Ruterana and X. Wallart
Appl. Phys. Lett. **101** (2012) 142111

2- **Strain relief and growth optimization of GaSb on GaP by molecular beam epitaxy**
Y. Wang, P. Ruterana, J. Chen, L. Desplanque, S. El Kazzi and X. Wallart
*J. Phys.: Condens. Matter **24** (2012) 335802*

3- **Interplay between Sb flux and growth temperature during the formation of GaSb islands on GaP**
S. El Kazzi, L. Desplanque, Y. Wang, P. Ruterana, and X. Wallart
J. Appl. Phys. **111** (2012) 123506

4- **AlSb nucleation induced anisotropic electron mobility in AlSb/InAs heterostructures on GaAs**
L. Desplanque, S. El Kazzi, J.-L. Codron, Y. Wang, P. Ruterana, G.Moschetti, J.Grahn and X. Wallart
Appl. Phys. Lett. **100** (2012) 262103

5- **Mechanism of formation of the misfit dislocations at the cubic materials interfaces**
Y. Wang, P. Ruterana, S. Kret, J. Chen, S. El Kazzi, L. Desplanque and X. Wallart
Appl. Phys. Lett. **100** (2012) 262110

6- **A growth mode determined misfit dislocation configuration and lattice mismatch strain relaxation at III-V semiconductor interfaces**
Y. Wang, P. Ruterana, L. Desplanque, S. El Kazzi and X. Wallart
Euro Phys. Lett. **97** (2012) 68011

7- **Investigation of the anisotropic strain relaxation in GaSb islands on GaP**
Y. Wang, P. Ruterana, H. P. Lei, J. Chen, S. Kret, S. EL kazzi, L. Desplanque and X. Wallart
J. Appl. Phys. **110** (2011) 043509

8- **GaSb/GaP compliant interface for high electron mobility AlSb/InAs heterostructures on (001) GaP**
S. El Kazzi, L. Desplanque, C. Coinon, Y. Wang, P. Ruterana, and X. Wallart
Appl. Phys. Lett. **97** (2010) 192111

9- **Strain relief at the GaSb/GaAs interface versus substrate surface treatment and AlSb interlayers thickness**
Y. Wang, P. Ruterana, L. Desplanque, S. El Kazzi and X. Wallart
J. Appl. Phys. **109** (2010) 023509

Oral communications:

1- 24th International Conference on Indium Phosphide and Related Materials (IPRM)
High electron mobility InAs-based heterostructure on exact (001) Si using GaSb/GaP accommodation layer
L. Desplanque, Salim El Kazzi, C. Coinon, B. Kunert, Y. Wang, P. Ruterana and X. Wallart
Santa Barbara, August **2012**

2- Material Research Society (MRS) 2012 Spring Meeting
Influence of Sb overpressure on the anisotropic transport properties of InAs/AlSb heterostructures grown on highly mismatched substrates
Salim El Kazzi, L. Desplanque, Y. Wang, P. Ruterana and X. Wallart
San Francisco, April **2012**

3- The 20th European workshop on Heterostructure Technology (HeTech)
Strain relaxation of GaSb islands on GaP and GaAs substrates for high mobility AlSb/InAs heterostructures
Salim El Kazzi, L. Desplanque, Y. Wang, P. Ruterana and X. Wallart
Lille, November **2011**

4- Material Research Society (MRS) 2011 Spring Meeting, Symposium RR
TEM analysis of the dislocation mechanism in III-V Heterostructures grown by molecular beam epitaxy
Y. Wang, P. Ruterana, L. Desplanque, Salim El Kazzi and X. Wallart
San Francisco, April **2011**

5- Material Research Society (MRS) 2011 Spring Meeting, Symposium D
Misfit dislocation and strain relaxation at GaSb/GaAs interface versus substrate surface treatment
Y. Wang, P. Ruterana, L. Desplanque, Salim El Kazzi and X. Wallart
San Francisco, April **2011**

6- International Symposium on Coumpound Semiconductors (ISCS) 2011
Strain relaxation at the GaSb/GaAs and GaSb/GaP interfaces
L. Desplanque, Salim El Kazzi, C. Coinon, Y. Wang, P. Ruterana and X. Wallart
Berlin, March **2011**

7- European Molecular Beam Epitaxy (Euro-MBE) 2011 workshop
Lattice mismatch accomodation at the GaSb/GaAs and GaSb/GaP interfaces
L. Desplanque, Salim El Kazzi, Y. Wang, P. Ruterana and X. Wallart
Grenoble, March **2011**

8- Mediterranean Conference on Innovative Materials and Applications (CIMA)
Compliance at the GaSb/GaP interface by Misfit Dislocations array
Salim El Kazzi, L. Desplanque, C. Coinon, Y. Wang, P. Ruterana and X. Wallart
Beirut, March **2011**

9- 6th International conference on Molecular Beam Epitaxy (MBE)
Strain relaxation by misfit dislocation array at the GaSb/GaP interface
Salim El Kazzi, L. Desplanque, C. Coinon, Y. Wang, P. Ruterana and X. Wallart
Berlin, August **2010**

Posters :

1- PICO 2012
The atomic structure and formation mechanism of misfit dislocations by HAADF investigation
Y. Wang, P. Ruterana, H.P.Lei, J.Chen, S.Kret, Salim El Kazzi, L. Desplanque and X. Wallart
Julich, March **2012**

2- European Material Research Society (E-MRS) 2011 Spring Meeting
Strain relief and growth optimization of the GaSb islands on GaP by molecular beam epitaxy
Y. Wang, P. Ruterana, L. Desplanque, Salim El Kazzi and X. Wallart
Nice, May **2011**

3- Doctoriales Franco-Belges
Study of material growth for high power low consumption devices
Salim El Kazzi, L. Desplanque and X. Wallart
Mons en Baroeul, May **2011**

4- Journées Nationales du Réseau Doctoral en Microélectronique 2010
Morphological study of molecular beam epitaxy GaSb growth on GaP substrate
Salim El Kazzi, L. Desplanque, C. Coinon, Y. Wang, P. Ruterana and X. Wallart
Montpellier, June **2010**

Epitaxial growth of Sb-based heterostructures on highly mismatched substrates for field effect transistor applications

Low power consumption transistors operating at low supply voltage are highly required for both high frequency autonomous communicating systems and CMOS technology. Since the performances of silicon-based devices are strongly degraded upon low voltage operation, low bandgap III-V semiconductors are now considered as alternative active materials. Among them, one of the best candidates is InAs. Therefore, the present work aims on paving the way to the use of InAs in transistor channels for both high-speed analog and digital applications. We particularly investigate the molecular beam epitaxy growth of InAs/AlSb heterostructures on both (001) GaAs and GaP via an antimonide metamorphic buffer layer. Using atomic force microscopy, transmission electron microscopy and reflection high energy electron diffraction, we first show the critical influence of the growth conditions on the III-Sb nucleation. From this study, we then achieve optimized high mobility InAs layers on these two highly mismatched substrates. The results obtained in the GaP case are extended to commercially available high quality GaP/Si platforms for the integration of InAs-based materials on an exactly oriented (001) Si substrate. State of the art mobility of 28 000 $cm^{-2}.V^{-1}.s^{-1}$ at 300K and higher than 100 000 $cm^{-2}.V^{-1}.s^{-1}$ at 77K are demonstrated.

Croissance épitaxiale d'hétérostructures antimoniées sur substrats fortement désadaptés en maille pour applications aux transistors à effet de champ

La nécessité de diminuer la consommation à la fois des systèmes autonomes communicants à haute fréquence et des circuits CMOS implique l'utilisation de transistors fonctionnant sous faible tension d'alimentation. Les performances des composants à base de silicium se dégradant rapidement dans ce régime de fonctionnement, les semiconducteurs III-V à faible bande interdite sont aujourd'hui envisagés comme une alternative. Parmi ceux-ci, l'InAs paraît le plus prometteur. Dans ce contexte, ce travail a pour but d'ouvrir la voie à l'utilisation d'un canal à base d'InAs pour les systèmes analogiques et numériques. Plus précisément, nous étudions la croissance par épitaxie par jets moléculaires des hétérostructures InAs/AlSb sur des substrats (001) GaAs et GaP par l'intermédiaire d'une couche tampon Ga(Al)Sb. La microscopie à force atomique, la microscopie électronique en transmission et la diffraction d'électrons de haute énergie sont utilisées afin de mettre en évidence l'influence critique des conditions de croissance sur la nucléation des antimoniures. Cette étude sert de base à l'optimisation de canaux InAs à haute mobilité sur ces deux substrats fortement désadaptés en maille. Les résultats obtenus dans le cas de GaP sont ensuite étendus au cas de pseudo-substrats commerciaux GaP/Si de haute qualité cristalline pour l'intégration de matériaux à base d'InAs sur des substrats Si (001) exactement orientés. Des mobilités électroniques atteignant 28 000 $cm^{-2}.V^{-1}.s^{-1}$ à 300K et supérieures à 100 000 $cm^{-2}.V^{-1}.s^{-1}$ à 77K sont démontrées.